First-Principles Study on
Solid Iodine under High Pressure

Kenji Yamaguchi

OSAKA UNIVERSITY
GRADUATE SCHOOL OF ENGINEERING SCIENCE
DEPARTMENT OF MATERIAL PHYSICS
TOYONAKA OSAKA

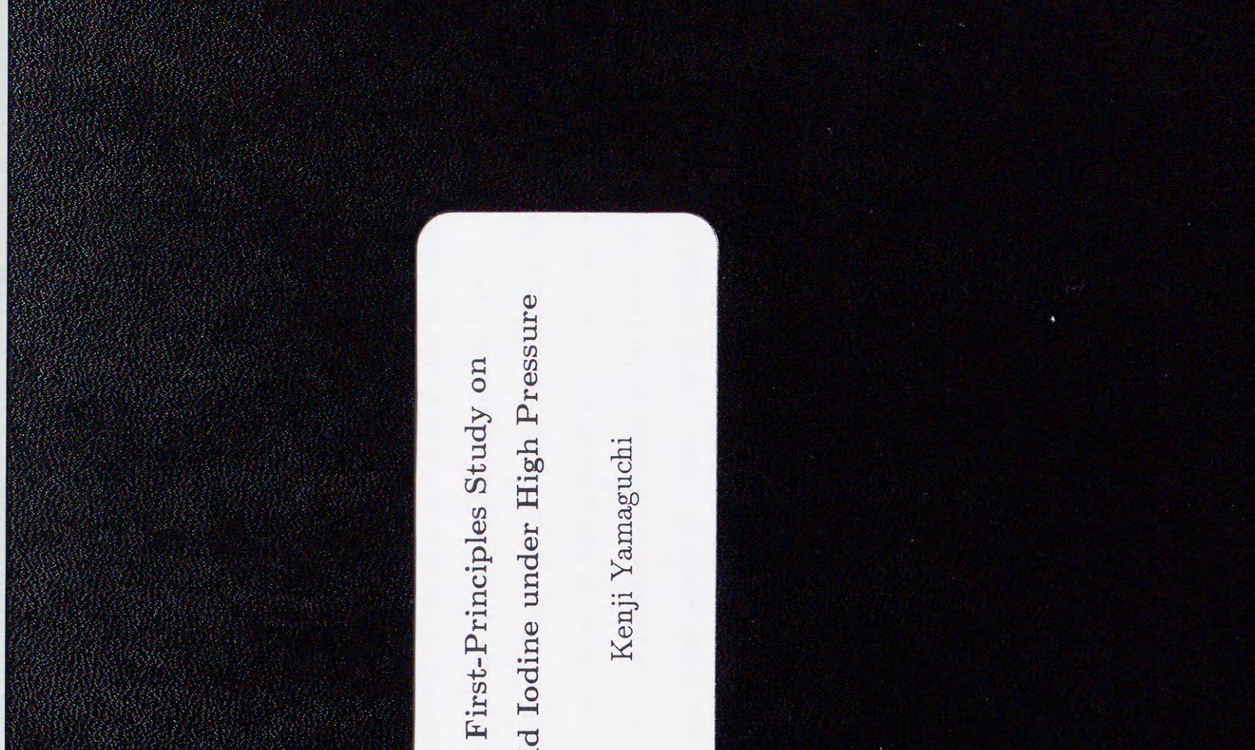

First-Principles Study on Solid Iodine under High Pressure

Kenji Yamaguchi

January, 1997

OSAKA UNIVERSITY
GRADUATE SCHOOL OF ENGINEERING SCIENCE
DEPARTMENT OF MATERIAL PHYSICS
TOYONAKA JAPAN

Abstract

Pressure effects on the molecular dissociation, molecular vibration, and hyperfine parameters of solid iodine are studied theoretically. Full-potential linear-muffin-tin-orbital (FP-LMTO) method is employed for calculating the electronic properties based on the density functional theory within the local density approximation (LDA).

The dimerization, as the reverse of the molecular dissociation, is studied in light of a phenomenological model, firstly introduced by Takemura *et al.*, in which the molecular phase is realized when the monatomic face-centered orthorhombic (FCO) structure is unstable against the transverse phonon at the center of Σ line. It is found that the structure of the molecular phase indicates the gradual molecular dissociation to FCO and the pressure-induced instability of the molecular phase with respect to FCO is caused by the interaction between third neighbors. Because the FCO phase is unstable structure with respect to the monatomic body-centered orthorhombic (BCO) one, the molecular dissociation transition is realized not to FCO but to BCO as observed at 21 GPa.

The frozen-phonon calculations for the Raman active A_g modes of the molecular solid iodine are carried out. The mixing between A_g vibron and libron is increased with increasing pressure. Above the band overlap pressure, which is found around 10 GPa in the present work, the direction of "vibron" is along the *c*-axis and the "libron" along the *b*-axis. It is indicated that the observed pressure-induced softening of Raman active A_g "libron" in the band overlap state is caused by the gradual molecular dissociation as suggested by Shimomura *et al.*

The experimental results of Mössbauer spectroscopy under pressure are explained on the basis of the molecular dissociation picture proposed by X-ray experiments. In the metallic molecular phase, the change of the principal axis of the electric field gradient (EFG) occurs, which is in agreement with the results observed by Pasternak *et al.* above 16 GPa. The change is also the result of the gradual molecular dissociation. In the BCO structure, a

high asymmetry parameter of EFG is obtained, $\eta = 0.49$ at 30 GPa, as is also observed by Pasternak *et al.* above 24 GPa. It is caused by the band Jahn-Teller effect as introduced to explain the stability of BCO by Orita *et al.* The negligible small change in the isomer shift under high pressure is attributed to the cancellation between the effect of the increasing contact density caused by the compressed 5*s*-electrons and that of the increasing shielding by 5*p*-electrons.

Acknowledgment

The author would like to express his sincere thanks to Professor Hiroshi Miyagi for helpful discussions and a number of encouragement in the course of this study. He also wishes to thank Dr. Hitose Nagara, Dr. Ryuji Kato, and Dr. Takao Kotani for enlightening discussions and a number of encouragement. Thanks are also due to the other members of Miyagi Laboratory.

The author would like to thank sincerely Dr. Sergej Yu. Savrasov of Max-Planck-Institute for providing him with the FP-LMTO programs.

The author would like to express his gratitude to Dr. Hiroshi Fujihisa of National Institute of Materials and Chemical Research for providing the author with his experimental data prior to publication. The author also thanks Dr. Kenichi Takemura of National institute for Research in Inorganic Materials, Professor Yasuhiko Fujii of Institute for Solid State Physics, and Dr. Nozomi Orita of Electrotechnical Laboratory for helpful comments.

The author is indebted to Mr. Naoki Tamitani for calling the problem of iodine to his attention. He also thanks Dr. Tomohiro Matsushita for a number of encouragement and discussions.

Contents

1 Introduction

Solid iodine is a diatomic molecular crystal under ambient condition. The diatomic molecular solids have received much attention from a view point of possibilities of molecular dissociation and metallization under high pressure. Especially, the simplest material, solid hydrogen, has attracted keen interest from theoretical, experimental, and astro- physicists over sixty years since the classic study of Wigner and Huntington [1], who predicted that the molecules of solid hydrogen might dissociate to form a monatomic metallic solid at 25 GPa. However, the evidence of molecular dissociation and metallization of solid hydrogen have not been observed over the pressure 200 GPa, which is the vicinity of the experimental limit [2]. In the theoretical side the difficulties lies in treatment of proton as a quantum particle, which has rejected the prompt progress [3]. The electronic structure of atomic hydrogen could be regarded as a lacking one electron from the closed shell structure, and under ambient condition it forms diatomic molecule. The same structure is also seen in halogen atoms, and therefore hydrogen might be classified as a halogen, rather than a alkali metal at low pressure.

Solid halogens have been remarked in past several decades as a "prototype" of pressure-induced metallization and molecular dissociation [4]. Especially, solid iodine was the first material studied for the phenomena. In the following, previous experimental and theoretical studies of solid iodine under pressure are reviewed.

1.1 Previous experimental works

1.1.1 Solid iodine under ambient condition

At ambient pressure, molecular iodine crystallizes into a base-centered orthorhombic structure with the space group $D_{2h}^{18} - Cmca$ and with two molecules per primitive cell [5].

At room temperature the atomic volume $V_0 = 288.34$ a.u. The structure is shown in Fig. 1, and the notations in the figure are to be used in the following parts of present paper. Normal lattice vibrational modes at $\mathbf{k} = 0$ are shown in Fig. 2.

Solid iodine is insulator with the optical energy gap about 1.3 eV [6]. The valence 5p states are occupied by five electrons per atom. Therefore, in a simple picture, σ, π, and π^* bands are occupied, and σ^* bands are unoccupied.

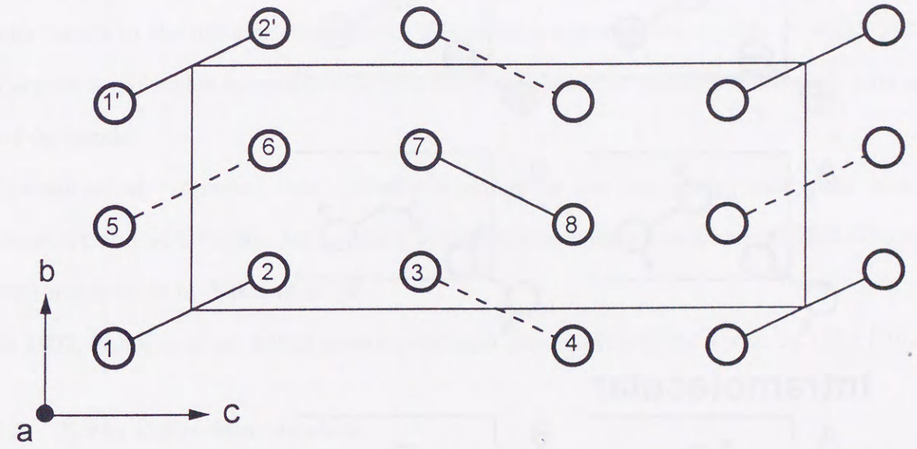

Figure 1: Crystal structure of molecular solid iodine with the space group $D_{2h}^{18} - Cmca$. The molecular axes are parallel to the bc-plane. The molecules in solid lines are on the plane and those in broken lines on the adjacent plane(s) being by $a/2$ above (or below) the plane in solid lines.

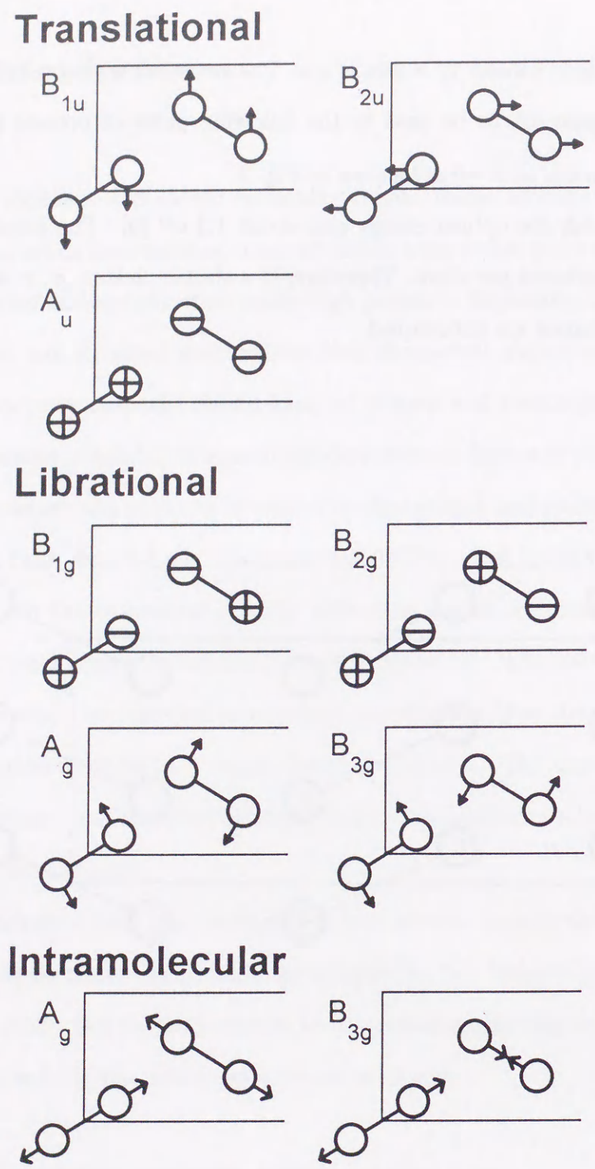

Figure 2: Normal lattice vibrational modes at $\mathbf{k} = 0$ described by two molecules on *bc*-plane. All the librational and intramolecular modes are Raman active and B_{1u} and B_{2u} are infrared active. Under high pressure, for A_g and B_{3g}, the separation of molecular motions into librational and intramolecular motions have not been confirmed.

1.1.2 Pressure-induced metallization

Drickamer and co-workers studied the optical absorption and the electrical resistance under pressure in 1960's [7]. They found that the optical absorption edge decreases with increasing pressure and it vanishes at about 16 GPa. They also found that the electrical resistance decreases with increasing pressure and it gradually reaches metallic region near 16 GPa. At this point, the resistance increases substantially linearly with increasing temperature, and therefore they concluded that solid iodine becomes metallic at 16 GPa. They proposed two models to explain the insulator-metal transition. One is a molecular model, in which the molecular structure is retained and the overlapping between π^* and σ^* bands results in the metallic conduction. The other is a monatomic model, in which iodine undergoes a molecular-to-monatomic transition and becomes metallic state with partially filled 5p bands.

Syassen *et al.* reported that optical reflectivity in the low energy side rises steeply between 21 and 24 GPa [8]. An anomaly of the resistance was found around 22.5 GPa and room temperature by Sakai *et al.* [9].

In 1992, Shimizu *et al.* found pressure-induced superconductivity above 21 GPa [10].

1.1.3 X-ray diffraction studies

Shimomura *et al.* carried out X-ray studies on iodine up to 20.6 GPa and they found that the crystal structure at this pressure is the same one at ambient pressure ($D_{2h}^{18} - Cmca$) [11]. Therefore they concluded that the metallization at 16 GPa comes from the band overlap.

Later, Takemura *et al.* studied up to 30 GPa and they found that the molecular dissociation occurs at 21 GPa with a 4 percent volume change and the structure transforms to a monatomic body-centered orthorhombic (BCO) one with the space group $D_{2h}^{25} - Immm$ [12]. Fujii *et al.* found a second-order transition at 43 GPa from BCO to a body-centered tetrago-

nal (BCT) structure with the space group $D_{4h}^{17} - I4/mmm$ [13], and at 55 GPa a first-order transition with a 1.8 percent volume change from BCT to a face-centered cubic (FCC) structure [14].

Fujihisa *et al.* studied X-ray experiments at temperatures down to 35 K and they found that even at 35 K the molecular dissociation begins at 21.5 GPa and ends at 26.3 GPa [15].

Recently, Reichlin *et al.* found that FCC is stable up to 276 GPa [16].

Very recently Fujihisa *et al.* studied the electron density of molecular phase under pressure using X-ray powder diffraction techniques with a diamond anvil cell and an imaging plate [17]. By using the Maximum Entropy Method, they obtained clear density maps under pressure and found a two-dimensional network formed in the *bc*-plane at the density level of 0.2 e/Å^3 above 16 GPa.

Their recent results of pressure-volume relation, lattice parameters, and atomic distances are shown in Fig.3, Fig.4(a), and (b), respectively [18]. In Fig. 3, the equation of state (EOS) is presented by the Murnaghan's formula [19]:

$$P = \frac{B_0}{B_0'} \ln \left[\left(\frac{V}{V_0} \right)^{-B_0'} - 1 \right] , \qquad (1)$$

with the isothermal bulk modulus at zero pressure $B_0 = 9.833$ GPa and it's pressure derivative $B_0' = 5.363$.

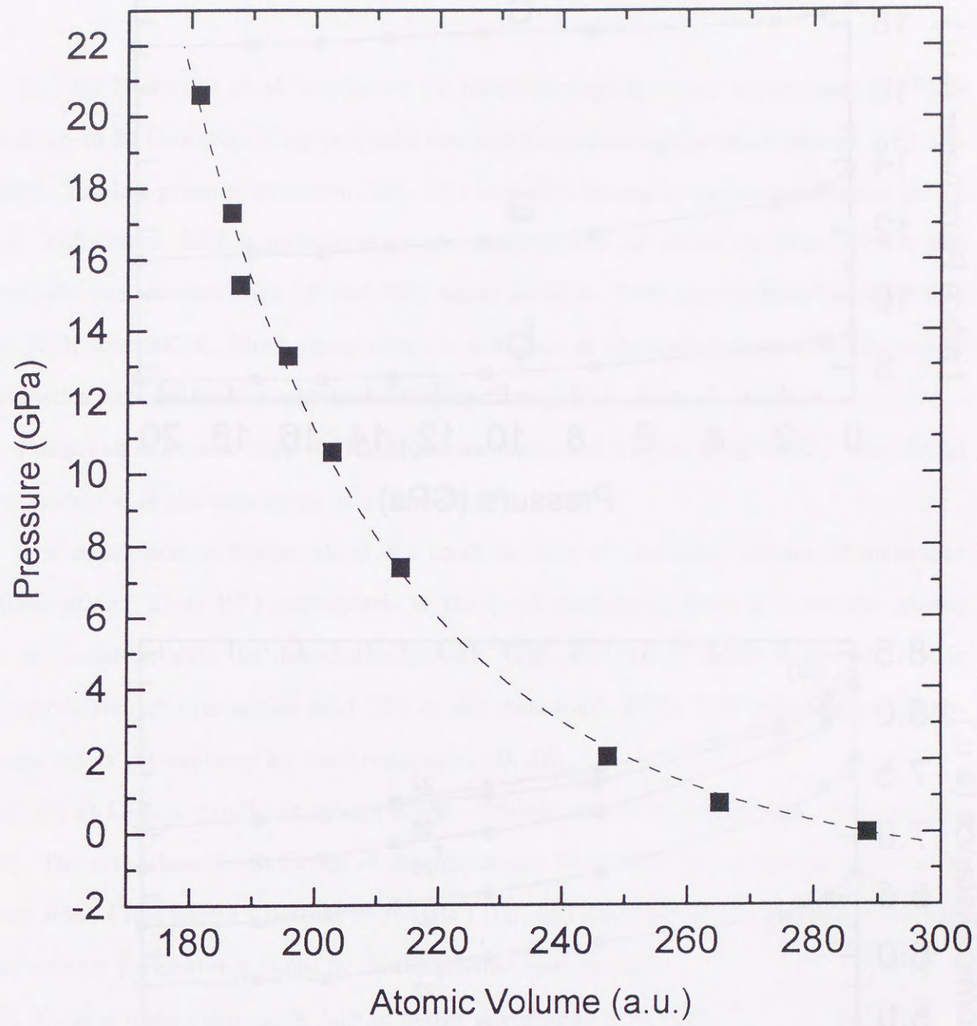

Figure 3: Pressure-volume relation for molecular solid iodine. Filled squares denote the x-ray data obtained by Fujihisa *et al.* [18]. Broken line represents the Murnaghan's EOS fit to the x-ray data.

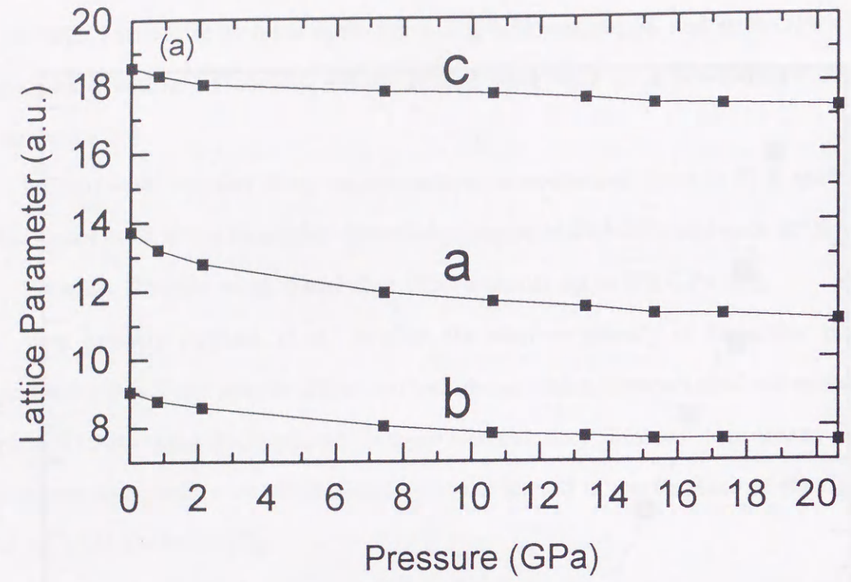

Figure 4: Pressure dependence of (a) lattice parameters and (b) atomic distances where r_{ij} denotes between i and j atoms , obtained by Fujihisa *et al.* [18].

1.1.4 Mössbauer spectroscopy

In 1987 Pasternak *et al.* conducted the Mössbauer spectroscopy experiments in ^{129}I at 4 K up to 30 GPa [20]. They proposed two new molecular high pressure phases, HP1 and HP2. The low pressure structure (LP), HP1 and HP2 belong to the identical space group, i.e. D_{2h}^{18}-$Cmca$. HP1 is metallic state and coexists with LP above 16 GPa. HP2 is also metallic and coexists with LP and HP1 above 24 GPa. They also obtained limited data at 75 K and 300 K, which agree with the 4 K data at the same pressure within poorer statistics imposed by the lower recoil-free fractions [21].

Pasternak *et al.* also observed the Mössbauer isomer shift up to 30 GPa [22]. They found no evidences of the transitions at 16 and 21 GPa.

The conclusion of Pasternak *et al.* conflicts with the previous picture of molecular dissociation. Their HP1 corresponds to the band overlapping state of molecular phase: It is consistent with the dissociation picture. The structure of iodine above 21 GPa is controversial: the molecular solid HP2 or the monatomic BCO. The following points are regarded as the evidence for their conclusion [20, 21]:

(1) At 21 GPa, a significant change of the electrical resistivity has not been observed [9].

(2) The orthorhombic distortion of the monatomic BCO from the tetragonal structure is very small (it is barely 4 percent at 30 GPa) [12], and therefore it cannot explain the high asymmetry parameter η found by the Mössbauer spectroscopy.

(3) Optical measurements [8] fails to detect any change at 21 GPa.

(4) The isomer shift shows no volume change at 21 GPa [22].

(5) Raman studies show that the intramolecular vibration modes remains at and beyond 21 GPa [23, 24, 25].

In Sec.1.3, the points (1), (3), and (5) are compared with the other experimental results reported up to the present. In Chap.5, the points (2) and (4) are studied in detail.

1.1.5 Raman spectra

Shimomura *et al.* studied Raman scattering spectra of iodine up to 21 GPa [23]. They found that the softening of the librational A_g mode above 15 GPa and considered it as a precursor of the molecular dissociation. Hayashi *et al.* studied up to 24.6 GPa and found the softening of the vibrational B_{3g} mode in the vicinity of the molecular dissociation pressure 21 GPa [24]. They observed the complete disappearance of the Raman spectrum at 24.6 GPa and the fact was taken as a strong evidence for the dissociation picture. Olijnyk *et al.* observed six Raman active modes (Fig.2), higher-order Raman spectra, and new bands beside the librational B_{3g} mode above 10 GPa (they labeled as Y) and beside the librational A_g mode above 14 GPa (labeled as X) [25]: The intensity of X increases with increasing pressure and the original peak of the librational A_g mode has nearly vanished around 20 GPa.

1.2 Previous theoretical works

1.2.1 Pressure-induced metallization

From band calculations by using model pseudopotential (PP) method Natsume and Suzuki showed that the high pressure monatomic phase is a "hole-metal", in which the conduction is due to holes [26]. Siringo *et al.* presented crude band calculations for the molecular phase by using linear combination of atomic orbital and reported that the interaction between *bc*-planes exhibits important role for pressure-induced metallization [27]. Detailed calculations by using *ab initio* PP method are presented by Orita and co-workers [28, 29]. They concluded that the band gap closure under pressure has two origins:

(1) As for the conduction band, the interlayer (a-direction) bonding interaction together with the intralayer bonding interaction through the 2-7 atom pair lowers the bottom of the

band when the interatomic distance between the 2-7 atom pair reduce under pressure.

(2) As for the valence band, the intermolecular interaction through the 2-1' atom pair promotes the top of the band as the pressure is increased.

Very recently, Sakamoto *et al.* studied pressure effects on the electron-phonon interaction for FCC phase [30, 31]. Their results are compared with the observed superconducting state [10].

1.2.2 Structural transformations among monatomic phases

Using *ab initio* PP, Orita and co-workers surveyed structural transformations among the monatomic phases [28, 32, 33]. They concluded that both the stability of BCO against BCT and BCT against FCC are resulted by the band Jahn-Teller effect. At the pressure, in which BCT is stable, splitting of the degenerated band at L of FCC in the vicinity of Fermi level stabilizes BCT. At the pressure, in which BCO is stable, splitting of the degenerated band at Z of BCT stabilizes BCO.

1.2.3 Models for structural and dynamical properties

The reason why the $D_{2h}^{18} - Cmca$ is favored in halogen elements is answered by Nyburg [34]. They showed that the "charge migration" caused by the π-antibonding states stabilizes the orthorhombic structure against the cubic $Pa3$ structure. The importance of intermolecular charge distribution is suggested by their model.

Kobashi and Etters calculated the pressure dependence of lattice vibrational modes at $k = 0$ by using a semiphenomenological potential [35]. Their results agree quite well with the pressure dependence of Raman active modes [23, 24, 25], except the softening of librational A_g and vibrational B_{3g} modes.

1.2.4 Models for molecular dissociation

Because the molecular dissociation was found to be reversible [12], Takemura *et al.* considered the transition as the converse of dimerization in the monatomic phase with decreasing pressure [36]. To realize the dimerization, two displacement waves are to be softened. One is a transverse wave with wave vector $\vec{q_1} = \vec{c^*}/8$ with the displacement along the b-axis, where the asterisk on shoulder of the vector denotes the reciprocal lattice vector. The other is a longitudinal wave with wave vector $\vec{q_2} = 2\vec{q_1}$ with the displacement along the c-axis. They concluded that the dimerization transition occurs only in first-order. In Sec.3.3 this model is modified and discussed in detail.

Luty and Raich also considered the dimerization within two-dimensional model for *bc*-plane [37]. They considered that the coupling between the transverse displacement wave and a bond charge wave with $\vec{q_1}$, instead of the longitudinal displacement wave. The effect of the bond charge wave is gathering electrons to the interatomic region, in which the two atoms form the molecule. Their conclusion was supposed as the evidence of existence of a new molecular phase at high pressure region [25], however it should be noticed that Luty and Raich study only the way of forming the "normal" molecular phase. In App.A this model is discussed in detail.

1.3 Purpose of this thesis

From the previous works introduced above, the controversial points for solid iodine under pressure can be summarized as follows:

(I) Are there any relation between the mechanism of molecular dissociation and the observed softening modes of lattice vibrations?

(II) How to compromise the discrepancy between Mössbauer and X-ray experiments?

Concerning with the point (II) above, five grounds are presented by Pasternak *et al.* as introduced in Sec.1.1.4. Here, a part of the grounds are checked as follows:

(1) As introduced in Sec.1.1.2, Sakai *et al.* found the anomaly of the resistivity around 22 GPa [9]. Therefore the evidence of the transition is really observed. In addition, the superconductivity is only found above 21 GPa [10]. This fact suggests that the property of the metallic state is significantly changed at 21 GPa. The anomaly is also observed in recent experiment of Bromine [38] at 80 GPa, which is the molecular dissociation pressure detected by the X-ray experiment [39].

(3) Optical reflectivity of iodine increases drastically at 21 GPa [8]. This fact indicates a significant increase in carrier density as expected for a monatomic phase [40].

(5) Hayashi *et al* reported that the Raman spectra from the molecular vibrations vanished at 24.6 GPa [24]. This fact supports the picture of dissociation.

In the present thesis, we have studied the above two problems by using the first-principles electronic structure calculation method, full-potential linear-muffin-tin-orbital (FP-LMTO) method [41, 42, 43]. All calculations are based on the density functional theory within the local density approximation (LDA) [44]. In Chap.2 the method of calculation is described. In Chap.3 the pressure-induced molecular dissociation is investigated microscopically as the reverse of molecular dimerization. In Chap.4, concerning with (I) above, the frozen-phonon calculation [45] of Raman active A_g modes are presented, in which the pressure-induced softening is confirmed theoretically. It is found that the softening is a precursor of the molecular dissociation and caused by the band overlap. In Chap.5, in relation to (II) above, pressure dependence of contact densities and electric field gradients (EFG), which are related to the isomer shift and the Mössbauer spectroscopy experiments, respectively, are presented under the molecular dissociation picture proposed by X-ray experiments. The consistency for Mössbauer and X-ray experiments are found. In Chap.6, the conclusion is presented.

2 Method of Calculation

2.1 LMTO

In FP-LMTO [41, 42, 43] method, electronic states are described by linear-muffin-tin-orbitals (LMTO) [46]. The crystal space is partitioned into muffin-tin-spheres (MTS) centered at every atomic position and the interstitial region, which is named for the region outside the MTS. Here, the overlap of MTS's is not considered. In the interstitial region, the electronic state is described by the Hankel functions, which are the solutions of the Helmholtz's equation:

$$(-\Delta - \varepsilon) f(\mathbf{r}) = 0, \tag{2}$$

in which the origin is set at atomic position $\mathbf{R}+\mathbf{t}$, where $\mathbf{R}$ is the position of the atom in the unit cell and $\mathbf{t}$ is the translation vector. The Hankel functions are taken with some fixed energy $\varepsilon = \kappa^2$. Inside the MTS, the radial part of the electronic state is described by the linear combination of $\phi_{RL}(\mathrm{r}_R - \mathbf{t}, \varepsilon_{\kappa Rl})$ and it's energy derivative $\dot{\phi}_{RL}(\mathrm{r}_R - \mathbf{t}, \varepsilon_{\kappa Rl})$, where ϕ is the solution of the one-electron Schrödinger (or Dirac) equation inside MTS with the spherically symmetric part of the potential for the energy $\varepsilon_{\kappa Rl}$ which is taken with the center of interest, L denotes the combined index for lm, and $\mathrm{r}_R = \mathrm{r} - \mathbf{R}$. The coefficients of the linear combination are determined with the condition of smooth augmentation to the Hankel function, $K_{\kappa L}(\mathrm{r}_R - \mathbf{t})$, at the boundary of MTS centered at $\mathbf{R}+\mathbf{t}$. Inside any other MTS centered at $\mathbf{R}'+\mathbf{t}'$ the electronic states are also described by the linear combination of ϕ and $\dot{\phi}$, and the coefficients are determined as follows. The tail of the Hankel function is expanded in terms of Bessel functions [47], which are also the solutions of Eq.(2):

$$K_{\kappa L}(\mathrm{r}_R - \mathbf{t}) = \sum_{L'} J_{\kappa L}(\mathrm{r}_R - \mathbf{t}) S_{R'L',RL}(\mathbf{t}' - \mathbf{t}, \kappa), \tag{3}$$

where $S_{R'L',RL}$ is the structure constants in direct space. The coefficients of ϕ and $\dot{\phi}$ centered at $\mathbf{R}'+\mathbf{t}'$ are determined with the condition of smooth augmentation to the each

Bessel functions in Eq.(3). Here, the following definitions are used:

$$K_{\kappa l}(r) = -\frac{i(\kappa\omega)^{l+1}}{(2l-1)!!} h_l(\kappa r), \tag{4}$$

$$J_{\kappa l}(r) = \frac{1}{2}\frac{(2l-1)!!}{(\kappa\omega)^l} j_l(\kappa r), \tag{5}$$

where $h_l = j_l - i n_l$ are the spherical Hankel functions and j_l, n_l are the spherical Bessel and Neumann functions respectively, and ω is the MTS radius. The phase factor of spherical harmonics Y_L to be used is defined after Condon and Shortley [48], and $f_L \equiv i^l Y_L f_l$, where f is $K, J, \phi, \dot{\phi}$, and so on. The expression for the structure constant is

$$\begin{aligned} S_{R'L',RL}(\mathbf{t},\kappa) &= \sum_{L''} \frac{8\pi(2l''-1)!!}{(2l'-1)!!(2l-1)!!} C^{L''}_{LL'} (\kappa\omega)^l (\kappa\omega')^{l'} (\kappa\omega'')^{-l''} \\ &\quad \times K_{\kappa l''}(|\mathbf{t} - \mathbf{R}' + \mathbf{R}|)(-i)^{l''} Y^*_{L''}(\mathbf{t} - \hat{\mathbf{R}}' + \mathbf{R}), \end{aligned} \tag{6}$$

where $C^{L''}_{LL'}$ is the Gaunt coefficients:

$$C^{L''}_{LL'} = \int d\hat{\mathbf{r}} Y_L(\hat{\mathbf{r}}) Y^*_{L'}(\hat{\mathbf{r}}) Y_{L''}(\hat{\mathbf{r}}). \tag{7}$$

The last step is to perform the Bloch sum of the LMTO's centered at different sites, and finally obtained as in the form

$$\chi^{\mathbf{k}}_{\kappa RL}(\mathrm{r}) = \Phi^K_{\kappa RL}(\mathrm{r}_R)\delta_{RR'} + \sum_{L'} \Phi^J_{\kappa R'L'}(\mathrm{r}_{R'}) S^{\mathbf{k}}_{R'L',RL}(\kappa) \quad \text{for } |\mathrm{r} - \mathrm{R}'| < s_{R'}, \tag{8}$$

$$= \sum_{\mathbf{t}} e^{i\mathbf{k}\mathbf{t}} K_{\kappa L}(\mathrm{r}_R - \mathbf{t}) \quad \text{for } \mathbf{r} \text{ at the interstitial region}, \tag{9}$$

where s_R is the MTS radius for the atom included in the sublattice 'R' and

$$S^{\mathbf{k}}_{R'L',RL}(\kappa) = \sum_{\mathbf{t}\neq 0} e^{i\mathbf{k}\mathbf{t}} S_{R'L',RL}(\mathbf{t},\kappa). \tag{10}$$

The functions $\Phi^K_{\kappa RL}(\mathrm{r}_R)$ and $\Phi^J_{\kappa RL}(\mathrm{r}_R)$ are the linear combination of ϕ_{RL} and $\dot{\phi}_{RL}$, in which the functions match smoothly to Hankel and Bessel functions at the MTS boundary respectively as described above.

In the present calculations, lattice Fourier transformation is performed to get the numerical values of the Hankel functions in the interstitial region [41]. To improve the convergence

with respect to the number of reciprocal lattice vectors, the solution of the following equation is used instead of the Hankel function $K_{\kappa L}(\mathrm{r})$ [49]:

$$(-\Delta - \kappa^2) f(\mathbf{r}) = \frac{4\pi(\frac{\xi^2}{\pi})^{\frac{3}{2}}(2\xi^2)^l \omega^{l+1} e^{\kappa^2/(2\xi)^2}}{(2l-1)!!} r^l e^{-(\xi r)^2} i^l Y_L(\hat{\mathbf{r}}), \tag{11}$$

where the Gaussian damping parameter is defined by the following relation,

$$\frac{(\omega\xi_l^2)^{l+2}\ e^{-(\omega\xi_l^2)^2}}{(G_{cut}/2\xi_l^2)^l\ e^{-(G_{cut}/2\xi_l^2)^2}} = \text{const.} \tag{12}$$

In Eq.(12), the right hand side is set as 0.5 in the present work and G_{cut} is the absolute value of maximum reciprocal lattice vector to be used, which is defined by numerical and computational conditions.

2.2 Hamiltonian and overlap matrix

With the LMTO basis set defined in (8) and (9) the wave functions $\psi_{\mathbf{k}\lambda}(\mathbf{r})$ for valence electrons, where λ denotes the bands, are represented as linear combinations of LMTO's with the coefficients $A^{\mathbf{k}\lambda}_{\kappa RL}$ obtained from the variational principle. For the one-electron Hamiltonian given by LDA they are found from the generalized eigenvalue problem:

$$\begin{aligned} &\sum_{\kappa RL}\left[< \chi^{\mathbf{k}}_{\kappa' R' L'}| -\Delta + V^{MT}(\mathbf{r}) + V^{NMT}(\mathbf{r})|\chi^{\mathbf{k}}_{\kappa RL} > -\varepsilon_{\mathbf{k}\lambda} < \chi^{\mathbf{k}}_{\kappa' R' L'}|\chi^{\mathbf{k}}_{\kappa RL} >\right] A^{\mathbf{k}\lambda}_{\kappa RL} \\ \equiv &\sum_{\kappa RL}\left(H^{\mathbf{k}}_{\kappa' R' L', \kappa RL} - \varepsilon_{\mathbf{k}\lambda} O^{\mathbf{k}}_{\kappa' R' L', \kappa RL}\right) A^{\mathbf{k}\lambda}_{\kappa RL} \ = \ 0, \end{aligned} \tag{13}$$

where $V^{MT}(\mathbf{r})$ stands for the spherical and $V^{MT}(\mathbf{r})$ for nonspherical parts of the potential.

2.3 Density and potential

The valence density is calculated as follows:

$$n^v(\mathbf{r}) = 2\sum_{\mathbf{k}\lambda}\sum_{\kappa RL}\sum_{\kappa' R' L'} A^{\mathbf{k}\lambda^*}_{\kappa' R' L'} A^{\mathbf{k}\lambda}_{\kappa RL} \chi^{\mathbf{k}^*}_{\kappa R' L'}(\mathrm{r})\chi^{\mathbf{k}}_{\kappa RL}(\mathrm{r}). \tag{14}$$

The electronic density inside MTS is expressed as

$$\hat{n}_R(\mathbf{r}) = \sum_L \hat{n}_{RL}(r) i^l Y_L(\hat{\mathbf{r}}), \tag{15}$$

where the core electron density is included in $L = 0$ term. The electronic density in the interstitial region is expressed as

$$\tilde{n}(\mathbf{r}) = \sum_{\mathbf{G}} \tilde{n}(\mathbf{G}) e^{i\mathbf{G}\cdot\mathbf{r}}. \tag{16}$$

The Hartree potential is calculated by solving Poisson's equation for the total charge density ρ. The auxiliary charge Γ is introduced [41] to compensate the multipole moments of charge densities in MTS under the following condition:

$$\int_0^{s_R} [\hat{n}_{LR} + \sqrt{4\pi} n^N_R(r)\delta_{l,0} - \Gamma_{RL}(r)] r^{l+2} dr = 0, \tag{17}$$

where $n^N_R(r)$ denotes the nuclear charge density. If Eq.(17) is fulfilled, the densities inside MTS could not produce an electrostatic field outside its own sphere. The influence of the charges in the given MTS on the rest of the crystal is completely described by the field produced by the Γ, which is added to the ρ to be canceled out. Poisson's equation for $\tilde{n} + \Gamma$ is solved by Fourier transformation. The auxiliary density Γ must be localized inside MTS and be smooth enough to ensure a fast convergence of the Fourier series. The Gaussian type auxiliary density is used in the present calculations [49]

$$\Gamma_{RL}(\mathbf{r}) = d_{RL} r^l e^{-(\xi_{RL} r)^2} i^l Y_L(\hat{\mathbf{r}}), \tag{18}$$

where the damping constant ξ is also defined by Eq.(12) with the following condition:

$$G^{\text{orbit.}}_{cut} \leq G^{\text{dens.}}_{cut}, \tag{19}$$

and the coefficient d_{RL} is defined by the condition Eq.(17).

The Hartree potential in MTS is written as

$$\hat{V}^H(\mathbf{r}) = \sum_L \hat{V}^H_{RL}(r) i^l Y_L(\hat{\mathbf{r}}), \tag{20}$$

where

$$\hat{V}^H_{RL}(r) = \frac{8\pi}{2l+1}\left[\frac{1}{r^{l+1}}\int_0^r x^{l+2}\hat{\rho}_{RL}(x)dx + r^l\int_r^{s_R} x^{1-l}\hat{\rho}_{RL}(x)dx + r^l\sum_{\mathbf{G}} 4\pi Y^*_L(\hat{\mathbf{G}})G^{-1}s_R^{1-l}j_{l-1}(Gs_R)[\tilde{n}(\mathbf{G})+\Gamma(\mathbf{G})]\right] \quad (21)$$

and

$$\hat{\rho}_{RL}(x) = \hat{n}_{RL}(r) + \sqrt{4\pi}n^N_R(r)\delta_{l,0}. \quad (22)$$

In the interstitial region

$$\tilde{V}^H(\mathbf{r}) = \sum_{\mathbf{G}}\frac{8\pi}{G^2}[\tilde{n}(\mathbf{G})+\Gamma(\mathbf{G})]e^{i\mathbf{G}\cdot\mathbf{r}}. \quad (23)$$

In MTS the exchange-correlation potential within LDA is written as

$$\hat{v}^{xc}(\mathbf{r}) = \sum_L \hat{v}^{xc}_{RL}(r)i^l Y_L(\hat{\mathbf{r}}). \quad (24)$$

For $r > 0.03Z^{\frac{1}{3}}a_0$, where Z is the atomic number and a_0 is Bohr radius, the numerical integration is performed to obtain the L component:

$$\hat{v}^{xc}_{RL}(r) = \int d\hat{\mathbf{r}}v^{xc}[\hat{n}_R(\mathbf{r})]\left(i^l Y_L(\hat{\mathbf{r}})\right)^*. \quad (25)$$

For $r \leq 0.03Z^{\frac{1}{3}}a_0$ a Taylor expansion is performed: the spherical (MT) part of the density is taken as a large part and the non-spherical (NMT) part as a small part [41]:

$$\hat{v}^{xc}_{RL=0}(r)/\sqrt{4\pi} = v^{xc}[n^{MT}(r)] + \frac{1}{4\pi}\frac{1}{2}v^{xc"}[n^{MT}(r)]\sum_{L'>0}(\hat{n}_{RL'}(r))^2$$
$$\hat{v}^{xc}_{RL>0}(r) = v^{xc'}[n^{MT}(r)]\hat{n}_{RL}(r) + \frac{1}{2}\sum_{L',L">0} v^{xc"}[n^{MT}(r)]\hat{n}_{RL'}(r)\hat{n}_{RL"}(r)C^{L"}_{LL'}, \quad (26)$$

where $v^{xc'}$ and $v^{xc"}$ are the first and second derivative of v^{xc} with respect to the density.

In the interstitial region, the exchange-correlation potential is represented as a Fourier sum. The coefficients are determined via a three-dimensional numerical integration over the unit cell:

$$\tilde{v}^{xc}(\mathbf{G}) = \frac{1}{\Omega_{cell}}\int d\mathbf{r}v^{xc}[\tilde{n}(\mathbf{r})]e^{-i\mathbf{G}\cdot\mathbf{r}}. \quad (27)$$

2.4 Total energy

The total energy is divided into following parts:

$$E_{\text{tot}} = E_{\text{kin}} + E_{\text{H}} + E_{\text{xc}}. \quad (28)$$

The kinetic energy part is written as

$$E_{\text{kin}} = \sum_{\mathbf{k}\lambda} f_{\mathbf{k}\lambda}\varepsilon_{\mathbf{k}\lambda} + \sum_{iR} f_{iR}\varepsilon_{iR} - \sum_R\int_{\text{MTS}} d\mathbf{r}\hat{\rho}_R(\mathbf{r})\hat{V}_R(\mathbf{r}) - \sum_{\mathbf{G}}\tilde{n}^*(\mathbf{G})\sum_{\mathbf{G}'}\tilde{V}(\mathbf{G}')\int_{\text{INT.}} d\mathbf{r}\, e^{i(\mathbf{G}'-\mathbf{G})\mathbf{r}}, \quad (29)$$

where $f_{\mathbf{k}\lambda}$ is the weight of $\mathbf{k}$-points sampling and f_{iR} is an occupation number for i-th core level, ε_{iR}.

Coulomb energy part is written as

$$E_{\text{H}} = \frac{1}{2}\sum_R\int_{\text{MTS}} d\mathbf{r}\hat{\rho}_R(\mathbf{r})\hat{V}^H_R(r) + \frac{1}{2}\sum_{\mathbf{G}}\tilde{n}^*(\mathbf{G})\sum_{\mathbf{G}'}\tilde{V}^H(\mathbf{G}')\int_{\text{INT.}} d\mathbf{r}\, e^{i(\mathbf{G}'-\mathbf{G})\mathbf{r}}. \quad (30)$$

For $r > 0.03Z^{\frac{1}{3}}a_0$ and in the interstitial region, the exchange-correlation energy is calculated in usual procedures. For $r \leq 0.03Z^{\frac{1}{3}}a_0$, the exchange-correlation energy is evaluated by the Taylor expansion up to the second order [41].

2.5 Computational details

The exchange-correlation functional formula proposed by von Barth and Hedin [50] is adopted in present work. Inside MTS, the scalar-relativistic calculations are performed for valence electrons [51]. The core states are recalculated at each self-consistent iteration with relativistic effects [52]. For $\mathbf{k}$-points sampling, the improved tetrahedron method is used [53].

In FP-LMTO, MTS's should not be overlapped. For the open structure materials, to describe the electronic states at the wide interstitial region correctly by LMTO, empty spheres are usually used. However I could not find the suitable position to set the empty sphere for the structure of molecular solid iodine. Although empty spheres are not used, the multiple-κ method provides correct structural and dynamic properties for open structures [42]. Throughout all the calculations, the MTS radius, s_R, is settled in 2.558 a_0, slightly short length from the half of molecular axis at zero pressure.

The iodine nucleus is treated as uniformly charged sphere, where the radius $R_{nuc} = 6$ fm, and the contact densities are obtained by averaging the electronic densities inside R_{nuc}.

The numerical conditions are determined by the following quantities as discussed above: Number of envelope functions, i.e. Hankel functions, per atom and their energies, κ^2, number of reciprocal lattice vectors to expand the densities and the envelope functions at the interstitial region, maximal angular momentum to expand the densities and the basis inside MTS, and number of **k**-points sampling.

2.5.1 Tests for FCC iodine

Here, total energy convergence for monatomic FCC iodine with the atomic volume V_0 is surveyed. The atomic volume V_0 is the value of the molecular phase at ambient pressure and the rate of the interstitial region is 75.7 percent.

Firstly the convergence with respect to the number of reciprocal lattice vectors is surveyed. The other conditions are set as follows. Basis set is presented for $5s5p$ with $\kappa^2 = 0.5 + 0.003i$ Ry and for $4d$ with $\kappa^2 = -2.5$ Ry, in which small imaginary number is added to the positive κ^2 to avoid the singularity [43]. The value of κ^2 is selected around the band center. Inside the irreducible Brillouin zone (IBZ) 47 **k**-points are sampled. Densities and the envelope functions inside MTS are expanded up to $l_{max} = 8$. Number of reciprocal lattice vectors to expand the envelope functions for $5p$ is set about one eighth of the

number for densities. Total energy convergence with respect to the number of reciprocal lattice vectors for densities is shown in Fig.5. The convergence within 0.5 mRy is obtained over 1700 vectors per atom. Hereafter the cutoff energy $E_c = 50\ (V/V_0)^{-\frac{2}{3}}$ Ry is adopted for the number of the vectors.

Secondly the convergence with respect to the number of **k**-points sampling is surveyed. The cutoff energy equals 50 Ry and the other conditions are same as above. The result is presented in Fig.6 and the convergence within 0.1 mRy is obtained over 72 points inside IBZ. This number of sampling corresponds to 163 points for monatomic BCT and 280 points for monatomic BCO inside IBZ.

Thirdly the convergence with respect to the LMTO basis set is surveyed. The cutoff energy equals 50 Ry, 72 **k**-points are sampled, and $l_{max} = 8$. Total energy of the starting basis set with 9 LMTO's/atom, i.e., for $5s5p$ with $\kappa^2 = 0.5 + 0.003i$ Ry and for $4d$ with $\kappa^2 = -2.5$ Ry, is compared with the several basis sets. The $5s$ and $5p$ orbitals are added with $\kappa^2 = -0.5$ Ry and $\kappa^2 = -1.5$ Ry, $5d$ are added with $\kappa^2 = 0.5 + 0.003i$ Ry, $\kappa^2 = -0.5$ Ry, and $\kappa^2 = -1.5$ Ry, and $4f$ are added with $\kappa^2 = 0.5 + 0.003i$ Ry. Maximum changes of total energies with addition of the orbitals are tabulated in Table I. The mRy order convergence is obtained by 22 LMTO's/atom basis set: for $5s5p5d$ with $\kappa^2 = 0.5 + 0.003i$ Ry, for $5s5p$ with $\kappa^2 = -0.5$ Ry and $\kappa^2 = -1.5$ Ry, and for $4d$ with $\kappa^2 = -2.5$ Ry. Hereafter the calculations are performed by using this basis set.

Finally the convergence with respect to the maximal angular momentum to expand the densities and the basis inside MTS is surveyed. Cutoff, **k**-points sampling, and basis set are used above results. The total energy changes from $l_{max} = 8$ to $l_{max} = 10$ and 12 are only 0.01 mRy order. Hereafter the calculations are performed with $l_{max} = 8$.

The total energy of monatomic FCC iodine is calculated as a function of atomic volume. The results are shown in Fig.7 and are fitted to the Murnaghan's EOS [19]:

$$E(V) = \frac{B_0 V}{B_0'}\left[\frac{1}{B_0' - 1}\left(\frac{V_0}{V}\right)^{B_0'} + 1\right] + \text{const.} \tag{31}$$

The parameters are obtained as follows: $B_0 = 36.774$ GPa, $B_0' = 4.2688$, and $V_0 = 210.44$

a.u. In the previous studies these parameters are determined as follows: $B_0 = 49.7$ GPa, $B_0' = 4.13$, and $V_0 = 205$ a.u. by using *ab initio* PP [32], and $B_0 = 38.5$ GPa, $B_0' = 4.25$, and $V_0 = 210$ a.u. by using full-potential linearized augmented-plane-wave (FLAPW) method [30]. In Table II the values of theoretical pressure for the lattice constant $a = 4.238$ Å (8.009 a.u.) are compared with the experimental value [14] and the theoretical results. The results of present work quite agree with these previous results.

Table I: Maximum changes of the total energies with increasing basis size in mRy/atom. The starting basis set is 9 LMTO's/atom with $\kappa^2 = 0.5 + 0.003i$ Ry for $5s5p$ and $\kappa^2 = -2.5$ Ry for $4d$.

Orbitals	$\kappa^2 =$ 0.5 Ry	-0.5 Ry	-1.5 Ry	-2.5 Ry
$4d$	—	—	—	0
$5s$	0	-2103.8	-6.0	—
$5p$	0	-852.0	-39.4	—
$5d$	-556.2	-0.82	-0.53	—
$4f$	-1.1	—	—	—

Table II: The pressure of monatomic FCC iodine for the lattice constant $a = 4.238$ Å(8.009 a.u.).

	Theoretical			Experimental
	FP-LMTO	*ab initio* PP	FLAPW	X-ray
Reference	present	[32]	[30]	[14]
Pressure (GPa)	62.3	71.0	63.8	64

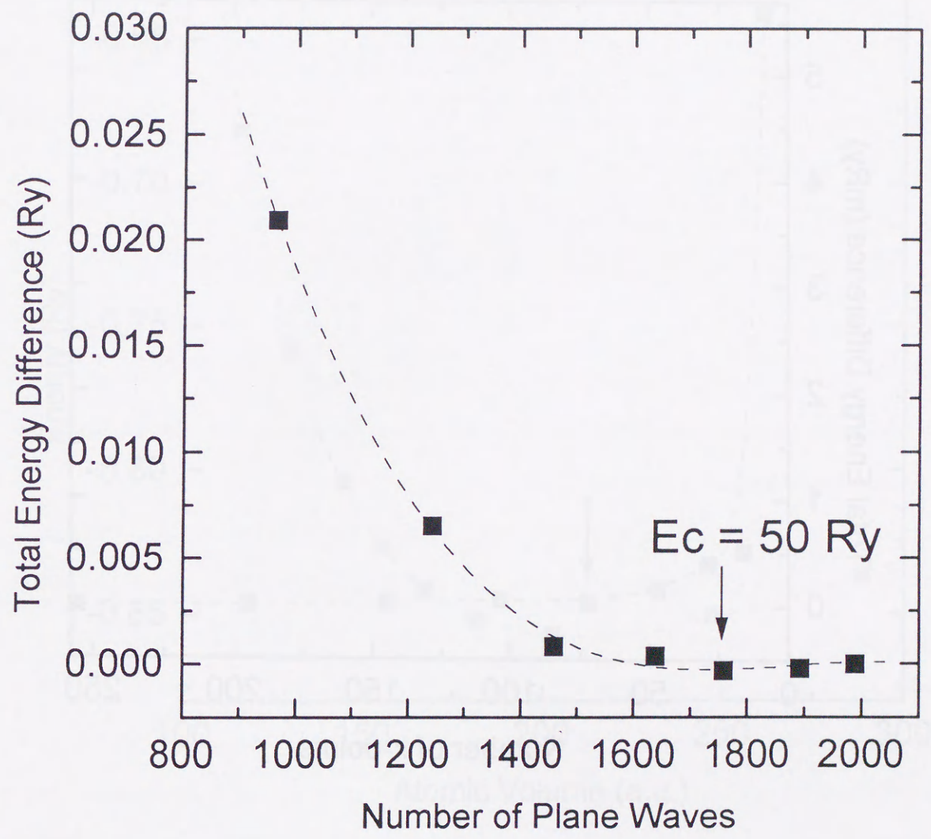

Figure 5: Total energy of monatomic FCC iodine versus number of plane waves to expand the densities. The broken line is guide to eye. The cutoff is selected with the cutoff energy 50 Ry.

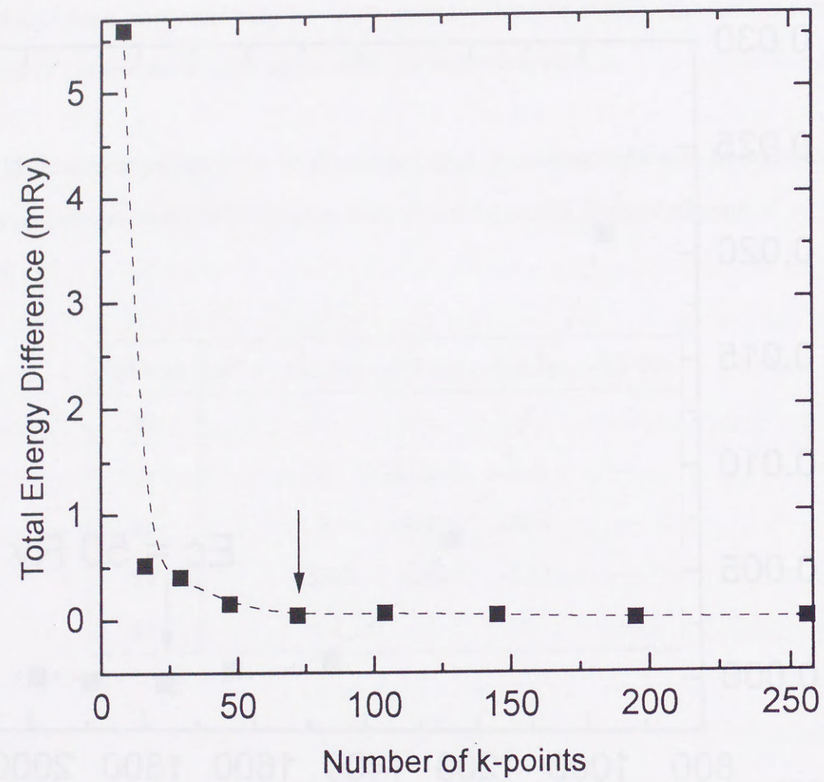

Figure 6: Total energy of monatomic FCC iodine versus number of **k**-points sampling inside IBZ. The broken line is guide to eye.

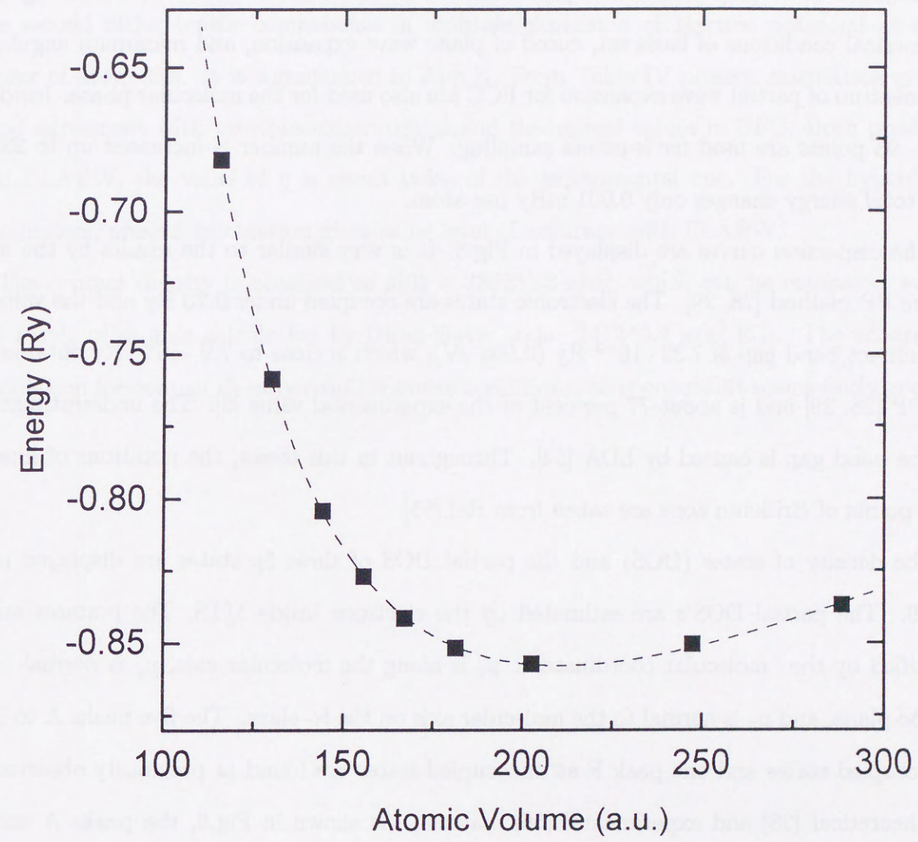

Figure 7: Total energy of monatomic FCC iodine versus atomic volume. Broken line represents the Murnaghan's EOS fit to the calculated results.

2.5.2 Tests for molecular solid iodine

In this section test calculations are presented for the structure at zero pressure determined by Fujihisa *et al.* [18]: The lattice parameters and atomic positions are shown in Fig. 4. Numerical conditions of basis set, cutoff of plane wave expansion, and maximum angular momentum of partial wave expansion for FCC are also used for the molecular phase. Inside IBZ, 93 points are used for **k**-points sampling. When the number is increased up to 228 the total energy changes only 0.001 mRy per atom.

The dispersion curves are displayed in Fig.8: It is very similar to the results by the *ab initio* PP method [28, 29]. The electronic states are occupied under 0.73 Ry and the value of indirect band gap is $7.32 \cdot 10^{-2}$ Ry (0.996 eV), which is close to $7.9 \cdot 10^{-2}$ Ry obtained by PP [28, 29] and is about 77 per cent of the experimental value [6]. The underestimate of the band gap is caused by LDA [54]. Throughout in this thesis, the notations of lines and points of Brillouin zone are taken from Ref.[55].

The density of states (DOS) and the partial DOS of three $5p$ states are displayed in Fig.9. The partial DOS's are estimated by the electrons inside MTS. The p states are specified by the "molecular coordinates": p_z is along the molecular axis, p_y is normal to the bc-plane, and p_x is normal to the molecular axis on the bc-plane. The five peaks A to E at occupied states and one peak F at unoccupied states are found as previously observed by theoretical [28] and experimental [56] manner. As shown in Fig.9, the peaks A and F mainly consist of σ and σ^* respectively, and E consists of π_y^*. The peaks B, C, and D consist of both π_y and π_x (and their antibonding states).

The density map on the bc-plane is displayed in Fig.10 in the unit of electrons per Å^3 (e/Å^3). The formation of diatomic molecules can be shown as experimental [17] and theoretical [28] results. In Table III, the densities at the center of interatomic positions are compared with the experimental results [17]: The calculated results show fairly good agreement with the experimental one.

The value of EFG at the nucleus and the asymmetry parameter of EFG η are tabulated in Table IV and are compared with the Mössbauer [57] and FLAPW [58] results. The experimental value is represented in V/m^2 with the nuclear quadrupole moment $Q = -0.55$ barn (10^{-28}m^2) for ^{129}I [59]. In present work, the value of EFG is calculated by the second order tensor components in multiple expansion of Hartree potential at the center of atom [60]. It is summarized in App.B. From Table IV present calculation gives good agreement with previous experimental and theoretical values in EFG. Both present and FLAPW, the value of η is about twice of the experimental one. For the hyperfine parameters, present calculation gives same level of accuracy with FLAPW.

The contact density is obtained as $\rho(0) = 238251.6\ \text{e/a}_0^3$, which can be compared with the result of atomic calculation by Dirac-Slater code: $241240.4\ \text{e/a}_0^3$ [61]. The accurate calculation for contact density requires severe conditions, thus our result seems fairly good.

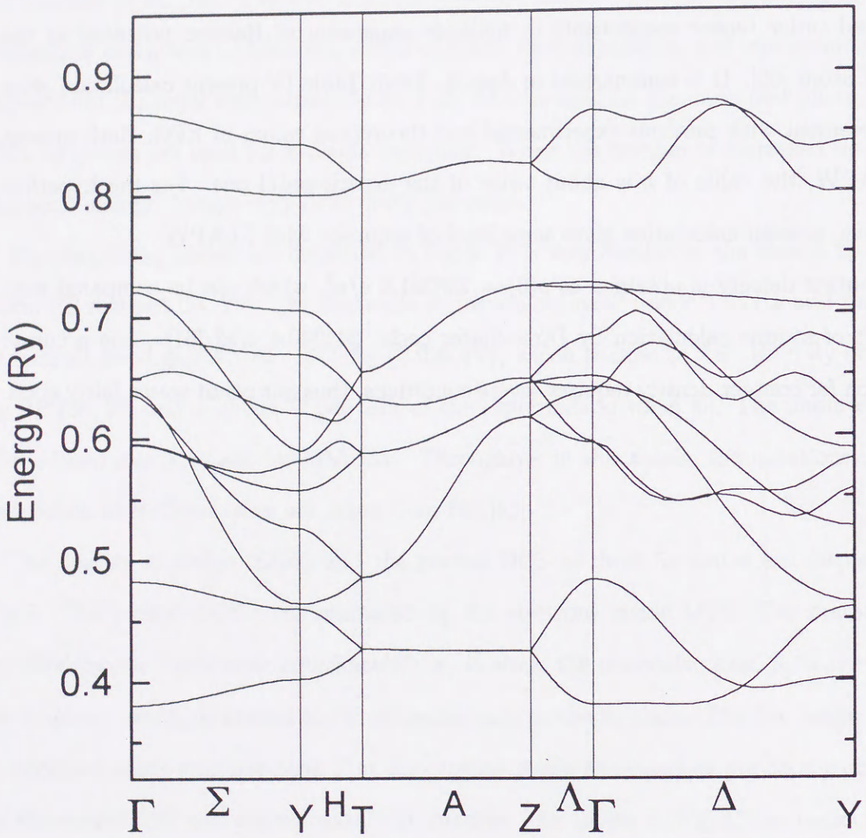

Figure 8: Dispersion curve of molecular solid iodine at ambient pressure.

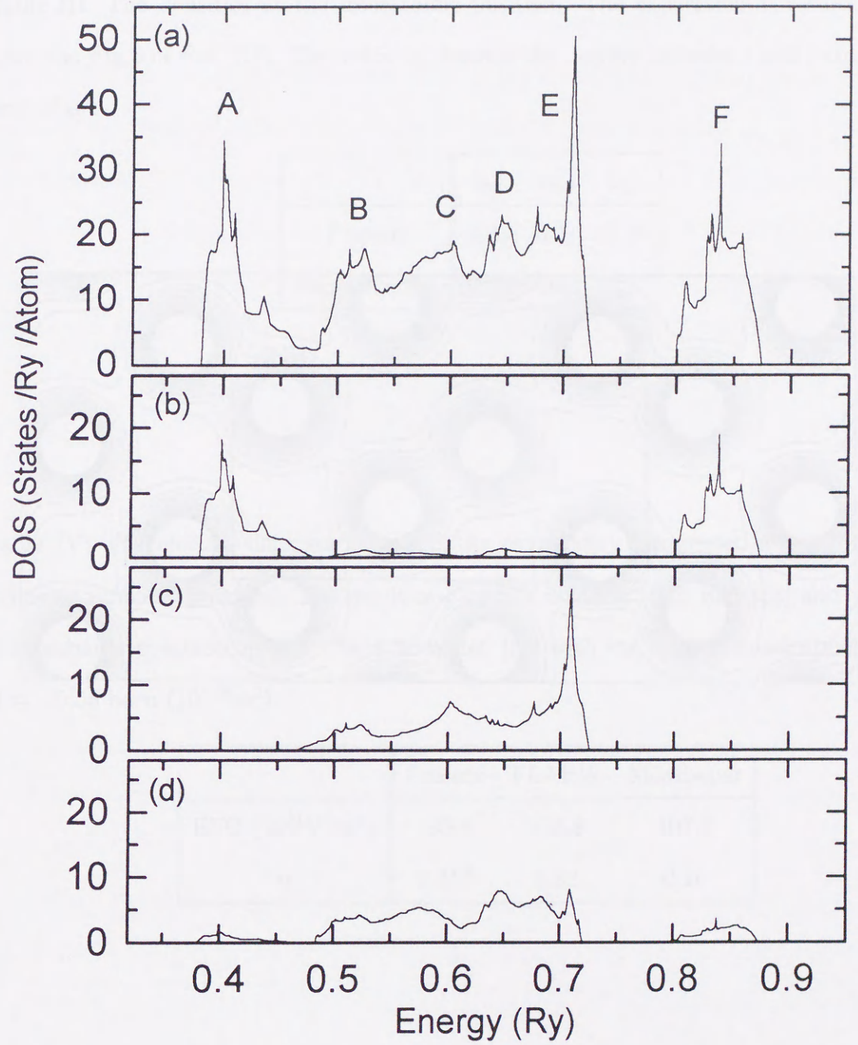

Figure 9: The total and partial density of states of molecular solid iodine at ambient pressure. The total DOS is presented in (a), partial DOS for $5p_z$ is in (b), $5p_y$ is in (c), and $5p_x$ is in (d). In this notation, z is set along the molecular axis, y is normal to the bc-plane, and x is on the bc-plane.

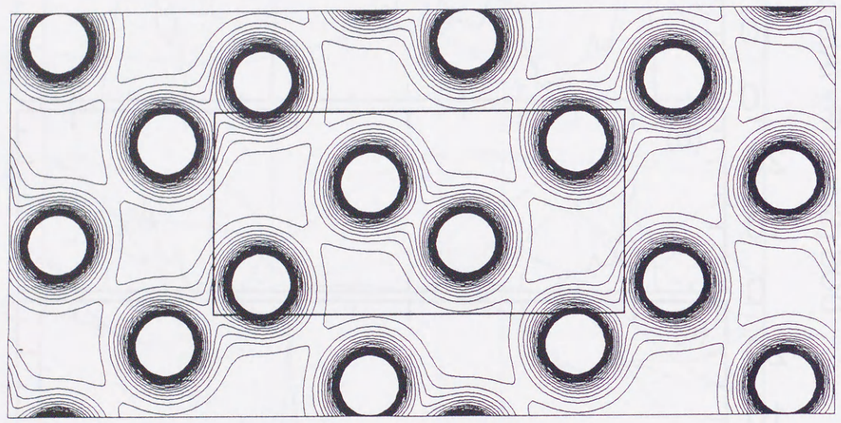

Figure 10: Density map of molecular solid iodine on the *bc*-plane at ambient pressure. The rectangle inside the figure denotes the unit cell. The contour values are given in 0.1 e/Å^3 and are drawn from 0.1 to 2.5 e/Å^3.

Table III: The densities at the interatomic position. The experimental results are read from the Fig.3 of Ref. [17]. The value b_{ij} denotes the density between i and j atoms in the unit of e/Å^3.

	b_{21}	b_{27}	$b_{21'}$
Present	0.43	0.11	0.05
Experimental	0.46	0.16	0.07

Table IV: The electric field gradient and the asymmetry parameter of molecular solid iodine at ambient pressure. The result of FLAPW is taken from Ref. [58] and the result of Mössbauer spectroscopy for ^{129}I is from Ref. [57] with the nuclear quadrupole moment $Q = -0.55$ barn (10^{-28}m^2).

	Present	FLAPW	Mössbauer
EFG (10^{21}V/m^2)	103.8	118.8	107.2
η	0.317	0.32	0.16

2.5.3 Tests of frozen-phonon calculation

Previously frozen-phonon calculation of solid iodine was performed only for FCC by using FLAPW [31]. To check the accuracy of the numerical conditions to be used, the frozen-phonon calculation at X-point of FCC is performed. The representation of symmetry at X-point is isomorphic with the D_{4h} point group. There are two normal modes at X-point: A_{2u} longitudinal and E_u transverse modes. These normal modes could be described by the one dimensional oscillator with the atomic mass M. Total energies with the atomic displacement $u = 0.007a, 0.014a$, and $0.021a$ are fitted to the equation:

$$E_{tot} = E_0 + \frac{1}{2}M\omega^2 u^2 + ku^4, \tag{32}$$

where E_0 denotes the total energy with $u = 0$. The results of the longitudinal and the transverse modes with the lattice constant $a = 4.335$ Å are tabulated in Table V. The results quite agree with the previous work for the frequencies, however the 4th order anharmonic parameters agree only in order.

To check the effects of using no empty spheres for frozen-phonon calculation, phonon frequencies of the typical open structure, the diamond structure of silicon, are calculated with 17 LMTO's/atom, i.e., for $3s3p$ with $\kappa^2 = 0.5 + 0.003i, -0.5$, and -1.5 Ry and for $3d$ with $\kappa^2 = 0.5 + 0.003i$ Ry. The results of LTO(Γ) and k_{xyz} are tabulated in Table VI and are compared with the previous experimental [62, 63], FP-LMTO [42], FLAPW [64], and PP [45] results. For both the frequency and the anharmonic parameter k_{xyz}, excellent agreement with the previous results are obtained.

Table V: The phonon frequency ω and the 4th order anharmonic parameter k at X-point of FCC iodine with $a = 4.335$ Å. The result of FLAPW is taken from Ref. [31]. The suffixes L and T denote A_{2u} longitudinal and E_u transverse modes respectively.

	Present	FLAPW
ω_L (cm^{-1})	248	231
ω_T (cm^{-1})	163	159
k_L (Ry/Å^4)	2.68	4.62
k_T (Ry/Å^4)	1.15	0.82

Table VI: The phonon frequency of LTO(Γ) and the 3rd order anharmonic parameter k_{xyz} of diamond silicon.

	Present	FP-LMTO	FLAPW	*ab initio* PP	Experiment
LTO(Γ) (THz)	15.15	15.47[a]	15.37[c]	15.16[d]	15.53[e]
		15.43[b]			
k_{xyz} (eV/Å^3)	−35.3	−38.7[a]	−37.0[c]	−32.8[d]	−35.1[f]
		−39.6[b]			

[a] Reference [42].

[b] Reference [43].

[c] Reference [64].

[d] Reference [45].

[e] Reference [62].

[f] Reference [63].

3 Pressure-Induced Molecular Dissociation

3.1 Hierarchy of crystal structures

All the structures appeared in the structural transformation of solid iodine are classified within the distorted one of FCC.

Apparently BCT is the distorted structure from FCC with respect to one of a cubic lattice parameter. As appeared in Introduction, the mechanism is surveyed by Orita *et al.* [28, 32].

The structures at lower pressure are formed by the atomic deformations within the xy-plane of BCT[36, 37]. Hereafter in monatomic structures the xy-plane denotes the layer in which atoms are forming squares in BCT. The xy-plane represents the bc-plane of the molecular phase. The lattice parameters are represented by a_i, b_i, and c_i for x, y, and z directions respectively under the condition $c_i > b_i \geq a_i$.

The BCO structure is the distorted one from BCT within the elastic distortion of B_{1g} symmetry as displayed in Fig.A-2 of App.refapdx-BC. The mechanism is also investigated by Orita *et al.* as the band Jahn-Teller effect [28, 33]. It can be also understood by the bond charge model [37] as discussed in App.A.

The molecular dissociation is found to be reversible, and therefore it can be regarded conversely as dimerization in monatomic phase with decreasing pressure [36]. In [36], however, Takemura *et al.* considered BCO as the undistorted structure. Then the realized molecular phase is monoclinic as displayed in Fig.5 of Ref.[36]. If the undistorted structure is the monatomic face-centered orthorhombic (FCO) one with the space group $D_{2h}^{23} - Fmmm$, then the molecular phase is to be orthorhombic $D_{2h}^{18} - Cmca$ within their model as discussed in Sec.3.3. The FCO structure is the distorted one from BCT within the elastic distortion of B_{2g} symmetry as displayed in Fig.A-2. Therefore the continuous transition, i.e. the second-order transition, could not be occurred between BCO and the molecular phase. Of

course, the observed transition is the first-order [12].

Table VII: Total and partial DOS's of BCT, BCO, and FCO at the Fermi level.

	BCT	BCO	FCO
DOS	7.9329	7.6392	7.9313
p_z	1.5304	1.4756	1.5369
p_y	2.0240	2.0479	2.0545
p_x	2.0240	1.8488	1.9863

Table VIII: Bond charges of BCT, BCO, and FCO in e/Å^3.

	BCT	BCO	FCO
b_x	0.3054	0.3357	0.3035
b_y	0.3054	0.2793	0.3035

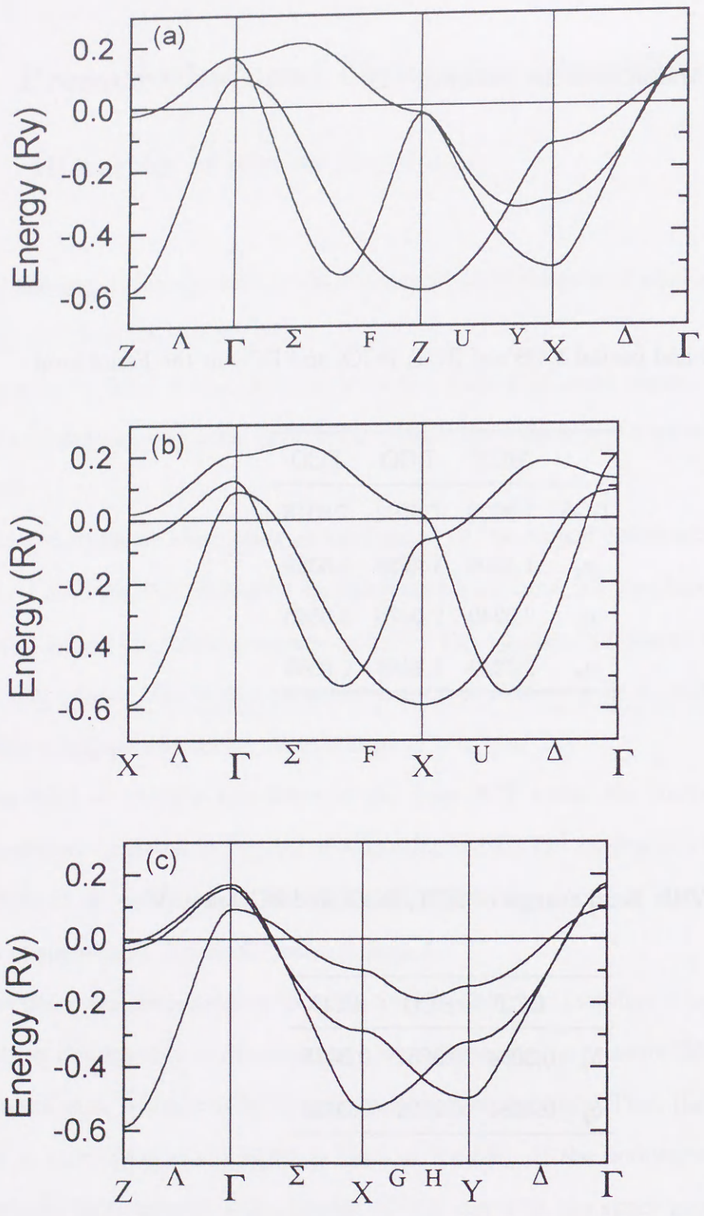

Figure 11: Band structures of (a) BCT, (b) BCO, and (c) FCO. Energies are measured from the Fermi levels.

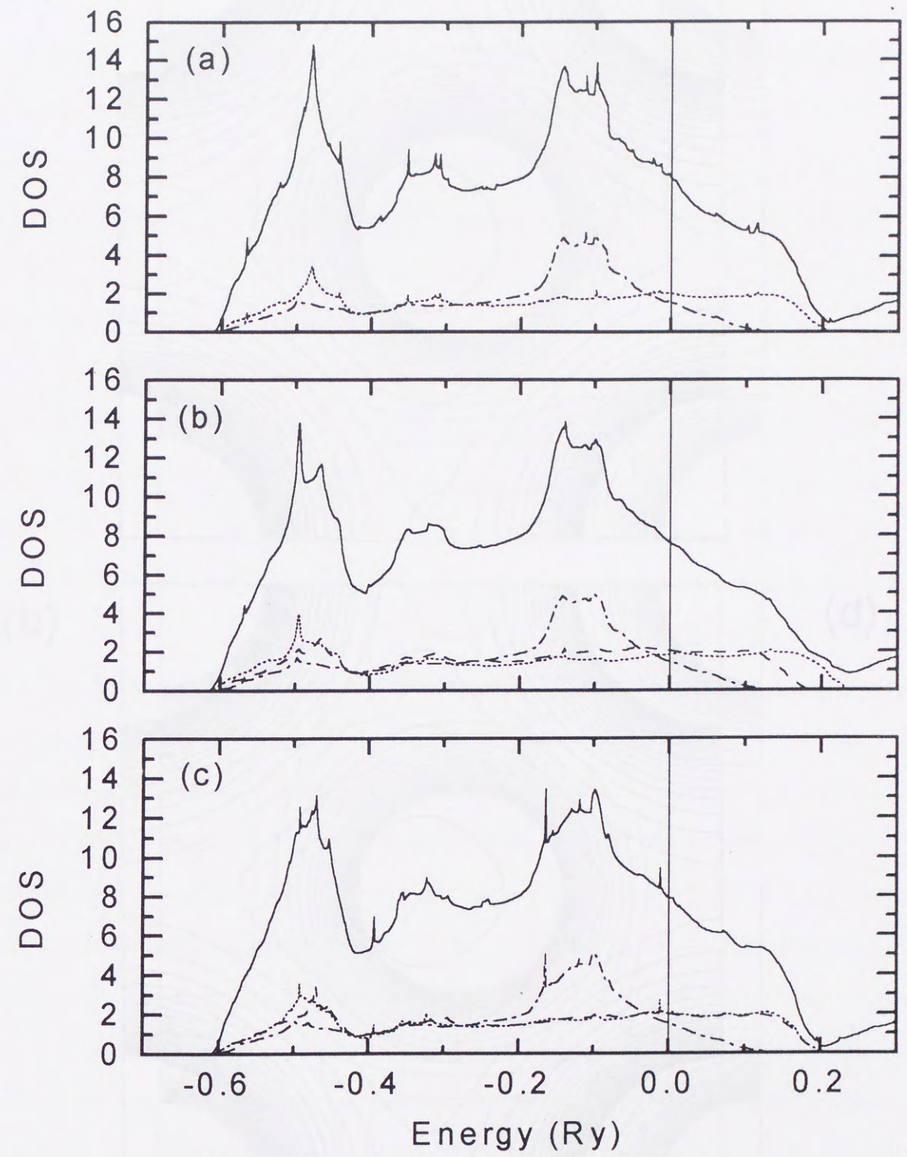

Figure 12: Density of states of (a) BCT, (b) BCO, and (c) FCO. The solid, dash-dotted, broken, and dotted lines denote the total, the partial of $5p_z$, $5p_y$, and $5p_x$ DOS respectively.

(a)

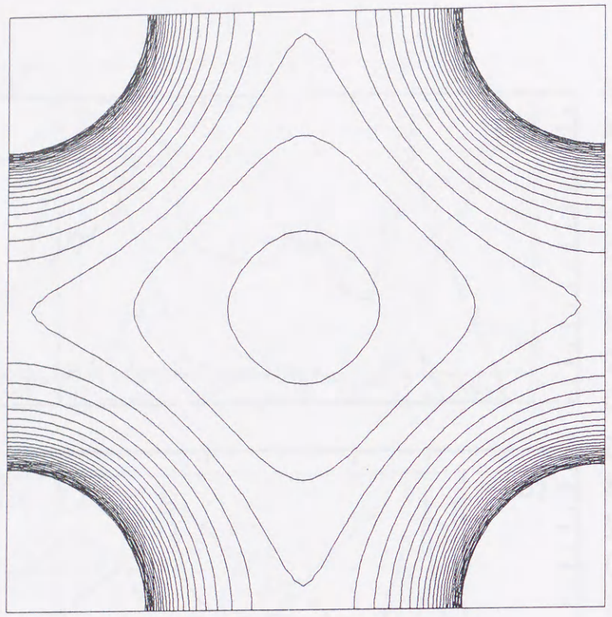

(b)

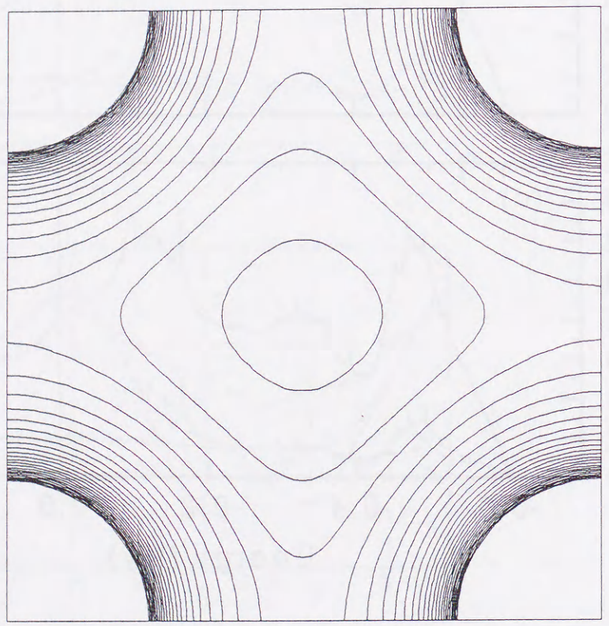

Figure 13: Electronic density maps on xy-plane of (a) BCT and (b) BCO. The contour values are given in 0.1 e/Å^3 and are drawn from 0.1 to 2.5 e/Å^3.

(a)

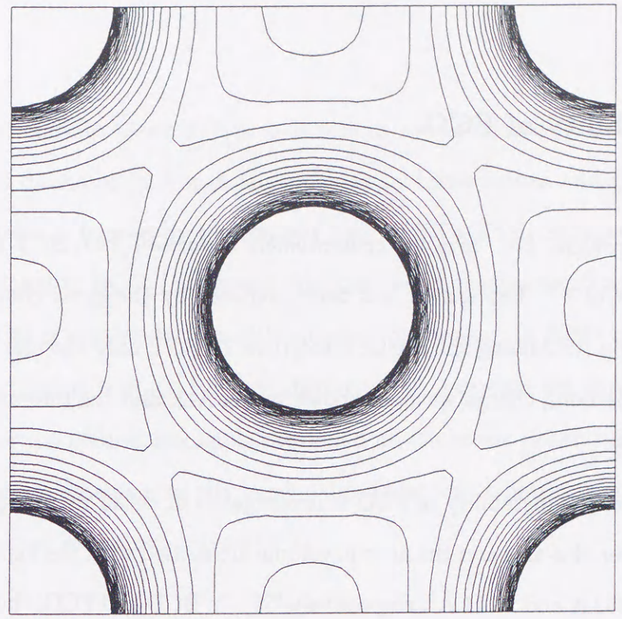

(b)

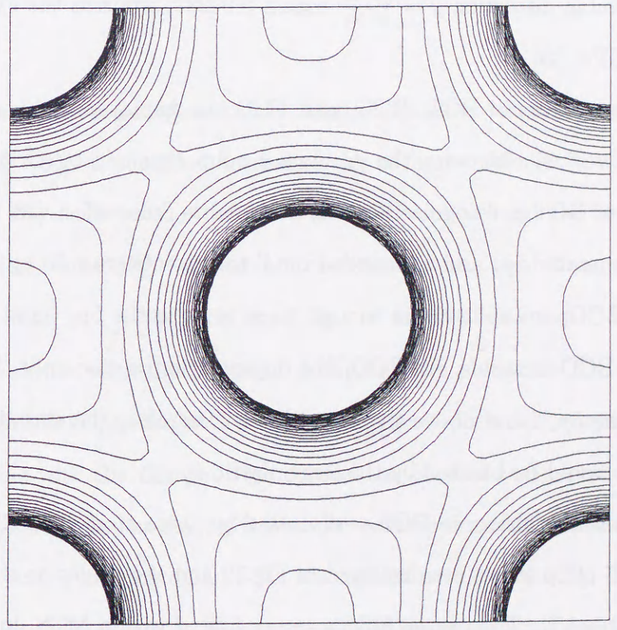

Figure 14: Electronic density maps on xy-plane of (a) BCT and (b) FCO. The contour values are given in 0.1 e/Å^3 and are drawn from 0.1 to 2.5 e/Å^3.

3.2 Instability of FCO

There is a problem, i.e. "*why the orthorhombic distortion from BCT is realized only in BCO not in FCO ?*" The answer has been prepared by the bond charge model [37] as discussed in App.A: Among the elastic distortions of BCT only the one of B_{1g} symmetry couples with the bond charge wave, as shown in Fig.A-2, and the interatomic repulsion is mediated.

In this section the instability of FCO is investigated in detail by using FP-LMTO. The lattice parameter of z-axis and the atomic volume are settled with the experimental ones at 30 GPa, i.e. 5.252 Å and 23.11 Å^3, respectively [36]. In BCO and FCO, the order parameter of the orthorhombic distortion $g = \frac{|a_i - b_i|}{\sqrt{a_i b_i}}$ equals 0.04281, which is the experimental value of BCO at 30 GPa [36].

The dispersion curves of BCT, BCO, and FCO are displayed in Fig.11. In BCT and BCO, they are very similar with the previous results obtained by Orita *et al.* [28, 33]. The instability of BCT is recognized by the band Jahn-Teller effect [28, 33]. As shown in Fig.11, the degenerated $5p_x$ and $5p_y$ bands from Z to Γ points are split by the orthorhombic distortion. In BCO, the splitting is enough large to raise the $5p_x$ band above the Fermi level, then the BCO is stable. In FCO, the degeneration is also split, however it is too small to raise the $5p_x$ band above the Fermi level. Therefore the stability caused by the FCO distortion would be blocked by the large elastic energy.

The situation is also shown in DOS as discussed by Orita *et al.* [28, 32]. The total DOS and partial DOS of $5p$ states are displayed in Fig.12 and the values at the Fermi level are tabulated in Table VII. The partial DOS's are evaluated within MTS. In BCT, the Fermi level is on the shoulder of DOS. In BCO, the DOS value at the Fermi level is lowered by the orthorhombic distortion. In FCO, the separation between p_x and p_y states is very little and the DOS value at the Fermi level is almost unchanged.

The electronic density maps are shown in Figs.13 and 14. The densities at the center of interatomic bondings along x- and y-directions are tabulated in Table VIII. The bond charge model discussed in App.A is supported by these figures and the table. The 2-dimensional network is formed by the contour lines of 0.3 e/Å^3 in BCT and FCO, however it is 1-dimensional in BCO. It suggests that the "bond charge wave" which has same symmetry with BCO is created by the orthorhombic distortion. In BCO the large splitting of degenerated bands is caused by the distortion of electronic density. In FCO the orthorhombic distortion creates negligible distortion on electronic density as displayed in Fig.14, therefore the mechanism of the band Jahn-Teller effect hardly works. Thus the orthorhombic structure is realized only in BCO.

3.3 Phenomenological model

In this section the phenomenological model, firstly applied to the dimerization of iodine by Takemura *et al.* [36], is modified to realize the orthorhombic molecular phase. As displayed in Fig.15 the undistorted structure is assumed as FCO and the atomic displacements of dimerization, to be $D_{2h}^{18} - Cmca$, are decomposed into two phonons. The first is transverse phonon at $\mathbf{k_1} = (\frac{\pi}{a_f}, 0, 0)$, on the Σ line of the Brillouin zone. The symmetry of the Σ line is isomorphic with the C_{2v} point group and the phonon is B_1 representation. The second is longitudinal phonon at $\mathbf{k_2} = 2\mathbf{k_1}$, on the X-point. The symmetry of the X-point is isomorphic with the D_{2h} point group and the phonon is B_{1u} representation.

As shown in Fig.4 the relation among the lattice parameters of molecular phase is $a > c/2 > b$, hence the lattice parameters of FCO are defined as $c_f > a_f > b_f$. The molecular axis is parallel to the bc-plane, then the atomic coordinates y and z are determined as follows:

$$y = \frac{1}{2}\frac{r \cdot \sin(\theta)}{b}, \tag{33}$$

$$z = \frac{1}{2}\frac{r \cdot \cos(\theta)}{c}, \tag{34}$$

where r is the bond length of an I_2 molecule and θ is the angle with respect to the c-axis. If $(y, z) = (\frac{1}{4}, \frac{1}{8})$ then the structure is FCO, thus the amplitudes of the two phonons η_1 and η_2 are determined as $\frac{1}{4} - y$ and $\frac{1}{8} - z$, respectively.

X-ray experimental results [18] of the amplitudes are shown in Fig.16. The η_2 value changes negligibly and is about 0. Then the atomic layers normal to the c-axis are equally spaced. Therefore the "molecular dissociation" along c-axis has been finished even at ambient pressure. The gradual decrease in η_1 represents the gradual molecular dissociation along the b-axis. This fact indicates effectiveness of the phenomenological model discussed in the following.

The change in the crystalline density function associated with the two phonons is described by three order parameters Q_1, Q_1^*, and Q_2:

$$\Delta\rho(\mathbf{r}) = Q_1 e^{i\mathbf{k_1 r}} + Q_1^* e^{-i\mathbf{k_1 r}} + Q_2(e^{i\mathbf{k_2 r}} + e^{-i\mathbf{k_2 r}}). \tag{35}$$

Because the X-point is at the boundary of Brillouin zone, the longitudinal phonon at $-\mathbf{k_2}$ could not be independent with the $\mathbf{k_2}$ phonon. The origin is set at the any atom of FCO, then $Q_2 = Q_2^* = \eta_2$. With the translational invariance a Landau free-energy expansion are written as

$$\begin{aligned} F &= c_0 + \frac{1}{2}c_1 Q_1^* Q_1 + \frac{1}{2}c_2\eta_2^2 + \frac{1}{2}c_3(Q_1^2 + Q_1^{*\,2})\eta_2 \\ &+ \frac{1}{4}c_4(Q_1 Q_1^*)^2 + \frac{1}{8}c_5(Q_1^4 + Q_1^{*\,4}) + \frac{1}{6}c_6(Q_1 Q_1^*)^3 + \cdots, \end{aligned} \tag{36}$$

or on writing $Q_1 = \eta_1 e^{i\phi}$,

$$F = c_0 + \frac{1}{2}c_1\eta_1^2 + \frac{1}{2}c_2\eta_2^2 + c_3\eta_1^2\eta_2\cos 2\phi + \frac{1}{4}(c_4 + c_5\cos 4\phi)\eta_1^4 + \frac{1}{6}c_6\eta_1^6 + \cdots. \tag{37}$$

Minimizing with respect to η_2 then

$$\eta_2 = -\frac{c_3}{c_2}\eta_1^2\cos 2\phi. \tag{38}$$

Minimizing with respect to ϕ within the condition (38) then

$$\frac{\partial F}{\partial \phi} = \eta_1^4\left(\frac{2c_3^2}{c_2} - c_5\right)\sin 4\phi = 0. \tag{39}$$

Here the accidental vanishing of the terms among the parentheses of Eq.(39) should be avoided. The solution is $\phi = \frac{n\pi}{4}$. If $\phi = \frac{(2n+1)\pi}{4}$ then the amplitudes of the transverse phonons are identical at all the atomic sites and the amplitudes of the longitudinal phonons are vanished: The distorted structure has the space group symmetry D_{2h}^{18}–$Cmca$. If $\phi = \frac{n\pi}{2}$ then the amplitudes of the transverse phonons are vanished at the atomic sites alternately: The distorted structure could not be identified after some of symmetry operations of D_{2h}^{18}–$Cmca$. Therefore the solutions $\phi = \frac{(2n+1)\pi}{4}$ are the demanded and the condition $c_5 > \frac{2c_3^2}{c_2}$ should be satisfied to be minima. Then the condition $c_5 \neq 0$ to single out $\mathbf{k} = \mathbf{k_1}$ [36] is also satisfied. After all the constrained free energy is

$$\tilde{F} = c_0 + \frac{1}{2}c_1\eta_1^2 + \frac{1}{4}\tilde{c_4}\eta_1^4 + \frac{1}{6}c_6\eta_1^6 \tag{40}$$

where $\tilde{c_4} = c_4 - c_5$.

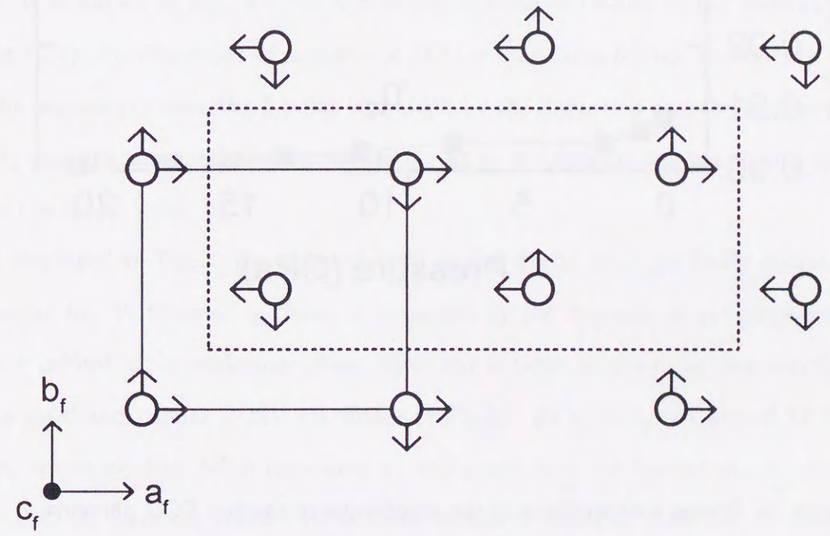

Figure 15: Dimerization from FCO. Solid and broken lines represent the unit cell of the monatomic FCO and the molecular phase respectively.

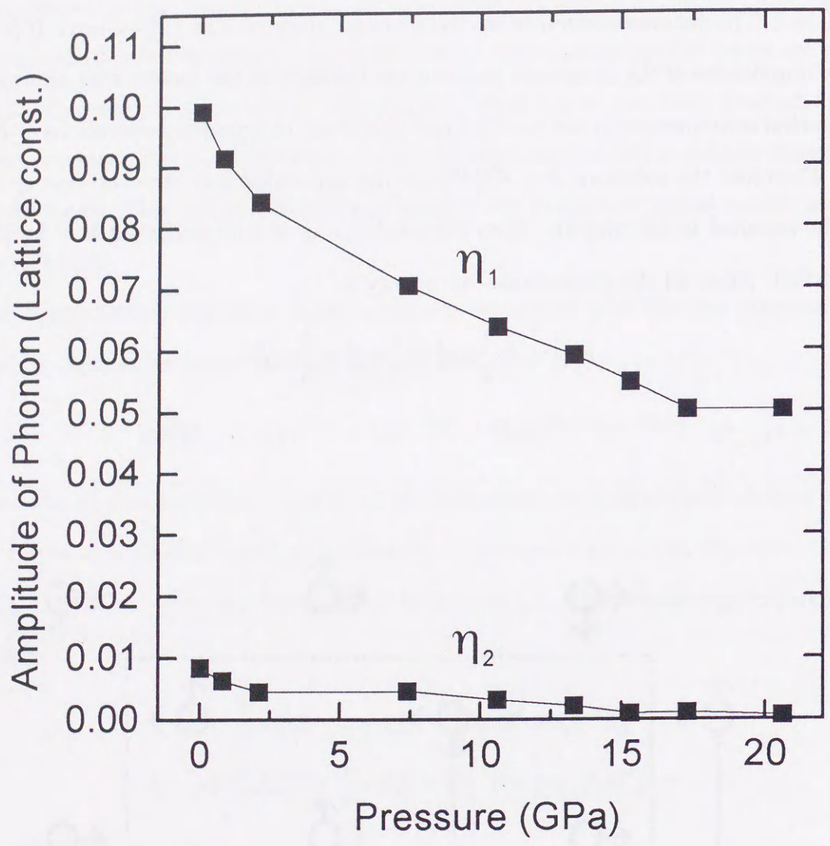

Figure 16: Pressure dependence of the amplitudes of the two FCO phonons.

3.4 Dimerization from FCO

In this section the dimerization from FCO is numerically investigated by using FP-LMTO. The orthorhombic lattice parameters are taken from the experimental results [18] at 15.3 GPa (Fig.4). The total energies versus the amplitude of the transverse phonon, η_1, is displayed in Fig.17, in which η_1 is measured in the unit of the lattice parameter b of the molecular phase. The least square fitting result for Eq.(40) during the η_1 value from 0 to 0.02 is $c_1 = -1.644 \cdot 10^3[\mathrm{mRy}], \tilde{c_4} = -1.291 \cdot 10^{-2}[\mathrm{mRy}]$, and $c_6 = 6.336 \cdot 10^9[\mathrm{mRy}]$. The FCO structure is unstable with respect to the transverse phonon with the infinitesimal amplitude.

The Madelung energy versus η_1 is displayed in Fig.18. The energy is increased monotonously, and therefore the molecular phase is stabilized by the electronic properties.

By the distortion of the transverse phonon, degenerates of the electronic dispersion curves are split as shown in Fig.19. The Λ-direction is along the c-axis of the molecular phase. In Fig.19(a), the dispersion of monatomic FCO is four-times folded. In Fig.19(b),(c), and (d) the degeneracy near the Z-point is avoided by the distortion and the repulsion among the Λ_4 bands is increased with increasing η_1. At $\eta_1 = 0.035$ the bands are split above and below the Fermi level.

As displayed in Fig.20 the value of DOS at the Fermi level gradually decreases with increasing η_1. With small η_1 value, it is caused by the decrease of p_z component which forms σ orbital in the molecular phase. Here xyz is taken as the molecular coordinate.

The total and partial DOS's are shown in Fig.21. At $\eta_1 = 0$, the partial DOS's of p_x and p_z are nearly flat. With increasing η_1, two peaks of p_z are formed above 0.07 Ry and below 0.45 Ry from the Fermi level as the σ orbital of diatomic molecule. Broad peaks of p_x as π orbital at about -0.1 and -0.25 Ry are formed with increasing η_1. The splitting between p_x and p_z is enhanced by the formation of the diatomic molecule: Decrease of DOS at Fermi level is caused by the dimerization and the molecular phase is stabilized.

The total energy with respect to η_1 around the bottom is regarded as representing an one-dimensional oscillator. The energy at the bottom and the frequency of the oscillator are obtained by four point values fitted to a cubic form. The pressure dependence of the energy difference between FCO's and the value at the bottom is displayed in Fig.22(a). The frequency versus pressure is shown in Fig.22(b). The pressure dependence of η_1 at the bottom and the molecular length are shown in Figs.23(a) and (b) respectively.

The molecular length is negligibly changed by compression. Such result is also obtained by X-ray experiment [18] as shown in Fig.4 (b). The bottom is defined by the balance between the repulsion among two nucleus and the attraction caused by the electronic bindings. The repulsion is mostly mediated by the deep lying σ-bondings among the valence $5p$ electrons. As displayed in Fig.21 the sharp peak of $5p_z$, which is along the molecular axis, is found around -0.45 Ry from the Fermi level. Therefore the molecular length is negligibly affected by the compression. It is also shown by the small change of electronic density at the center of diatomic molecule, b_{21} observed by X-ray [17]. The negligible changes in the molecular length and b_{21} are also obtained by frozen-phonon calculations as discussed in Chap.4 and are displayed in Figs.28 and 33 respectively.

When the orthorhombic parameters and the molecular length are fixed, the value of η_1 is uniquely obtained: The value is decreased with increasing pressure as displayed in Fig.23(a). It is also observed by X-ray as shown in Fig.16. As a result the third neighbor distance, i.e. between 2 and 1', are approaching. In Fig.24, the electronic density coming from the Z_1 bands shown in Fig.19(d) are displayed. In Fig.24(a), the "high energy" σ-antibonding state of the molecule could be regarded as a π-like state of the atomic pair of third neighbors. And in Fig.24(b), the "low energy" π state could be regarded as a σ^*-like state of the atomic pair of third neighbors. Therefore under high pressure, the distinction between σ^* (p_z) and $\pi^{(*)}$ (p_x) becomes ambiguous. As discussed above, the molecular phase is stabilized by the splitting between p_x and p_z as displayed in Fig.21, therefore the energy difference between FCO and the molecular phase is decreased with increasing pressure as

shown in Fig.23(b). When the bottom is pushed up by the compression, the softening is occurred in the one-dimensional oscillator as shown in Fig.22(b).

Here the decision of the structure of molecular phase could be divided in two factors within the bc-plane:

(I) As discussed in Sec.3.2, the energy of the monatomic FCO, as the undistorted structure of the molecular phase, is increased with increasing an orthorhombic order parameter $g = \frac{|a_f - b_f|}{\sqrt{a_f b_f}}$, where $a_f = c/2$ and $b_f = b$.

(II) As discussed in Sec.3.4, the diatomic binding with a fixed molecular length is stabilized with increasing g, because the third neighbor distance is increased with increasing g.

The realized structure is coming from the energetic balance between (I) and (II) above. From the data of Fig.4, the experimental order parameter g is obtained as shown in Fig.25. The value of g is increased with increasing pressure, to mediate the effect of decreased third neighbor distance. It seems that the structure of the molecular phase at each volume is determined by the molecular length as discussed by Fujihisa *et al.* [65].

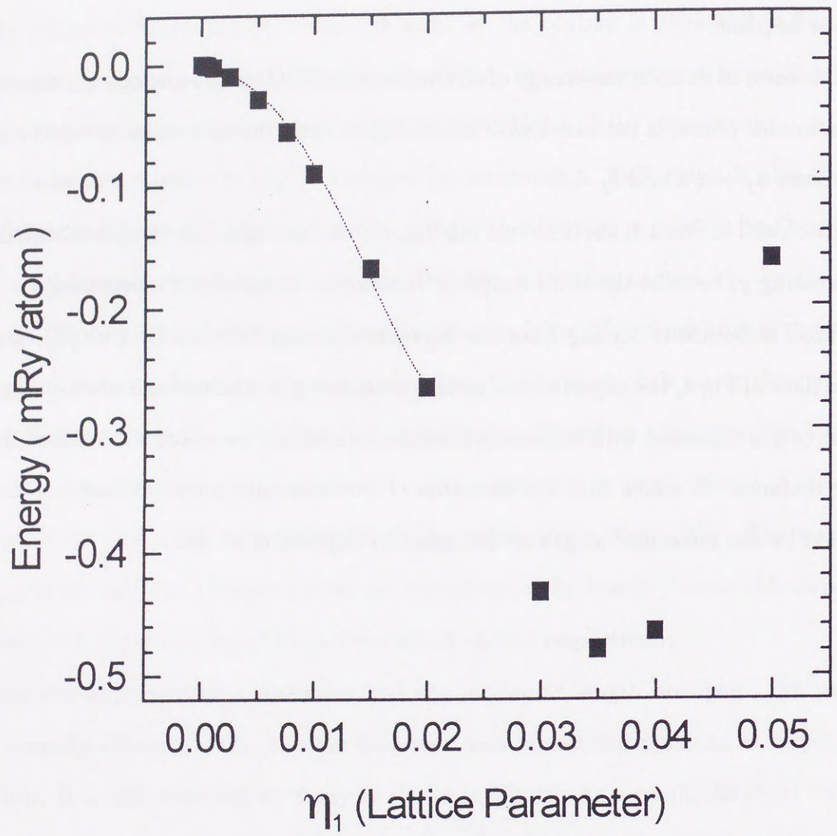

Figure 17: Total energy versus the amplitude of the transverse FCO phonon η_1. The dotted line denotes the least square fitting result for Eq.(40) during the η_1 value from 0 to 0.02.

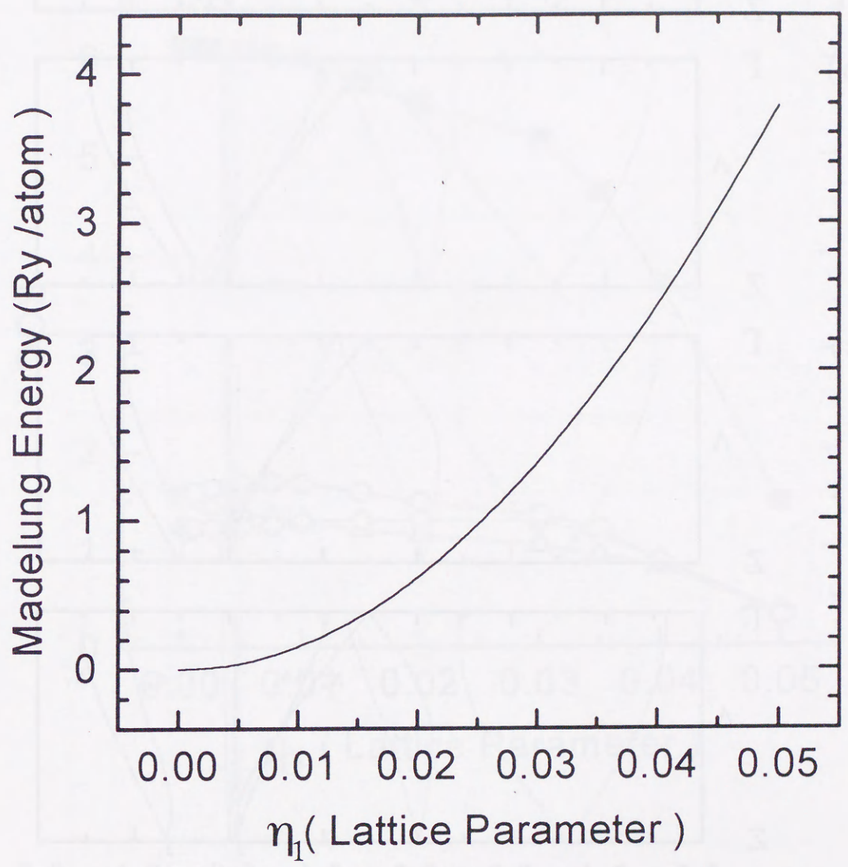

Figure 18: Madelung energy versus the amplitude of the transverse FCO phonon η_1.

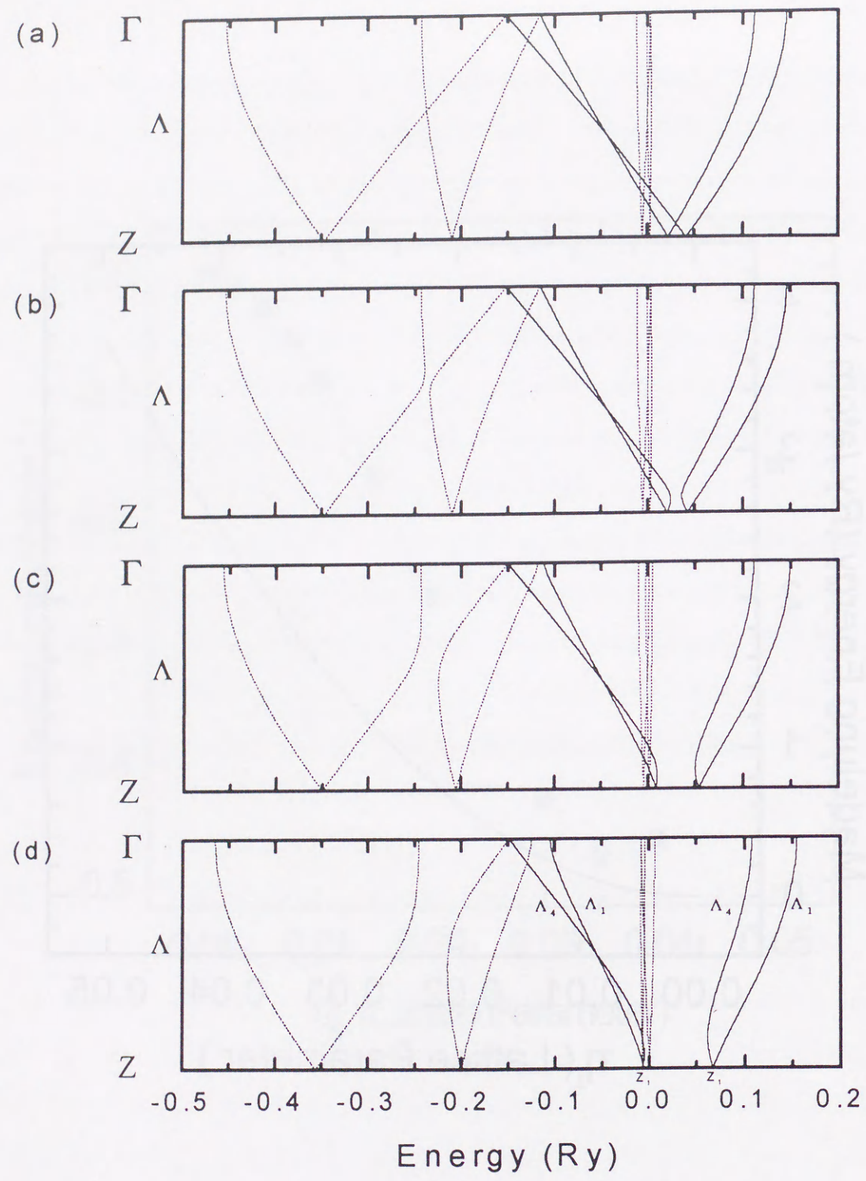

Figure 19: Dispersion curves with η_1 equals (a) 0, (b) 0.005, (c) 0.02, and (d) 0.035. Solid lines denote Λ_1 and Λ_4 bands around the Fermi level. The other bands are represented by dotted lines.

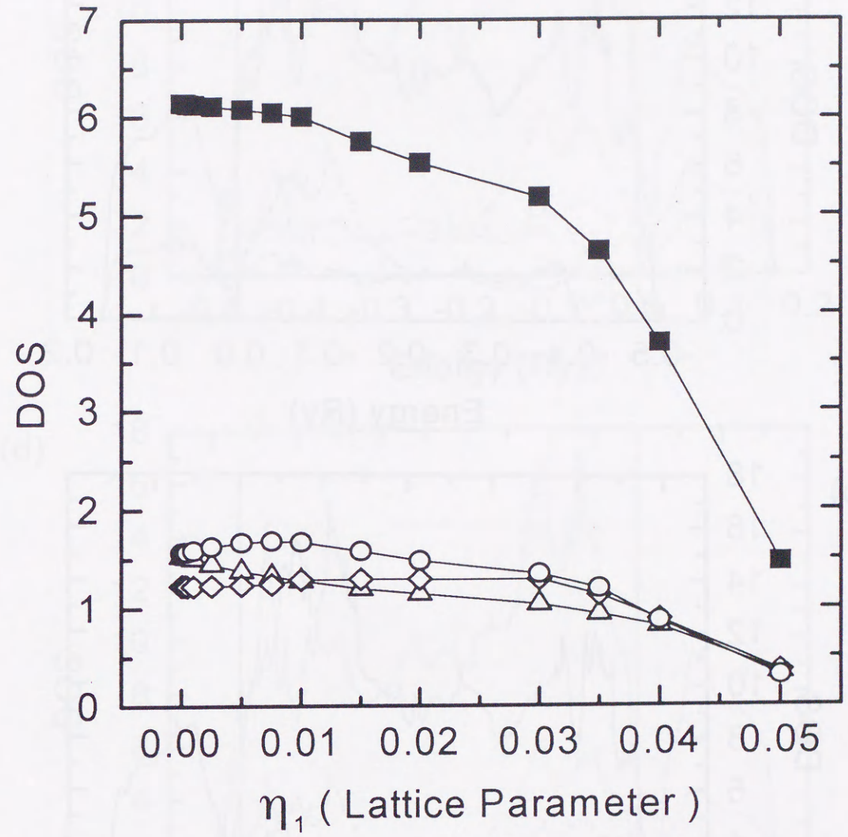

Figure 20: The value of DOS at the Fermi level versus the amplitude of the transverse FCO phonon η_1. Filled square denotes the total DOS. Open circle, diamond, and triangle represent the partial DOS of p_x, p_y, and p_z respectively, where z is set along the molecular axis, y is normal to the bc-plane, and x is on the bc-plane.

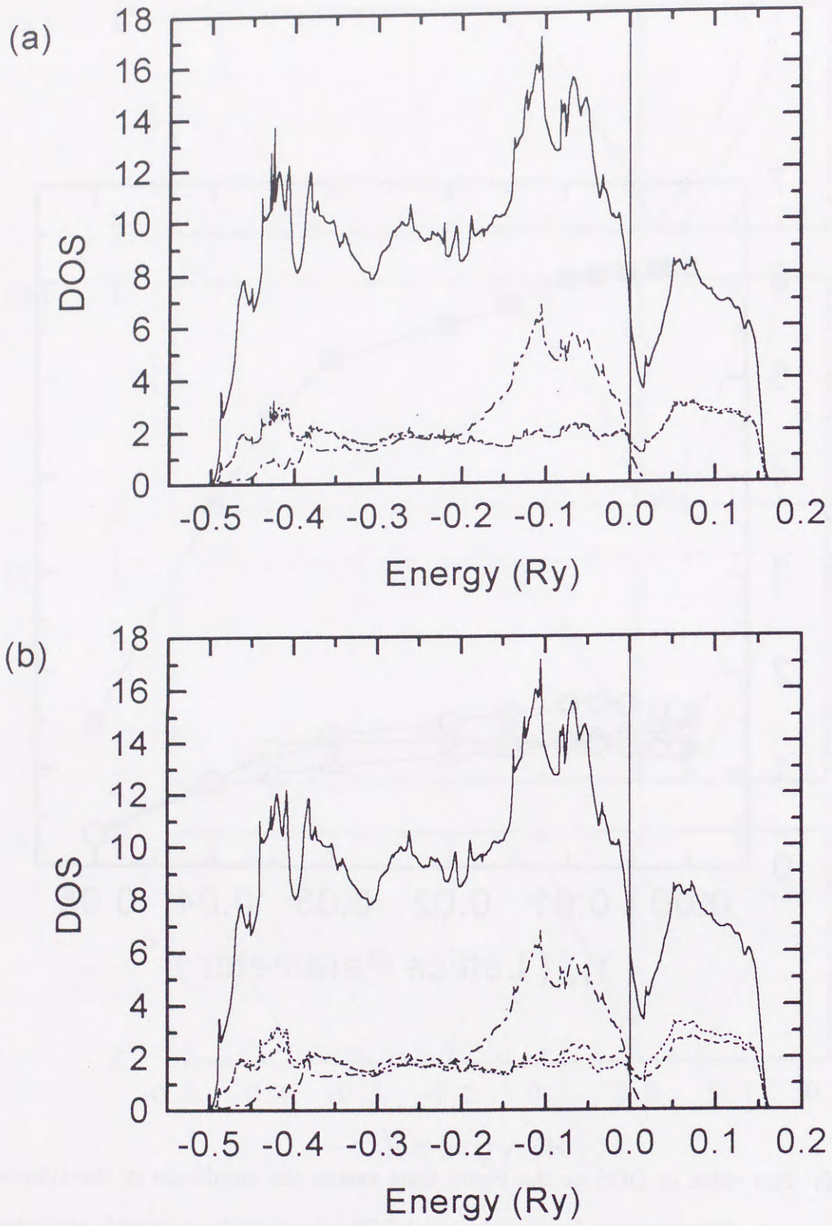

Figure 21: Figure caption is written in the following page.

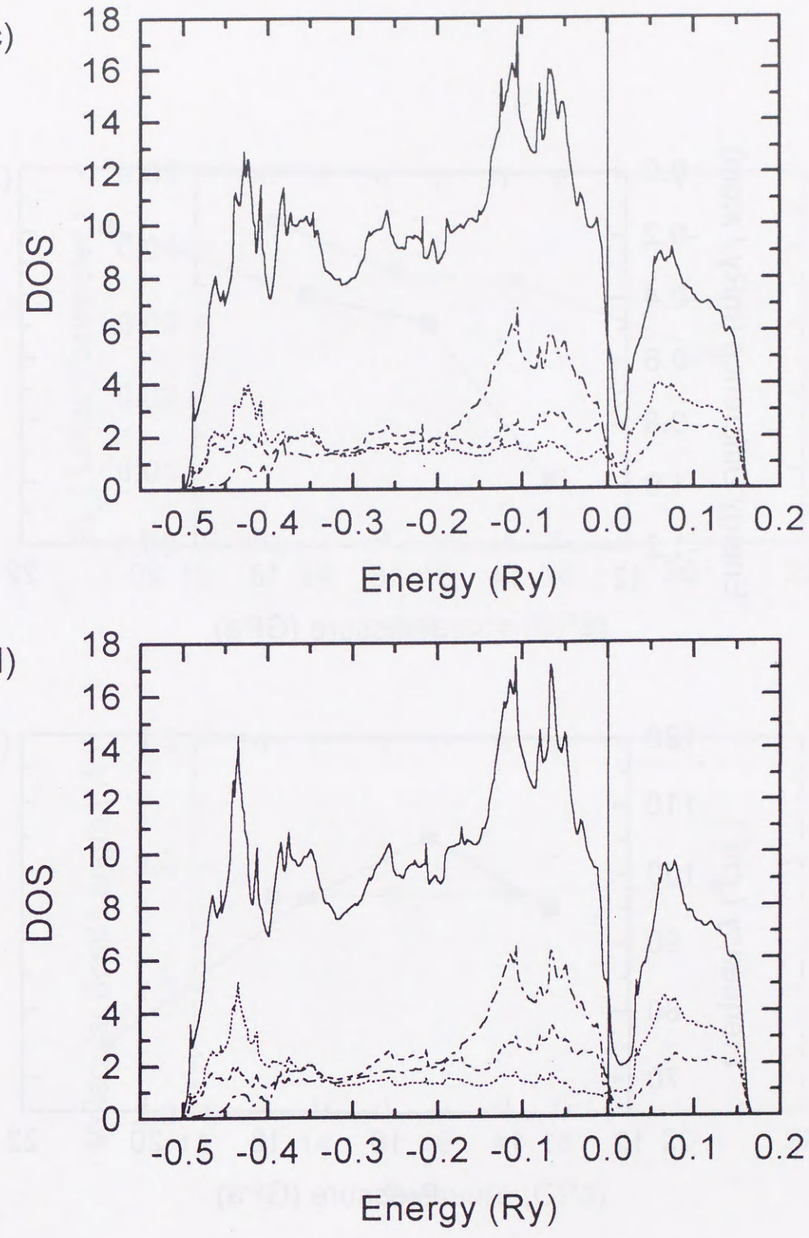

Figure 21: Total and partial DOS's with the amplitude of the transverse FCO phonon η_1 equals (a) 0, (b) 0.005, (c) 0.02, and (d) 0.035. Solid line denotes the total DOS, and broken, dash-dotted, and dotted lines represent the partial DOS of p_x, p_y, and p_z respectively,

(a)

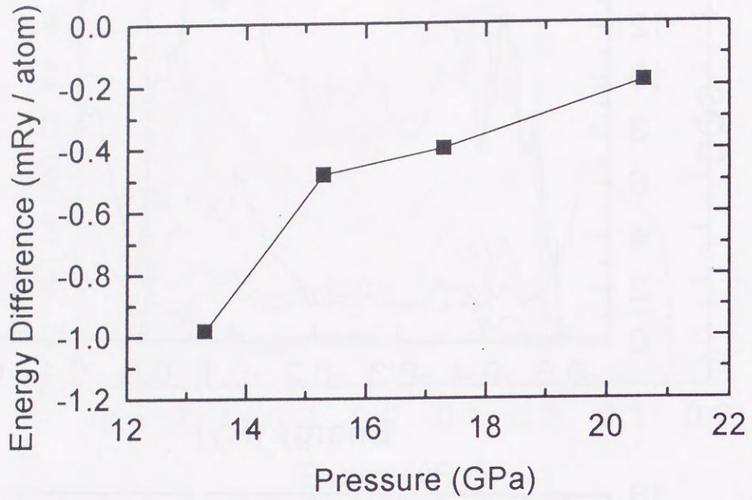

(b)

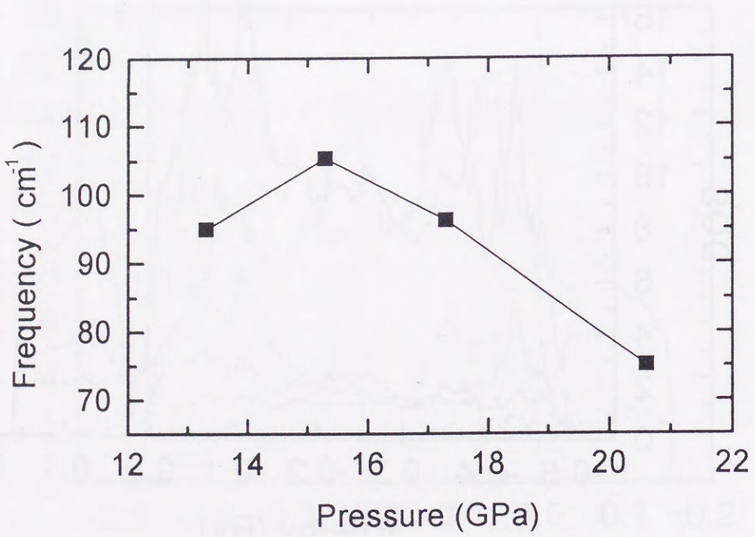

Figure 22: Pressure dependence of (a) energy difference between FCO and the bottom with respect to η_1 and (b) frequency of the one-dimensional oscillator with respect to η_1.

(a)

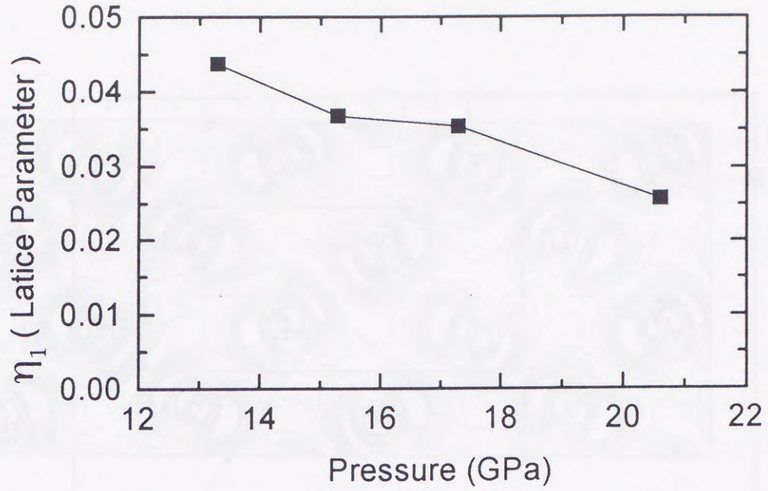

(b)

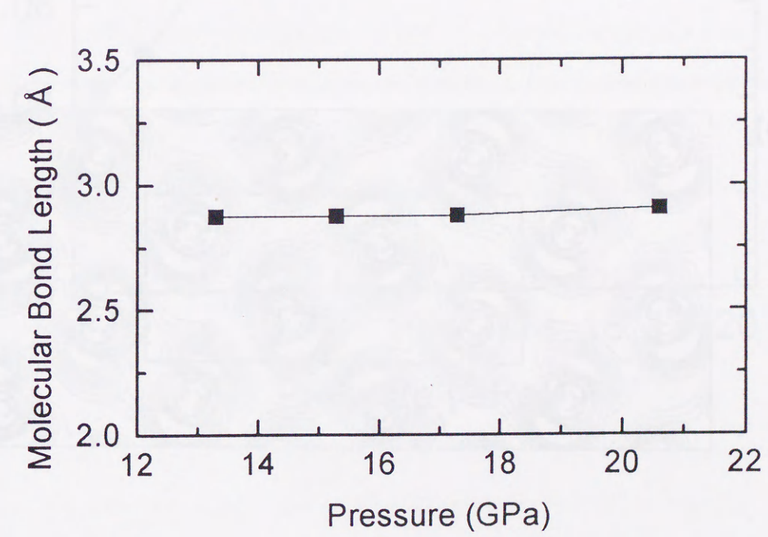

Figure 23: Pressure dependence of (a) the bottom position with respect to η_1 and (b) molecular length at the bottom.

(a)

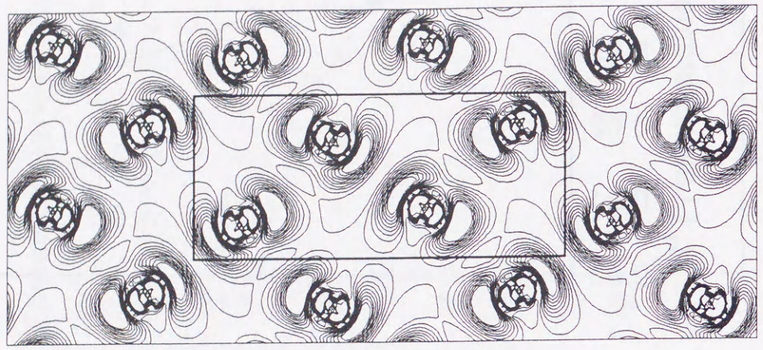

(b)

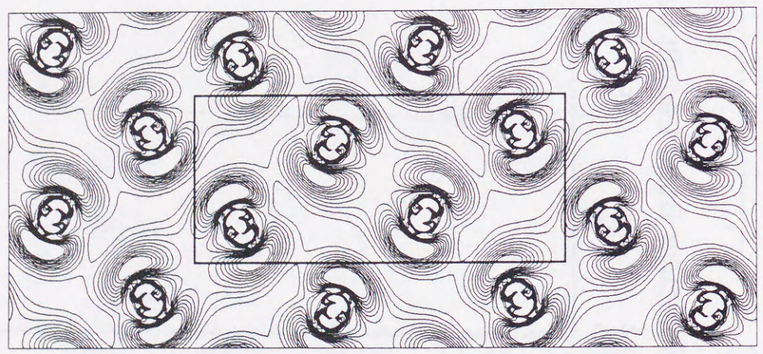

Figure 24: Electronic densities coming from the Z_1 bands displayed in Fig.19(d). The unoccupied and occupied around the Fermi level are displayed in (a) and (b), respectively. The contour values are given in 0.005 e/Å^3 and are drawn from 0.005 to 0.05 e/Å^3.

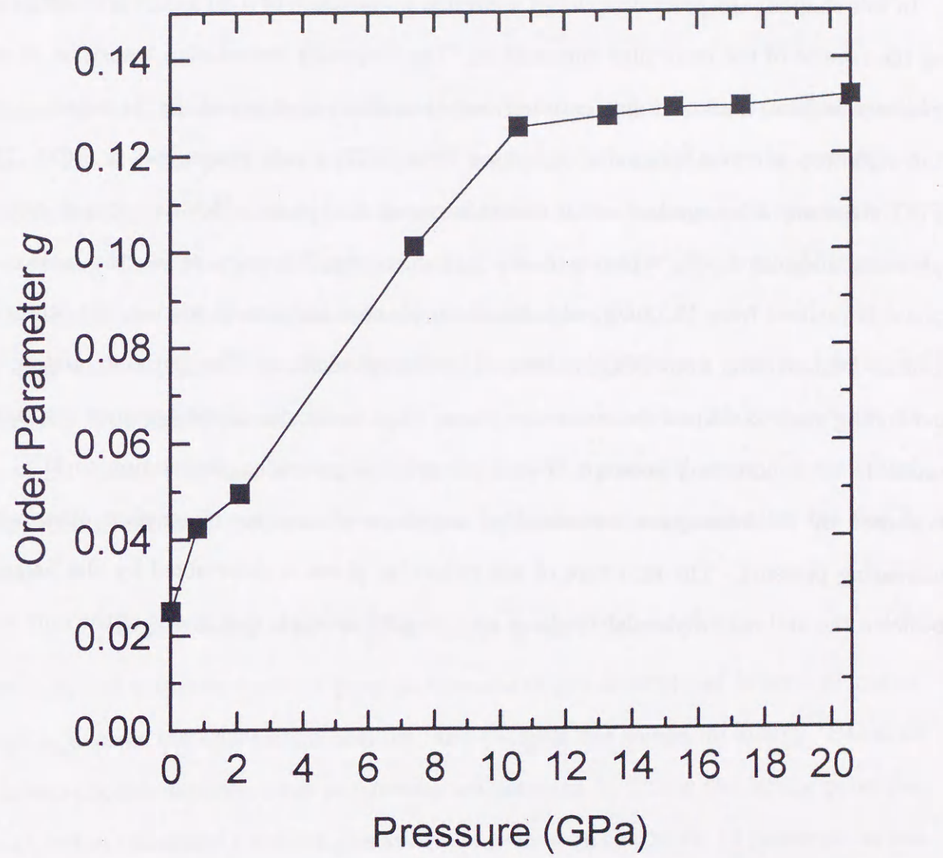

Figure 25: Pressure dependence of FCO orthorhombic order parameter calculated from the X-ray experimental result displayed in Fig.4(a).

3.5 Conclusion of Chap.3

In this chapter, the pressure-induced molecular dissociation of solid iodine is investigated as the reverse of the molecular dimerization. The molecular dissociation transition to the monatomic BCO is allowed only as a first-order transition as observed. In the experiments, the structure with orthorhombic distortion from BCT is only discovered in BCO. The FCO structure is recognized as an unstable monatomic phase. However, based on the phenomenological model, which is firstly introduced by Takemura *et al.*, the molecular phase is realized from FCO with the distortion of the transverse phonon at the center of Σ line. Dimerization from FCO is obtained by the calculations: The diatomic binding by σ-bonding state stabilizes the molecular phase. The molecular phase becomes gradually unstable with increasing pressure, that is the gradual molecular dissociation to FCO. It is caused by the interaction between third neighbors which come closer each other with increasing pressure. The structure of the molecular phase is determined by the balance between the diatomic molecular bindings and the orthorhombic distortions of the unit cell.

4 Pressure Effects on Vibron and Libron

4.1 Method

In this section, frozen-phonon calculations for A_g lattice vibrations of molecular solid iodine at $\mathbf{k} = 0$ under pressure are presented. The A_g mode is the identity representation, therefore the original structure and the distorted one in A_g modes have same symmetry, i.e. $D_{2h}^{18} - Cmca$. The structure, as displayed in Fig.1, is characterized by three orthorhombic lattice parameters, a, b, and c, and two atomic coordinates, y and z.

In this work, optimization with respect to the lattice parameters, a, b, and c, is not performed. The lattice parameters at each pressure are taken from the recent X-ray experimental results [18], and are displayed in Fig. 4. The potential energy of the lattice is expanded in terms of the atomic coordinates in the basis corresponding to the two A_g modes,

$$U(y,z) = \alpha(y-y_0)^2 + \frac{1}{2}\beta(y-y_0)(z-z_0) + \gamma(z-z_0)^2 + U_0, \tag{41}$$

where α, β, and γ are the three independent elements of two dimensional dynamical matrix, y_0 and z_0 express the equilibrium position, and U_0 gives the minimum energy. Based on the frozen-phonon method, these parameters are obtained by fitting the lattice potential, $U(y,z)$, to the calculated total energies at several points. In this work, 12 points of various atomic coordinates are used. To avoid the anharmonic effects, the atomic coordinates are selected within 0.1 a_0 from the equilibrium position. Phonon frequencies and normal modes are obtained by diagonalization of the dynamical matrix.

4.2 Results

Pressure dependence of the calculated frequencies of A_g modes are displayed in Fig.26. The low frequency mode (LFM) shows maximum around 10 GPa. The high frequency mode

(HFM) shows minimum around 1 GPa and gradually increases with increasing pressure.

Pressure dependence of the atomic coordinates with the equilibrium structure, i.e. y_0 and z_0, are displayed in Fig.27. The y_0 value increases with increasing pressure, however the z_0 value negligibly changes and nearly equals one eighth.

Pressure dependence of the molecular bond length with the equilibrium structure are displayed in Fig.28. The values are negligibly changed by the compression.

The total energy of the molecular phase with the equilibrium structure versus atomic volume is displayed in Fig.29. It is compared with the energy of FCO calculated with the orthorhombic lattice parameters taken from the experimental results [18] (Fig.4) and four atoms in the primitive cell. The best fitted Murnaghan's EOS parameters are $B_0 = 19.22$ GPa, $B_0' = 4.644$, and $V_0 = 243.80$ a.u. for the molecular phase and $B_0 = 27.97$ GPa, $B_0' = 4.411$, and $V_0 = 228.89$ a.u. for FCO. The atomic volume of the molecular phase at zero pressure is 84.6 percent of the experimental one. The transition pressure obtained by the extrapolation is 13 GPa with a volume change from 178.83 a.u. in the molecular phase to 177.04 a.u. in FCO: The pressure is an upper limit of the molecular dissociation within the present work. In the experiment, the volume changes from 172 a.u. for the molecular phase to 165 a.u. for BCO [12].

The total and partial DOS at the Fermi level of the equilibrium structure versus the experimental pressure are displayed in Fig.30. The band overlap is occurred around 10 GPa.

The direction of eigenvector of HFM with respect to the c-axis is compared with the molecular axis at the equilibrium position in Fig.31. At ambient pressure the two directions nearly equal, therefore HFM can be called as stretching mode (vibron) and LFM as librational (libron). However the difference between the two directions increases with increasing pressure. Thus the two A_g modes could not be separated such as in Fig.2 in compressed state. Above the band overlap pressure, i.e. around 10 GPa, HFM directs along the c-axis and LFM along b-axis as displayed in Fig.32.

Pressure dependence of the density at the center of interatomic bonding for the equilibrium structure is shown in Fig.33. The intramolecular bond charge b_{21} slightly increases up to about 10 GPa, and above the band overlap pressure slightly decreases with increasing pressure. The intermolecular bond charges $b_{21'}$ and b_{27} increase with increasing pressure.

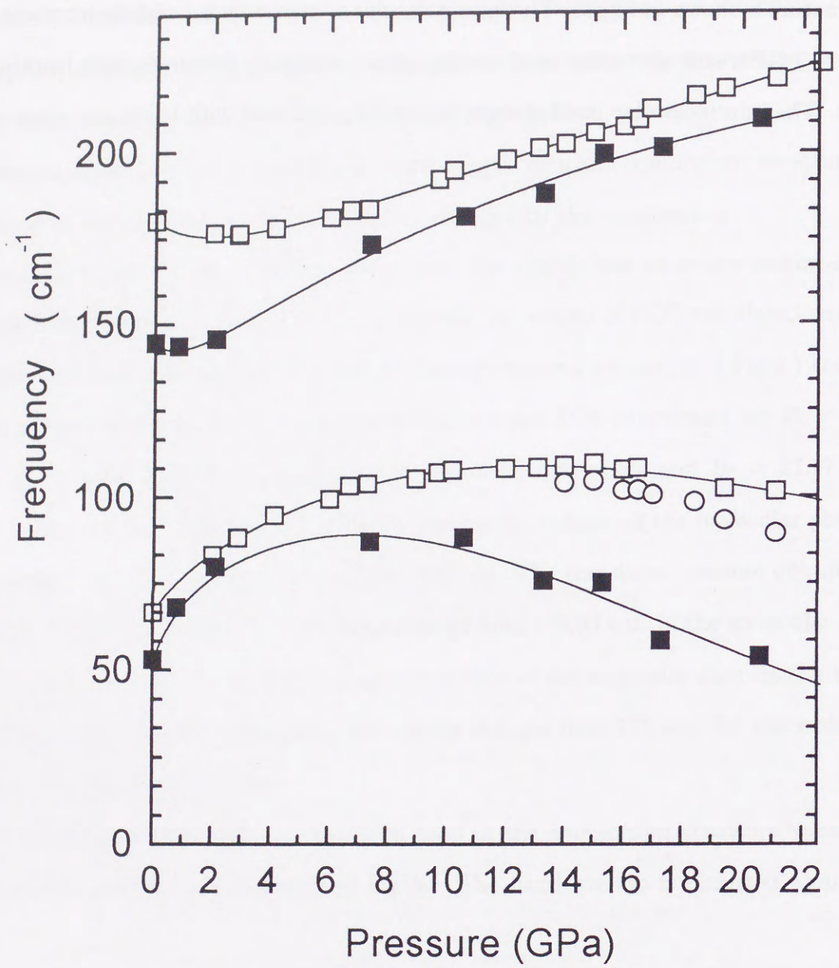

Figure 26: Pressure dependence of Raman active A_g modes of molecular solid iodine. Open and filled squares denote experimental and calculated results, respectively. Open circles represent the X band reported by Olijnyk *et al.* [25]. Solid lines are guide to eye.

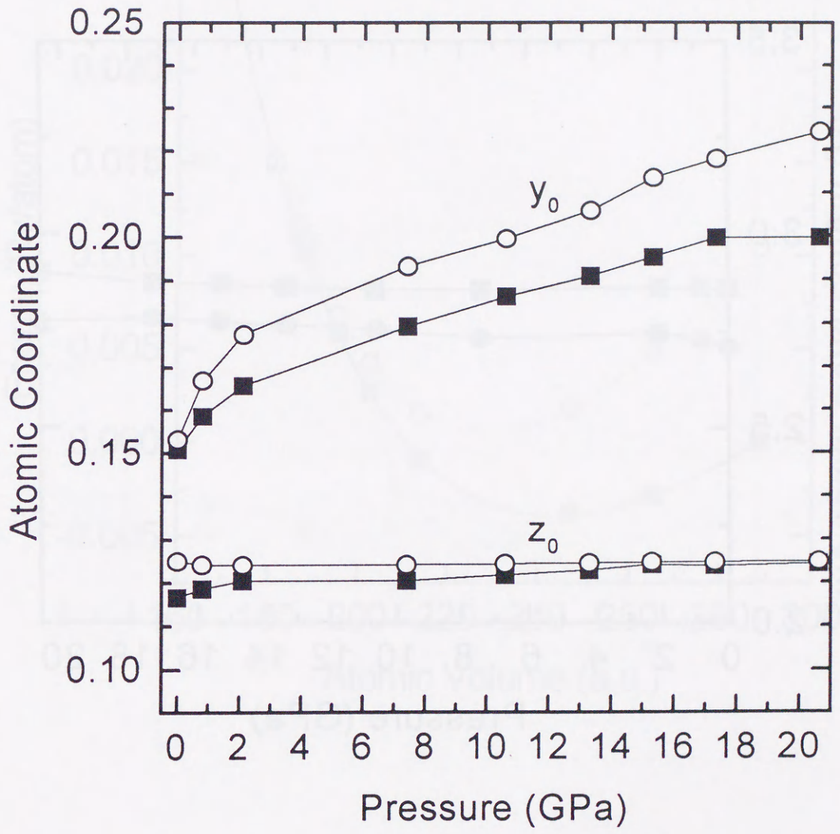

Figure 27: Pressure dependence of the atomic coordinates of the equilibrium position. Open circles are calculated results. Filled squares are X-ray experimental results by Fujihisa [18], which are shown in Fig.4.

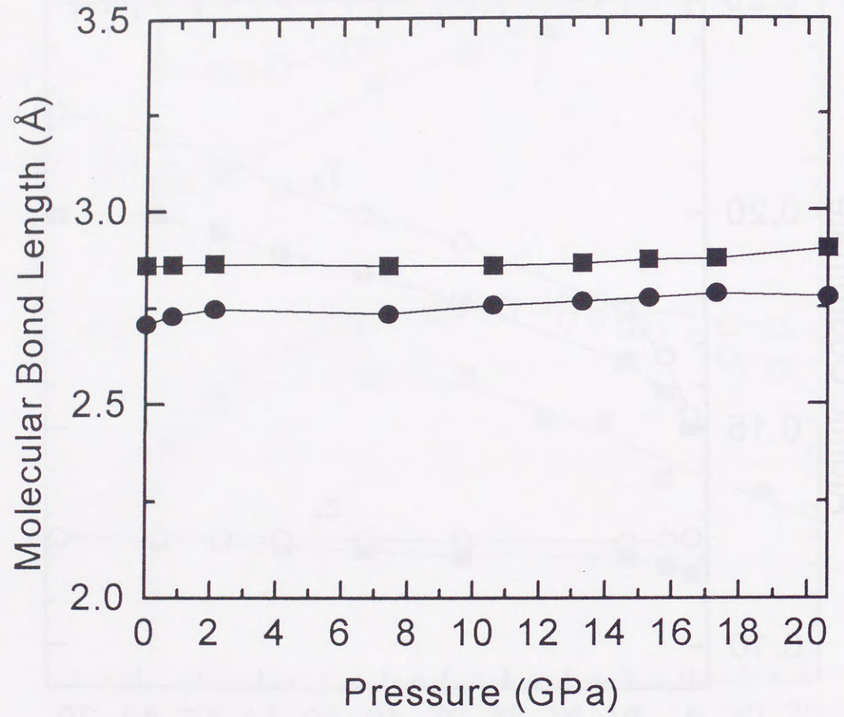

Figure 28: Molecular bond length versus pressure. Filled squares and circles denote the present calculations and the experimental results [18], respectively.

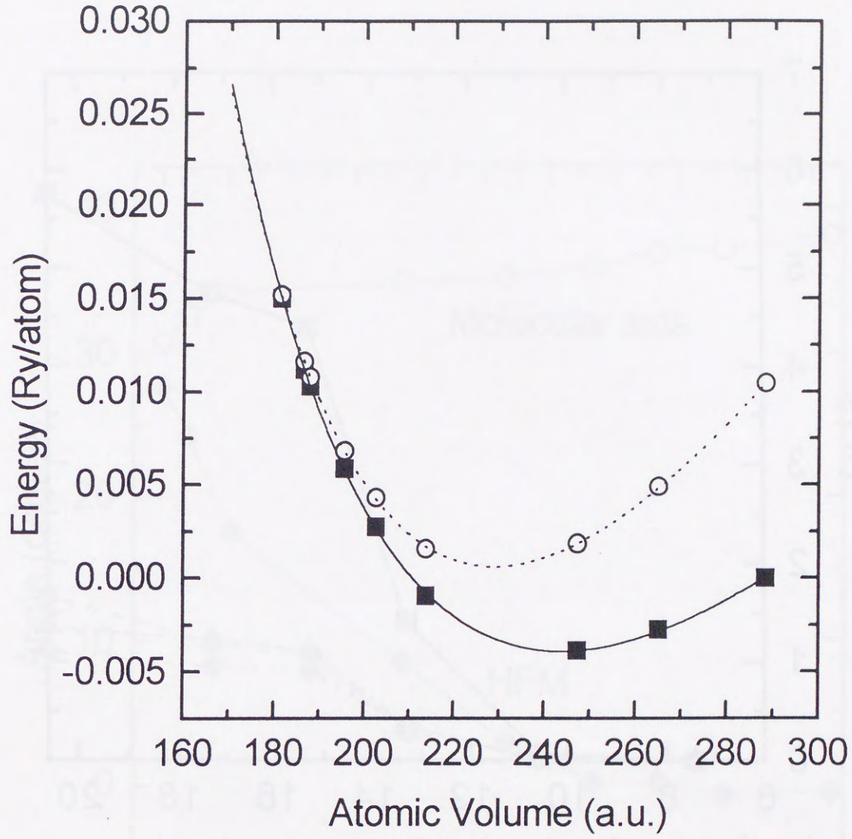

Figure 29: Total energy of the molecular phase and FCO versus atomic volume. Filled squares and open circles denote the calculated results of the molecular phase and FCO, respectively. Solid and dotted lines represent the Murnaghan's EOS fitted for the molecular phase and FCO, respectively.

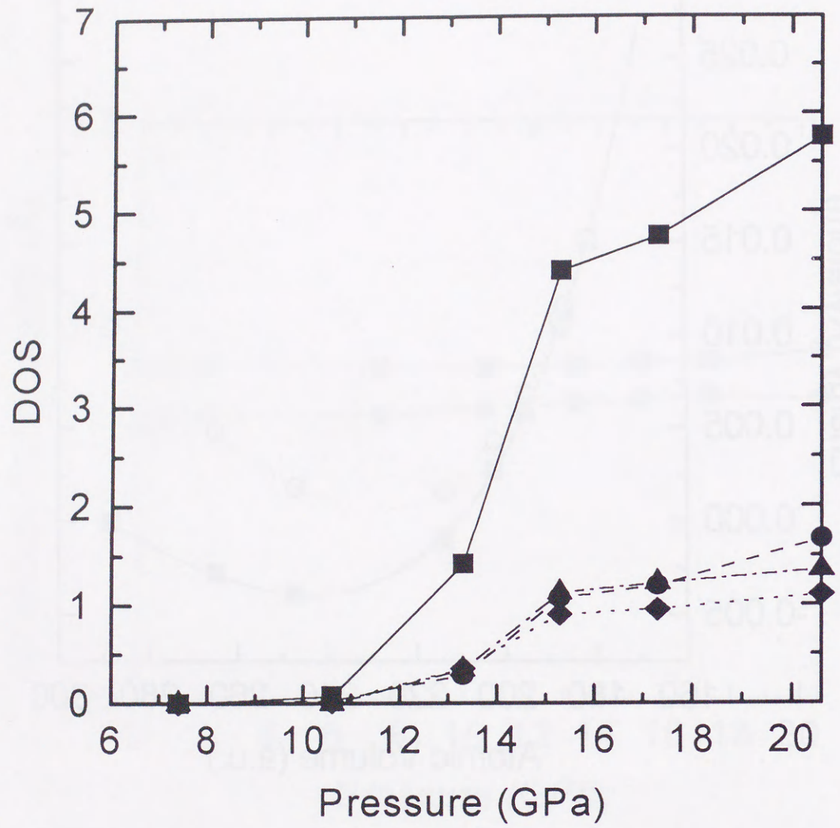

Figure 30: Total and partial DOS of the molecular phase, which is calculated with the equilibrium structures of frozen-phonon calculations, at Fermi level. Filled squares, triangles, circles, and diamonds denote the total, p_x, p_y, and p_z DOS respectively.

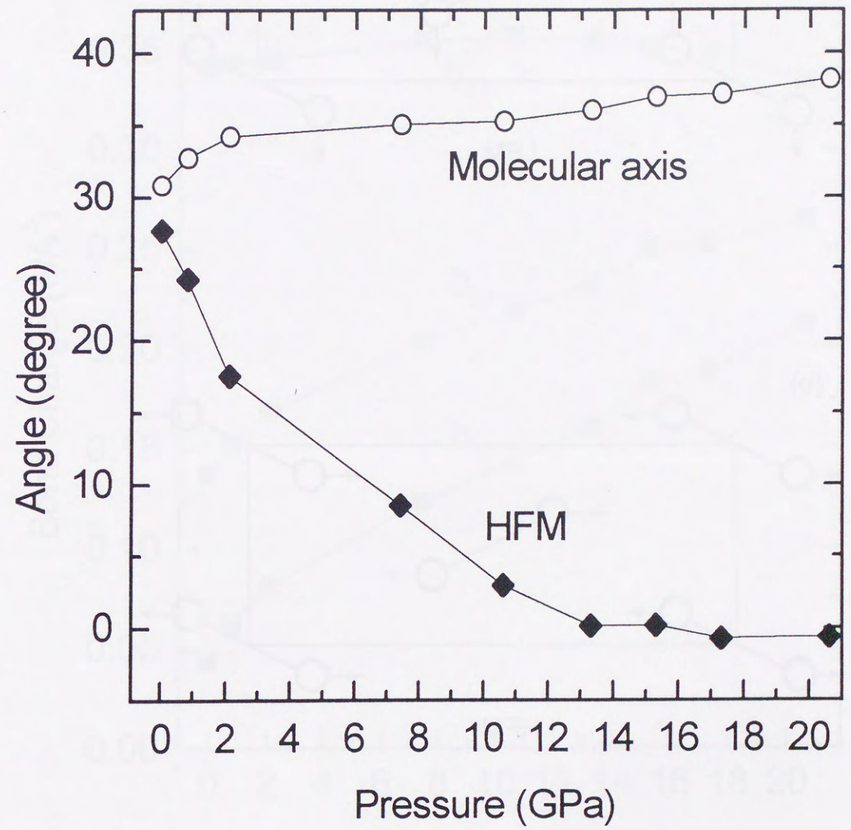

Figure 31: Pressure dependence of the directions of molecular axis and eigenvector of HFM with respect to the c-axis.

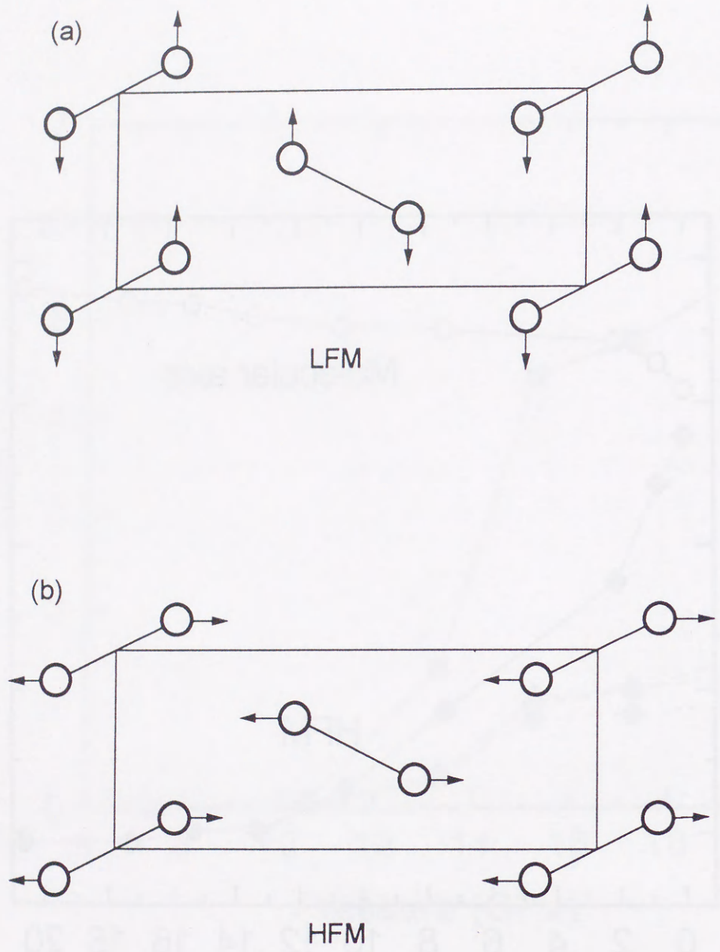

Figure 32: Two A_g modes of molecular solid iodine in metallic state at $\mathbf{k} = 0$.

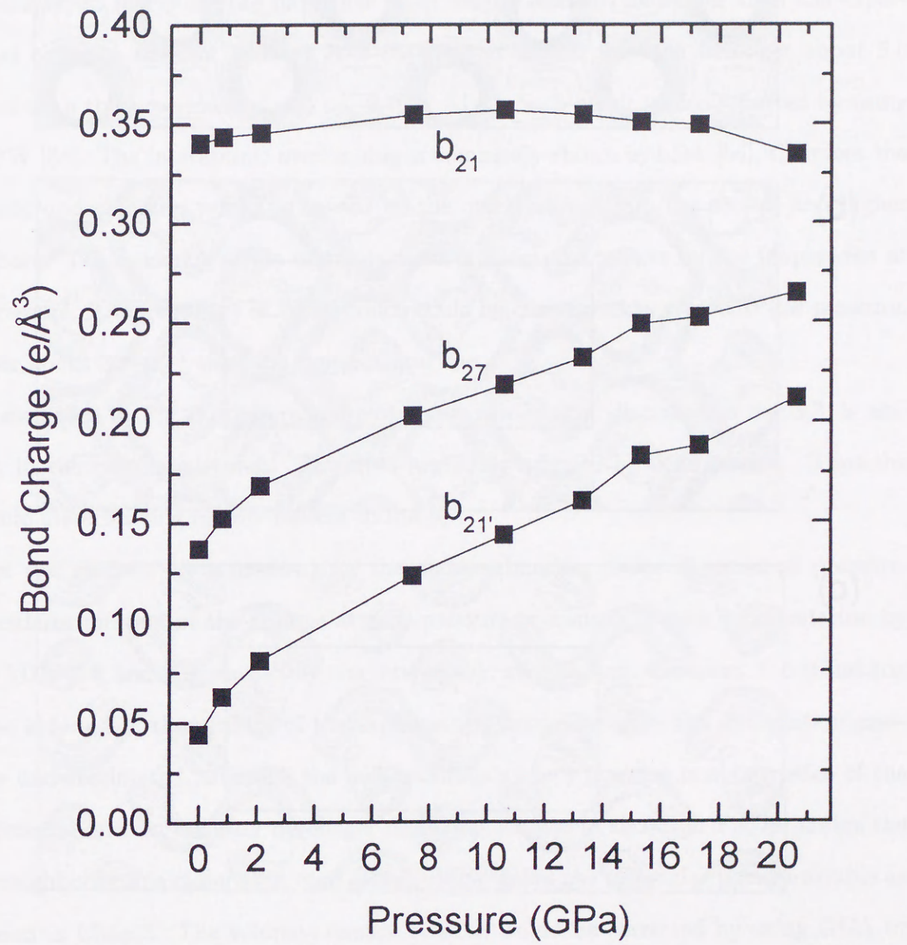

Figure 33: Pressure dependence of the bond charges. Here b_{ij} represents the density at the center of r_{ij}.

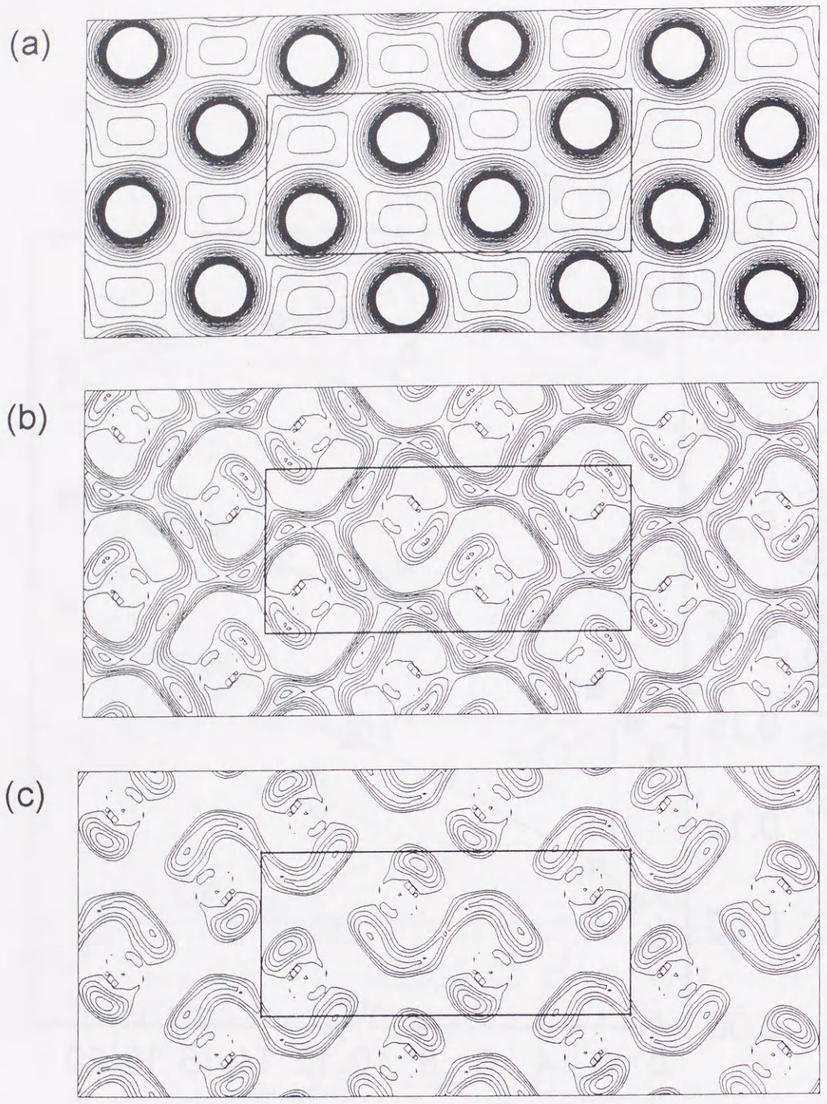

Figure 34: Electronic density $\rho(\mathbf{r})$ of the equilibrium structure at 15.3 GPa on bc-plane is displayed in (a). Plus and minus region of $-\Delta\rho(\mathbf{r})/\rho(\mathbf{r})$ are displayed in (b) and (c) respectively. Here $\Delta\rho(\mathbf{r})$ is defined in Eq.42. The rectangle inside the figures denotes the unit cell. In (a) the contour values are given in 0.1 e/Å^3 and are drawn from 0.1 to 2.5 e/Å^3. In (b) and (c) the contour values are given in 0.05 percent and are drawn from -0.4 to 0 and 0 to 0.25 percent respectively.

4.3 Discussions

As displayed in Fig.28, the molecular bond length tends to be longer than the experimental one. At ambient pressure it is obtained as 2.8610 Å which is longer about 5.6 percent than the experimental one, i.e. 2.7082 Å[18]. Such result is also reported by using FLAPW [58]. The interatomic overbinding is commonly shown in LDA [54], therefore the diatomic underbinding would be caused by the overbindings from the second and higher neighbors. The tendency of the diatomic underbinding also reflects on the frequencies at low pressure: The frequency of HFM, which could be considered as vibron at low pressure, is lower about 30 cm^{-1} than the experimental one.

As displayed in Fig.27, the gradual molecular dissociation, discussed in Sec.3.3, is also shown in the calculated result. The z_0 is negligibly affected by compression. Thus the diatomic underbinding mainly reflects to the y_0.

Here two reasons are considered for the underestimation of the dissociation pressure. The underestimation of the volume at zero pressure is commonly seen in calculation by using LDA [54] and it is caused by the interatomic overbinding. However, the transition volume is found in the vicinity of the experimental one. Therefore the dissociation pressure is underestimated, although the bulk modulus at zero pressure is about twice of the experimental one. In addition the longer molecular length, as shown in Fig.28, makes the third neighbors come closer with each other, which makes the molecular phase unstable as discussed in Chap.3. The volume-pressure relation would be corrected by using GGA or any other improved method [54].

The LDA underestimates also band gap [54], and therefore the band overlap is occurred at lower pressure than the observed one [7].

The change in the direction of the eigenvector (Fig.31) suggests that the intra- and intermolecular bondings become to be equivalent with increasing pressure. Especially, as displayed in Fig.32, the restoration forces with respect to the bonding 2-1 and 2-1' would be

nearly the same above 10 GPa. At low pressure region HFM could be regarded as vibron, and the mixing between vibron and libron is mostly reflected on the softening of HFM as displayed in Fig.26.

The pressure dependence of the bond charges suggests the equivalence between intra- and interatomic bonding at compressed state (Fig.33). Such a behavior is also found by the X-ray experiment [17].

To investigate the properties of the band overlap the difference between the density of fictitious insulating state and the one of real metallic state is calculated:

$$\Delta\rho(\mathbf{r}) \equiv \sum_{i\in I} |\psi_i(\mathbf{r})|^2 - \sum_{i(\varepsilon_i \le \varepsilon_F)} |\psi_i(\mathbf{r})|^2 \tag{42}$$

where I represents the set of bands which are occupied at the low pressure insulating state and ψ_i is the Kohn-Sham orbital which is obtained by usual self-consistent procedure. Plus and minus region of $-\Delta\rho(\mathbf{r})/\rho(\mathbf{r})$ are displayed in Fig.34 (b) and (c) respectively. At the plus region the electronic density is increased by the band overlap, and the minus is decreased. As displayed in Fig.34 the band overlap transfers the electrons from intra- to intermolecular region. Therefore the slight decrease of the intramolecular bond charge b_{21} above 10 GPa is caused by the band overlap. Furthermore the equivalence between intra- and intermolecular bonding is also caused by the band overlap. As a result the A_g normal modes direct as shown in Fig.32 in the metallic state.

Interestingly, the direction of normal mode of LFM is identical with the transverse phonon of FCO which is used to explain the dimerization in Chap.3. As shown in Fig.34, the increase of bond charge $b_{21'}$ with increasing pressure is enhanced by the band overlap. By the bond charge model [37] as discussed in App.A the transverse phonon of FCO is softened by the bond charge $b_{21'}$: The repulsion between 2 and 1' atoms is mediated by the electronic densities. It is suggested that the softening of LFM is caused by the band overlap. On the other hand, the softening of LFM (the transverse phonon of FCO) with increasing pressure is the result of gradually decreased energy difference between the molecular phase and the monatomic FCO as discussed in Chap.3. Therefore the softening

of LFM is just a precursor of the molecular dissociation as suggested by Shimomura *et al.* in 1982 [23].

Band gap is underestimated commonly by LDA [54], and therefore the softening of LFM in the band overlap state occurs above 10 GPa as displayed in Fig.26. The overestimated softening in LFM is coming from the overestimate of the band overlap.

Here the X band reported by Olijnyk *et al.* [25] should be focused. They said that " *The evolution with pressure of the librational* A_g *mode ... suggests that a new peak (labeled X) emerges on the low-frequency side and grows in intensity , whereas the original peak has nearly vanished around 20 GPa*". It seems that the metallic and the insulating molecular phase coexisted in their sample because of the pressure gradient: The X band would be coming from the metallic state. The abrupt change in the electronic state caused by the band overlap might affect abruptly phonon frequencies. In the experiment, the jump between the original and the X bands is only a few cm^{-1} and the present calculation does not have such accuracy as seen in Fig.26.

4.4 Conclusion of Chap.4

In this chapter, frozen-phonon calculations for the Raman active A_g modes of the molecular solid iodine are presented. The coupling between A_g vibron and libron are increased with increasing pressure. In the band overlap state, HFM, continued from the vibron at ambient pressure, directs along the c-axis, and LFM, continued from the libron at ambient pressure, directs along the b-axis. It is caused by the effect of the band overlap, i.e. the intramolecular electrons are transferred to the intermolecular region. Above 10 GPa LFM is softened with increasing pressure. The eigenvector along the b-axis is just identical with the transverse phonon of FCO at the center of Σ line. In Chap.3, the softening of energy curvature along the b-axis is indicated as an evidence of decrease in the difference between energy of the molecular phase and FCO. Therefore the softening of LFM is recognized as an evidence of the gradual molecular dissociation. as suggested by Shimomura *et al.*

In the present calculation the transition pressure between the molecular phase and FCO is 13 GPa. The underestimation of the dissociation pressure is caused by using LDA.

To survey the molecular dissociation and scaling rule of halogens [65] quantitatively, the following quantities should be calculated at each volume with the accuracy 0.1 mRy per atom or higher:

$$E_{Mol}(V) = E_t(V) + \delta E_f(V) - \delta E_m(V), \quad (43)$$

$$E_{BCO}(V) = E_t(V) - \delta E_b(V), \quad (44)$$

where E_t is the total energy of BCT as an undistorted structure of all the phases, δE_f is the difference between FCO and BCT, δE_m is the difference between FCO and the molecular phase, and δE_b denotes the difference between BCO and BCT. One should notice that all the quantities are to be optimized with respect to the ratio of lattice parameters.

5 Mössbauer Effects of Solid Iodine Under Pressure

In this chapter, by using FP-LMTO the experimental results of the Mössbauer spectroscopy of iodine under pressure are explained on the basis of the molecular dissociation picture proposed by X-ray experiments. In the Mössbauer spectroscopy coupling between nuclear quadrupole moment and EFG at the nucleus is measured. The isomer shift is the energy difference coming from the change in the size of nucleus between ground- and excited states and electronic density at the nucleus, the so-called contact density. Calculations of the contact density and EFG at the nucleus under the molecular dissociation picture are presented. Theory of EFG is summarized in App.B. In figures, the experimental values of EFG are represented in V/m^2 with the nuclear quadrupole moment $Q = -0.55$ barn ($10^{-28}m^2$) for ^{129}I [59] and the contact densities are in e/a_0^3 with the calibration constant $\alpha = 0.213$mm sec^{-1} a_0^3 [66].

5.1 Results for molecular phase

In the molecular phase, the lattice parameters at each pressures are taken from the recent X-ray experimental results [18], and are displayed in Fig.4(a).

The calculated EFG and asymmetry parameter η with the observed atomic position, which is displayed in Fig.4(b), are shown in Fig.35. The difference between the molecular axis and the principal axis of EFG is increased with increasing pressure as displayed in Fig.36. The change of the principal axis of EFG does not occur up to 20.6 GPa.

The EFG's and η's with the equilibrium atomic position, which is obtained by the frozen-phonon calculations described as Chap.4, are displayed in Fig.37. At low pressures the principal axis of EFG also nearly directs along the molecular axis as shown in Fig.38. Above 15.3GPa, however, it directs along the a-axis and the sign of Φ_{zz} is changed.

Contact densities versus pressure are displayed in Fig.39. The fitted value of $\frac{d\rho(0)}{dln(V/V_0)}$ is $-3.23\ a_0^{-3}$ with the X-ray experimental structure and $-2.51\ a_0^{-3}$ with the equilibrium structure. The experimental $\frac{d\rho(0)}{dln(V/V_0)}$ equals $-6.6(2)a_0^3$ [22]. This is about twice value of the calculated result.

5.2 Results for monatomic phase

In monatomic phase, the lattice parameters at each pressures are taken from the X-ray experimental results [13]. The calculated results of EFG and asymmetry parameter η are shown in Fig.40. The principal axis of EFG directs along the c-axis. A large value of the asymmetry parameter is obtained, that is $\eta = 0.49$ at 30 GPa.

Contact densities versus pressure are displayed in Fig.39. The values are negligibly changed with increasing pressure.

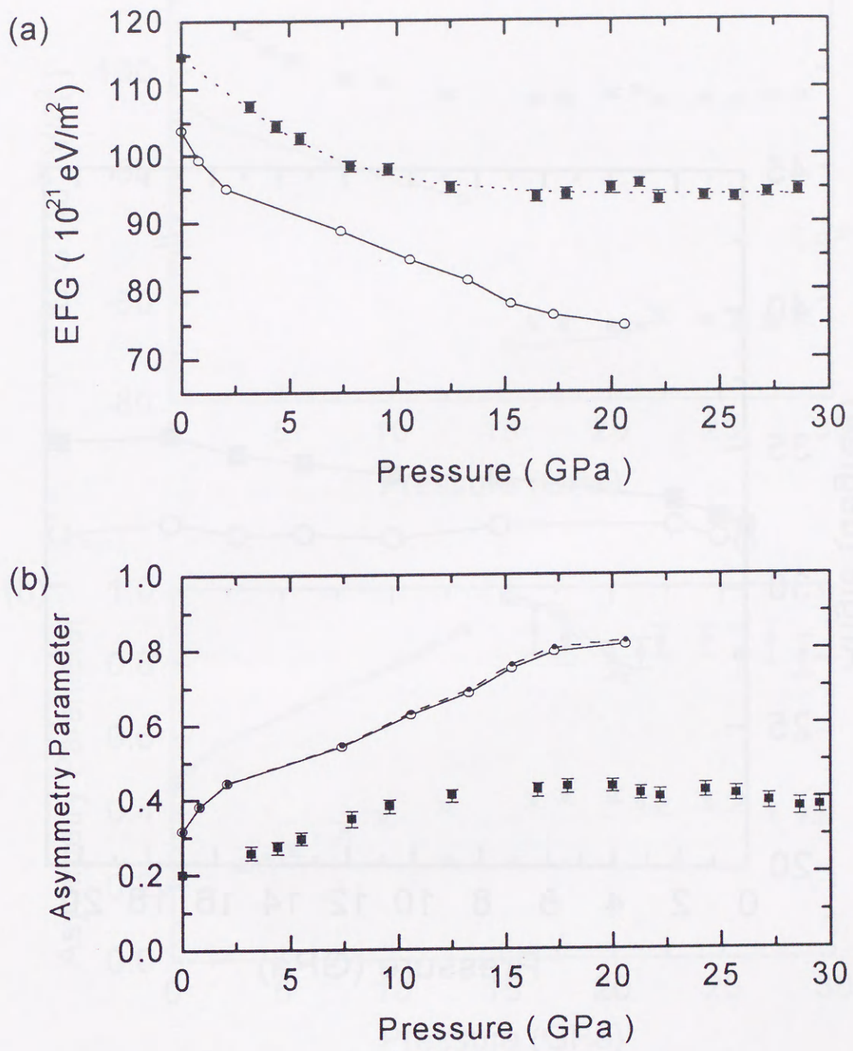

Figure 35: Pressure dependence of (a) EFG and (b) asymmetry parameter. Filled squares and open circles denote experimental results of LP [20] and calculated results with the X-ray experimental atomic position, respectively. In (b) the asymmetry parameter calculated by Eq.(B-20) is represented by small filled circle.

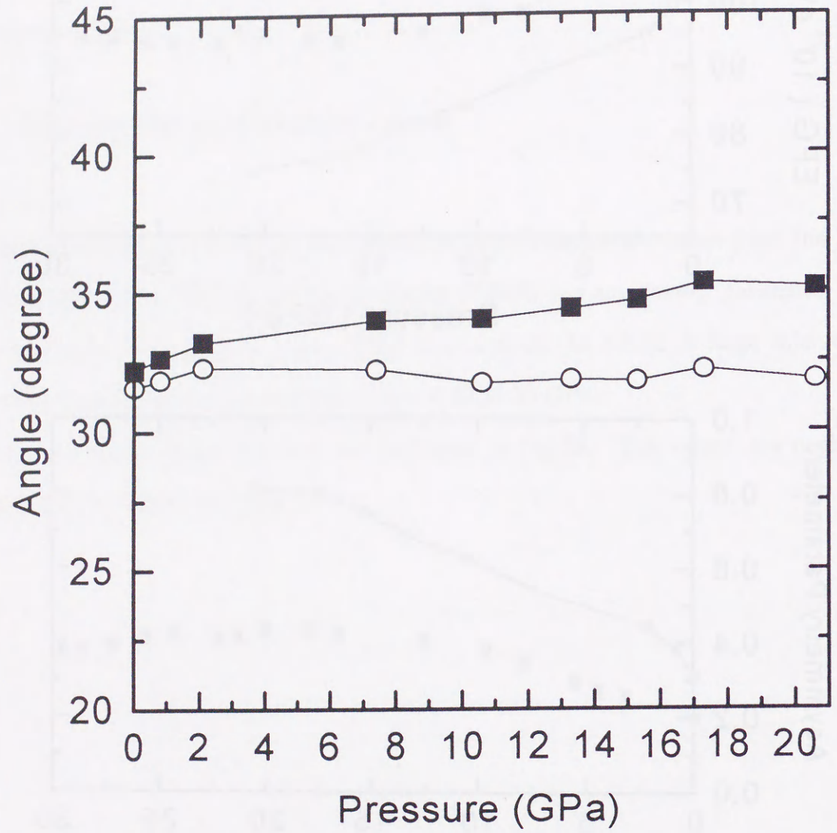

Figure 36: Angles of molecular axis and principal axis of EFG with respect to the c-axis. Filled squares and open circles denote the experimental molecular angles and calculated EFG results, respectively. The structure is observed by X-ray experiment [18].

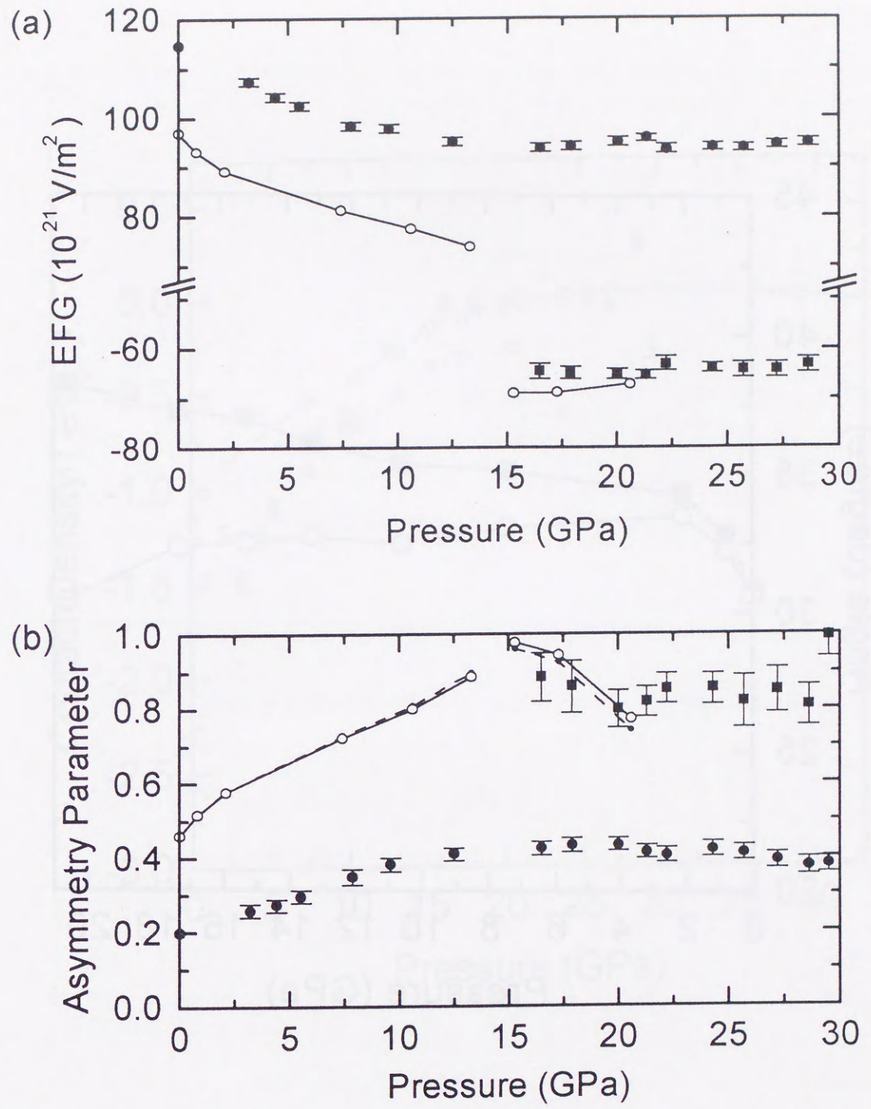

Figure 37: Pressure dependence of (a) EFG and (b) asymmetry parameter with the equilibrium structures of frozen-phonon calculations (Chap.4) at each pressures. Open circles denote the present results. Filled circles and squares denote the experimental results of LP and HP1 [20] respectively. In (b) the asymmetry parameter calculated by Eq.(B-20) is represented by small filled circle.

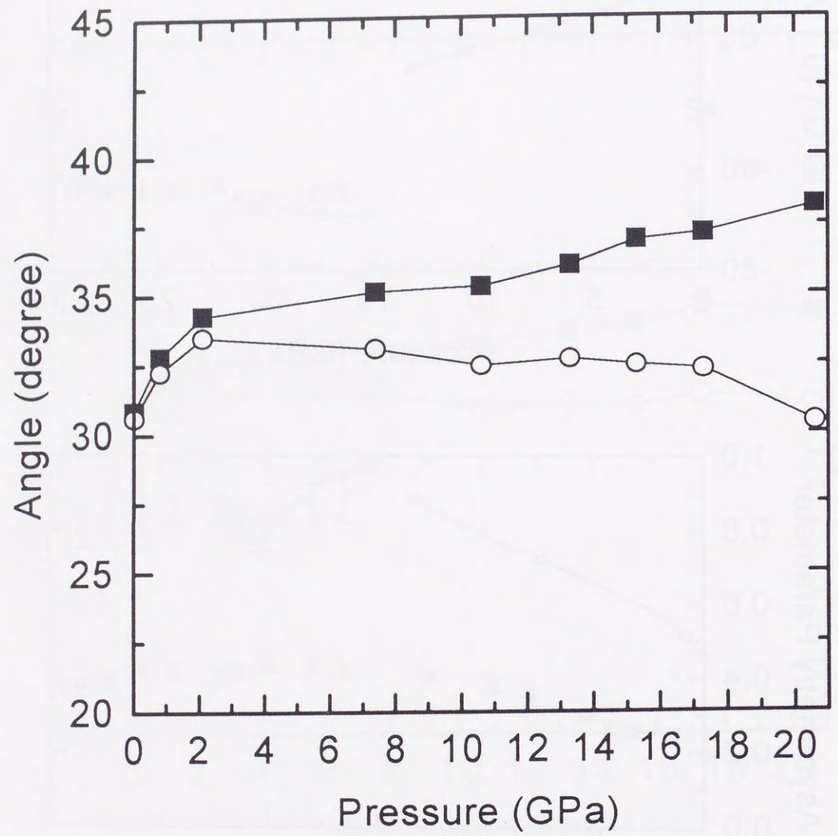

Figure 38: Angles of molecular axis and principal axis of EFG with respect to the c-axis in the equilibrium structure of frozen-phonon calculations. Filled squares and open circles denote the molecular axes and calculated EFG results, which are the Φ_{yy}'s directions above 15.3 GPa, respectively.

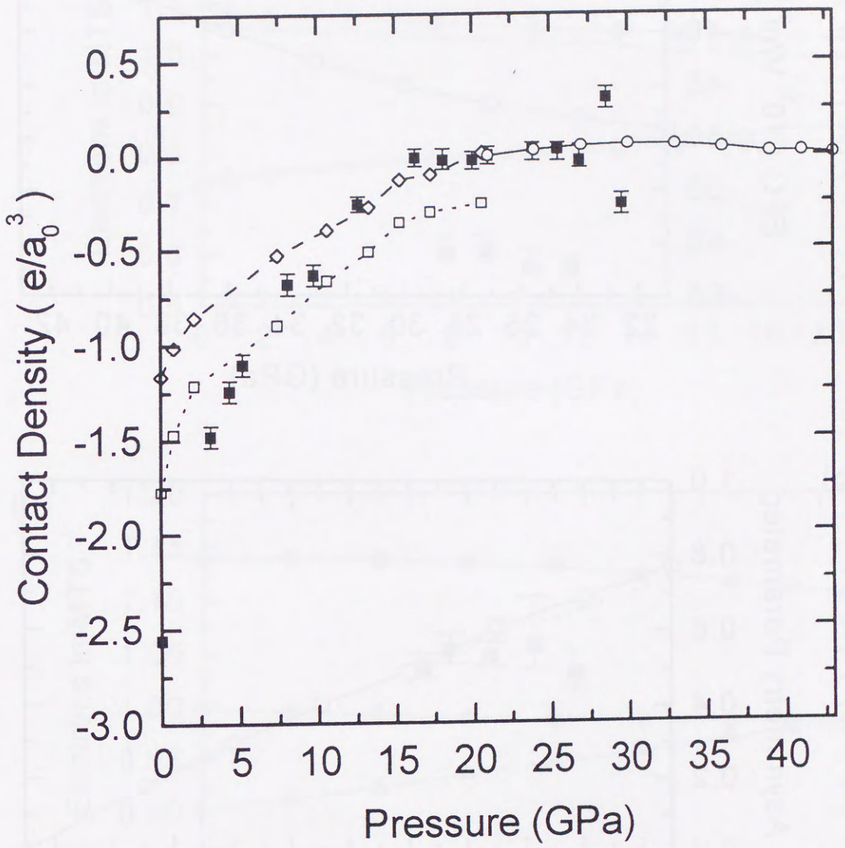

Figure 39: Contact densities versus pressure. Filled squares, open squares, open diamonds, and open circles denote the experimental results [22], calculated results of molecular phase with the experimental structure, calculated results of molecular phase with the equilibrium structure, and calculated results of BCO with the experimental structure, respectively. These are measured from the calculated value of BCO at 21 GPa.

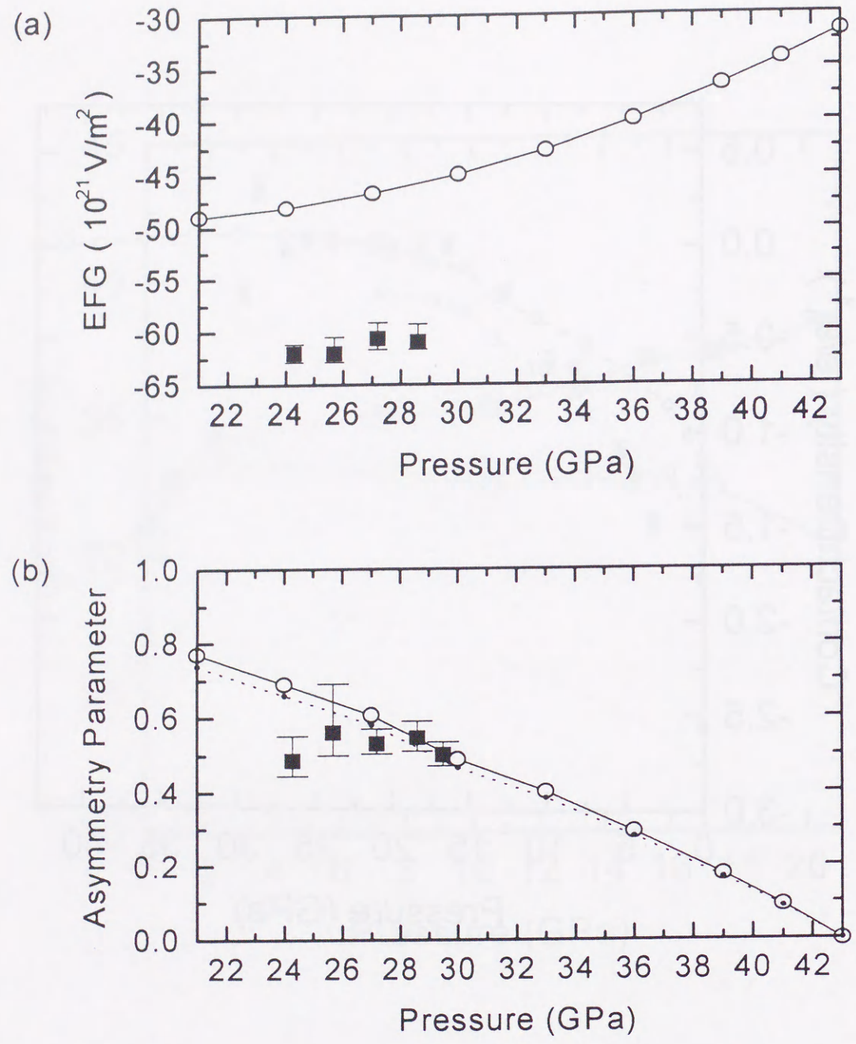

Figure 40: Pressure dependence of (a) EFG and (b) asymmetry parameter with the X-ray experimental structures of BCO [13] at each pressures. Open circles denote the present results. Filled squares denote the experimental results of HP2 [20]. In (b) the asymmetry parameter calculated by Eq.(B-20) is represented by small filled circle.

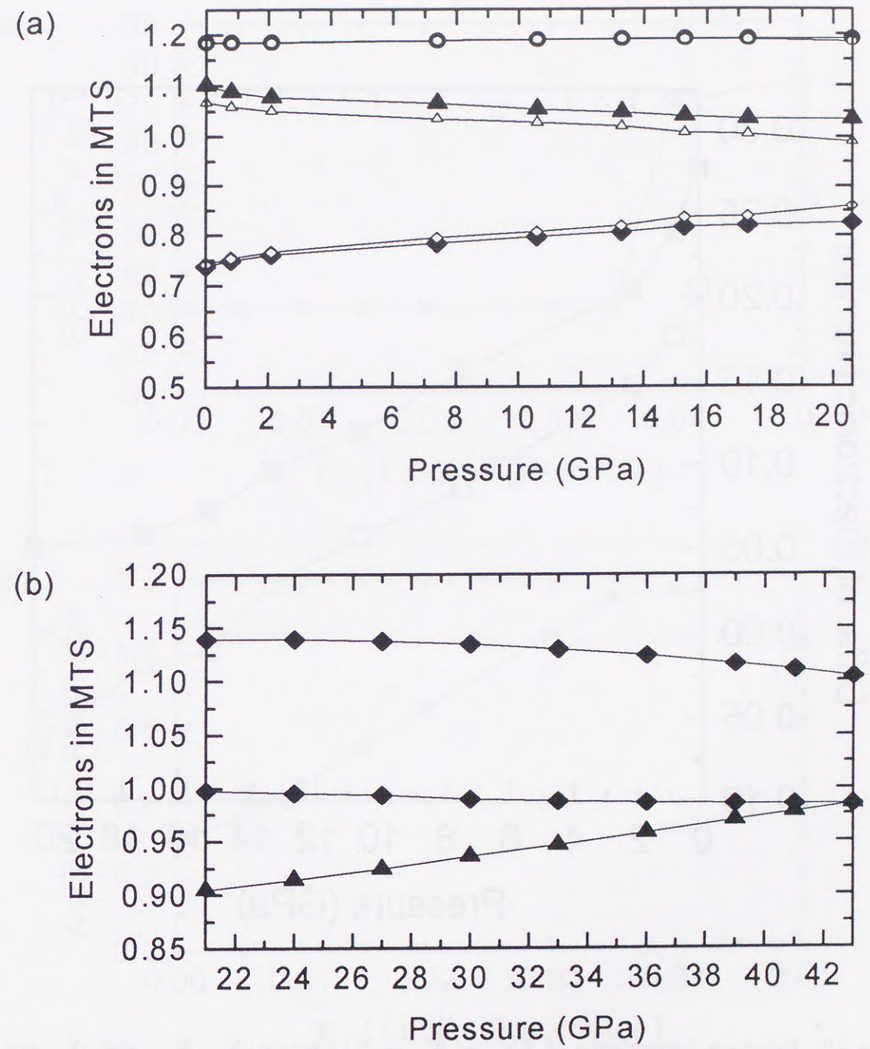

Figure 41: Pressure dependence of occupation number of $5p$-electrons in MTS for (a) the molecular phase and (b) BCO. Triangles, circles, and diamonds denote the number of p_x, p_y, and p_z, respectively. In (a) filled and open notations denote the calculated results with the experimental structure and with the equilibrium one, respectively.

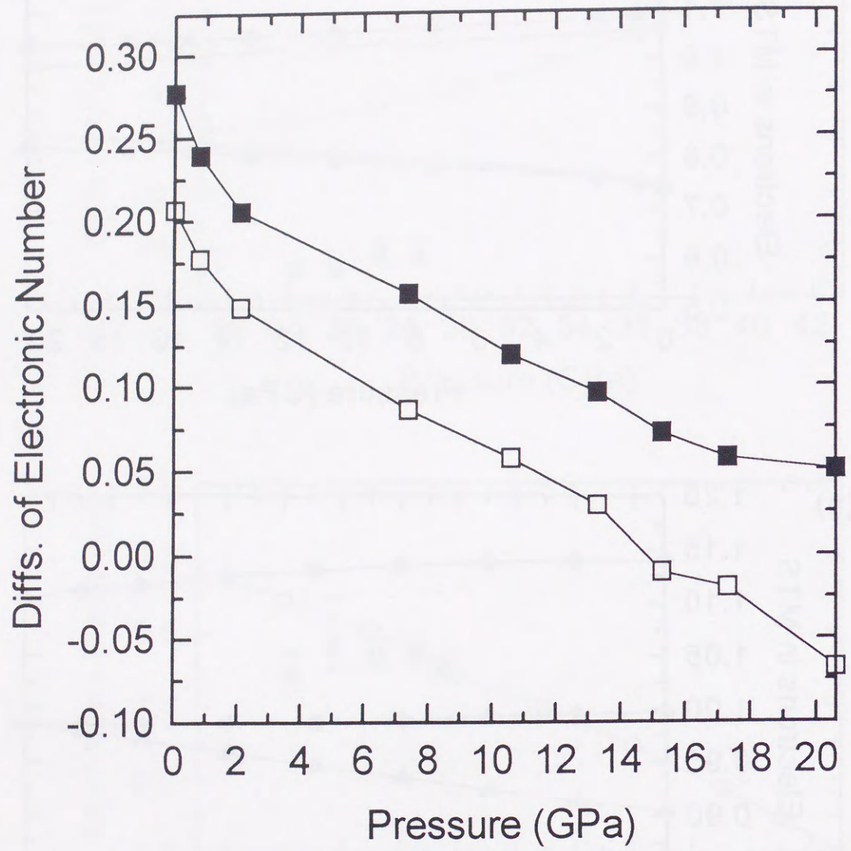

Figure 42: Pressure dependence of $2N_{p_x} - N_{p_y} - N_{p_z}$, where N_{p_x}, N_{p_y}, and N_{p_z} are the occupation number of p_x, p_y, and p_z respectively and are displayed in Fig.41. Filled and open squares denote the calculated results with the experimental structure and with the equilibrium one, respectively. As displayed in Fig.37, the principal axis of EFG changes, when the sign of $2N_{p_x} - N_{p_y} - N_{p_z}$ changes.

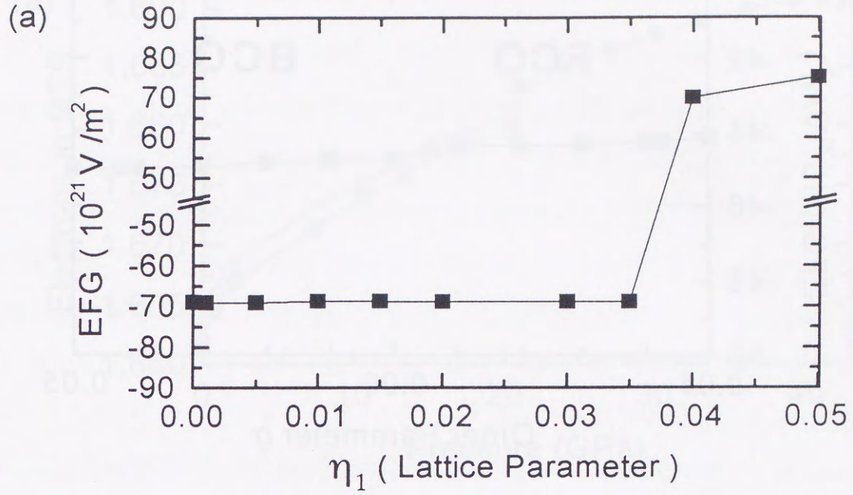

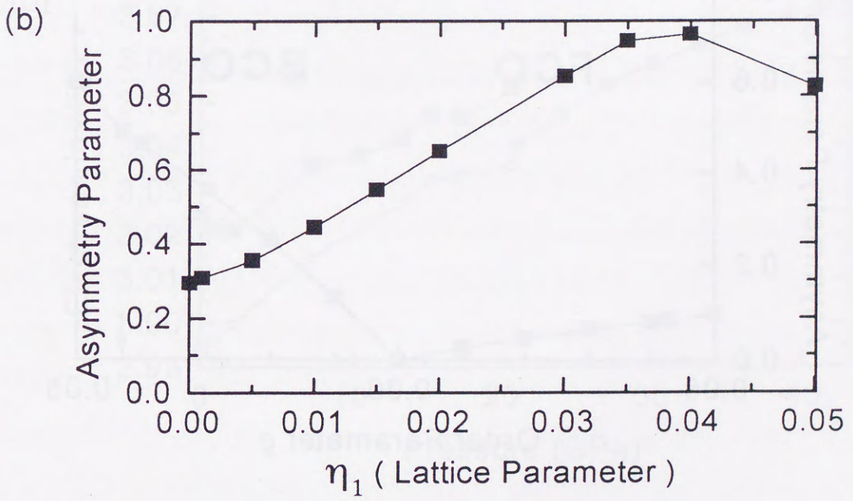

Figure 43: EFG (a) and asymmetry parameter (b) versus the amplitude of the transverse FCO phonon η_1. Lattice parameters are taken from the X-ray experimental results [18] at 15.3 GPa.

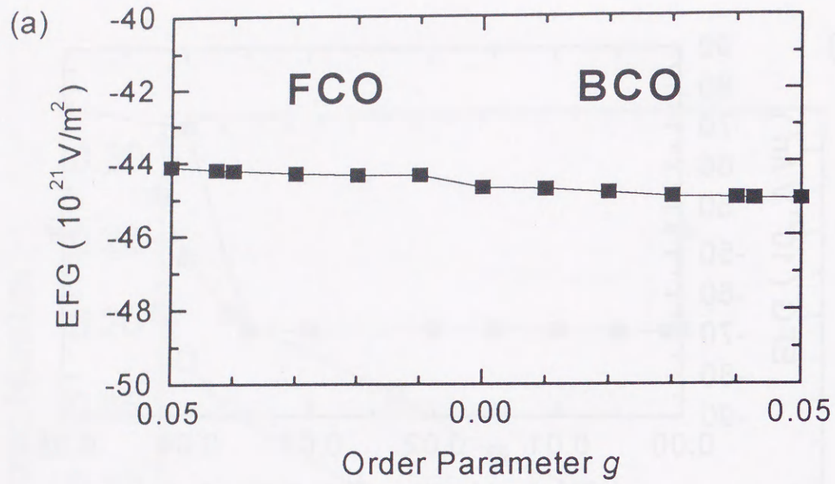

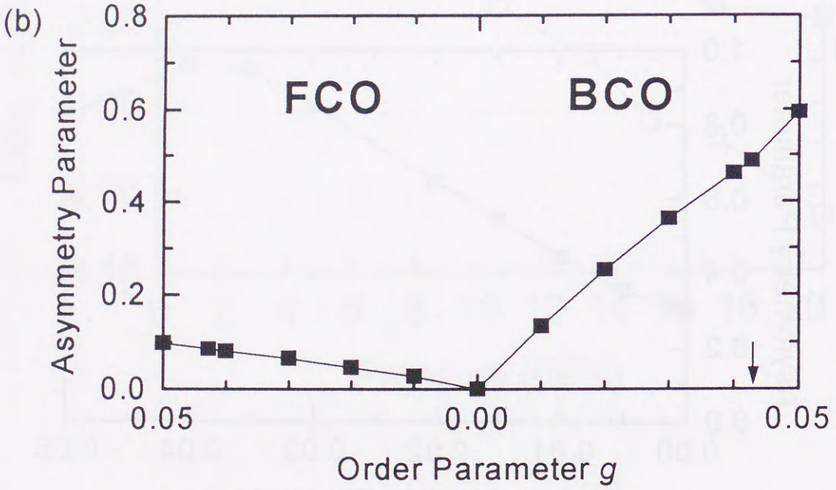

Figure 44: EFG (a) and asymmetry parameter (b) versus orthorhombic distortion in FCO and BCO. The atomic volume and the lattice parameter along z axis is taken from the X-ray experimental values at 30 GPa [36]. The arrow denote the experimental structure $g = \frac{|a_i - b_i|}{\sqrt{a_i b_i}} = 0.04281$.

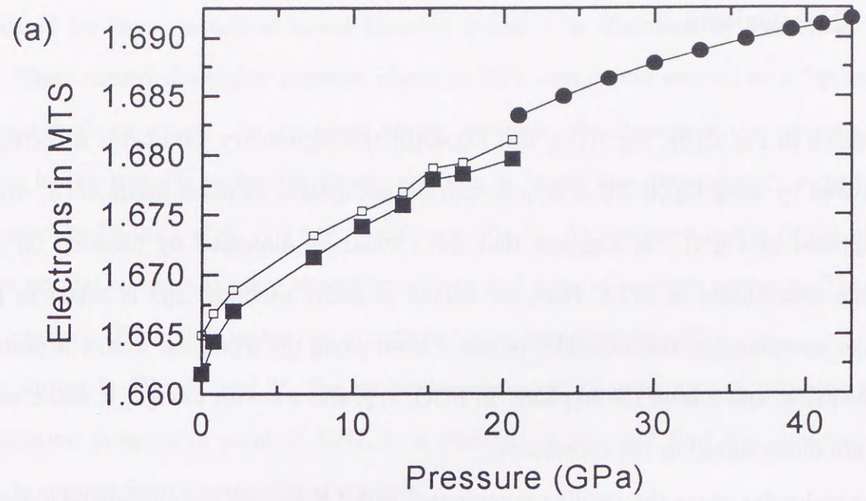

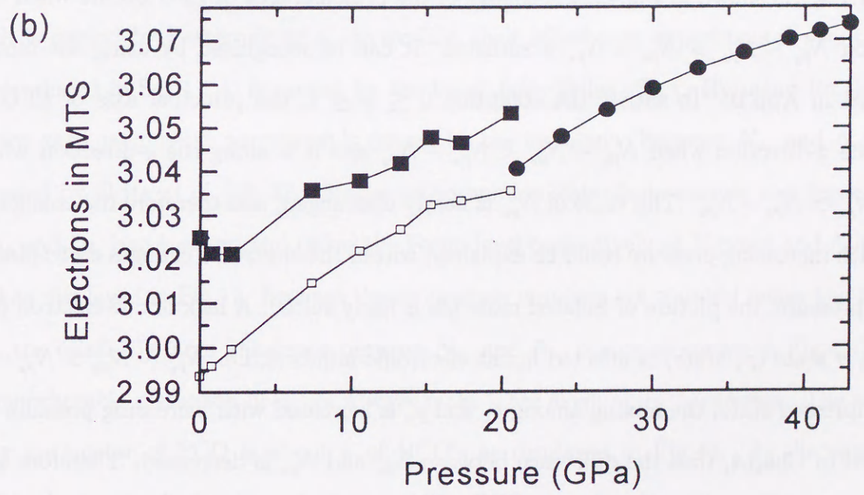

Figure 45: Pressure dependence of occupation number of (a) 5s- and (b) 5p-electrons in MTS. Squares and circles denote the number of the molecular phase and BCO, respectively. Filled and open squares denote the calculated results with the experimental structure and with the equilibrium one, respectively.

5.3 Discussions

As shown in Fig.35(b), Fig.37(b), and Fig.40(b) the asymmetry parameter is correctly recalculated by using Eq.(B-20) of App.B with the occupation numbers inside MTS, which are displayed in Fig.41. It suggests that EFG could be discussed by focusing on the electronic distribution in MTS. Here, as defined in above sections, xyz is taken as the molecular coordinate in the molecular phase: z is set along the molecular axis, y is normal to the bc-plane, and x is on the bc-plane. In BCO, x, y, and z are set along a, b, and c axes: EFG's are diagonalized in the coordinate.

In the molecular phase the results are compared with LP and HP1, which are introduced in Sec.1.1.4. As shown in Fig.42, the change of the principal axis of EFG occurs when the condition $N_{p_y} - N_{p_x} > N_{p_x} - N_{p_z}$ is satisfied. It can be recognized by using the model discussed in App.B: To satisfy the condition $0 \leq \eta \leq 1$, the principal axis of EFG is along the z-direction when $N_{p_y} - N_{p_x} < N_{p_x} - N_{p_z}$ and it is along the y-direction when $N_{p_y} - N_{p_x} > N_{p_x} - N_{p_z}$. The value of N_{p_y} is nearly unchanged, and therefore the change of EFG with increasing pressure could be explained within the electronic changes on bc-plane. At low pressure, the picture of isolated molecule is fairly suited: A lack of one electron per atom in σ state (p_z state) is affected in the electronic numbers, i.e. $N_{p_y} \sim N_{p_x} > N_{p_z}$. In the compressed state, the mixing among p_z and p_x is increased with increasing pressure as discussed in Chap.4, thus the difference between N_{p_x} and N_{p_z} is decreased. Therefore the change of the principal axis of EFG is also an evidence of the gradual molecular dissociation.

The mixing in the equilibrium structure is larger than the X-ray experimental's, because the y_0 value of the equilibrium structure is larger than the X-ray experimental's one as shown in Fig.27. Therefore the change of the principal axis of EFG occurs in the equilibrium structure. It is apparently recognized by the η_1 $(= \frac{1}{4} - y_0)$ dependence of EFG and the asymmetry parameter as displayed in Fig.43.

As discussed above, the change of the principal axis of EFG with increasing pressure

is caused by the approach of atoms between 2 and 1' as discussed by Pasternak *et al.* [20]. They named the higher pressure phase as HP1, and it was seemed as a "quasi one-dimensional" structure. As discussed above, however, the change of the principal axis occurs in the metallic molecular phase, and it is a "quasi two-dimensional" structure as discussed by Fujihisa *et al.* [17] and as shown in Fig.34. As displayed in Fig.16 the atomic layers normal to the c-axis are almost equally spaced even at ambient pressure. Therefore the approach of 2 and 1' makes the structure "quasi two-dimensional".

As shown in Figs.36 and 38, the molecular character remains even at vicinity of the dissociation pressure in point of EFG. It is reflected by the fact that the observation of EFG is coming from the vicinity of nucleus.

As explained by the author and Miyagi [67], the high asymmetry parameter of BCO, which is denied by Pasternak *et al.* to explain their Mössbauer experimental results [20] as introduced in Sec.1.1.4, is caused by the band Jahn-Teller effect. By using Eq.(B-20), the non-zero asymmetry parameter is caused by the imbalance between N_{p_x} and N_{p_y}. As discussed by Orita *et al.* [28, 32, 33], the orthorhombic distortion removes the degeneracy of $5p_x$ and $5p_y$ bands above and below the Fermi level respectively at X-point and Λ-line of BCO as displayed in Fig.11. Because the occupation numbers are counted below the Fermi level, the relatively large imbalance between N_{p_x} and N_{p_y} occurs as shown in Fig.41(b).

Orthorhombic distortion does not always make large asymmetry parameter: The asymmetry parameter of FCO is about $\frac{1}{5}$ of BCO's as displayed in Fig.44. As discussed in Sec.3.2, the band splitting is so small to stabilize FCO, therefore the asymmetry parameter could not be large. Within the discussion in App.A, the bond charge wave, created not in FCO but in BCO, is also taken as the origin of large asymmetry parameter: The imbalance between N_{p_x} and N_{p_y} is caused by the bond charge wave as shown in Fig.A-2.

The answer to the claim of Pasternak *et al.*'s [20] summarized in Sec.1.1.4(2) is that the large asymmetry parameter of EFG in BCO is caused by the imbalance between N_{p_x} and N_{p_y}.

In the $5s$-$5p$ elements, the contact density $\rho(0)$ is often expressed in the simple form [61],

$$\rho(0) = const. + An_s - Bn_p, \tag{45}$$

where An_s is the increase in $\rho(0)$ due to the addition of n_s electrons with s-character and Bn_p is the decrease in $\rho(0)$ due to shielding of the s-electrons by n_p electrons with p-character. Pressure dependence on n_s and n_p, which are the electronic number of $5s$ and $5p$ states in MTS respectively, are displayed in Fig.45. In the molecular phase, the best fitted values for A and B are 100.34 a_0^{-3} and 9.52 a_0^{-3}, respectively. In BCO, A and B are 101.52 a_0^{-3} and 24.92 a_0^{-3}, respectively.

In the molecular phase, the increase of the contact density is caused by the increase of n_s with increasing pressure, and it is mediated by the shielding from the increased n_p electrons.

At 21 GPa, the transition pressure, the change of the contact density is about 0.25 e/a_0^3 as displayed in Fig.39 from the experimental molecular structure to BCO. The negligible change from the equilibrium molecular phase to BCO, i.e. -0.02 e/a_0^3, as displayed in Fig.39, is caused by cancellation between the last two terms in (45): As shown in Fig.45, the effect of the abrupt increase in n_s is mediated by the abrupt increase of the shielding from the abruptly increased n_p electrons. In the experiment the change of the isomer shift is not observed at 21 GPa [22]. By Pasternak *et al.*, it was taken as the evidence of the absence of volume change caused by the first-order transition at 21 GPa, as summarized in Sec.1.1.4(4). However, the present work indicates that the effect of abrupt volume change is mediated by the cancellation between the last two terms in (45).

In BCO, the contact density varies negligibly up to 43 GPa: It is consistent with the results of the isomer shift measured up to 30 GPa [22]. It is also caused by the cancellation between the last two terms in (45).

Finally, the three phase coexistence proposed by Pasternak *et al.* [20] is considered. By using Gibbs's phase rule, in equilibrium one component system the thermodynamic degrees of freedom is zero for three phase coexistence state [68]. Because Pasternak *et al.* reported

that the three phase coexistence is observed at various pressures above 24 GPa, the sample would not be in equilibrium.

5.4 Conclusion of Chap.5

In this chapter, the hyperfine parameters of iodine under pressure are calculated within the molecular dissociation picture proposed by X-ray experiments. In the band overlap state, the change of the principal axis of EFG occurs at 15.3 GPa with the equilibrium structure: It is named by Pasternak *et al.* as HP1. It is shown that the change of the principal axis of EFG is also the evidence of the gradual molecular dissociation.

In BCO, a large asymmetry parameter of EFG is obtained, i.e. the value is 0.49 at 30 GPa, and the results of HP2 observed by Pasternak *et al.* agree quite well. It is caused by the imbalance between the occupation number of $5p_x$ and $5p_y$: That is the result of the band Jahn-Teller effect as introduced to explain the stability of BCO by Orita *et al.* Therefore the consistency between Mössbauer and X-ray experiments are found on the basis of the molecular dissociation picture.

Under high pressure, the increase of the contact density caused by the compressed $5s$-electrons are mediated by the shielding from $5p$-electrons. Therefore the change of the contact density at the dissociation pressure is small, 0.25 e/a_0^3 with the experimental structure and -0.02 e/a_0^3 with the equilibrium structure. It is taken as a reason why the change of isomer shift was not discovered at 16 and 21 GPa by Pasternak *et al.* In BCO the value of the contact density changes negligibly with increasing pressure, as observed in isomer shift by Pasternak *et al.* It is also caused by the cancellation between the effect of the compressed $5s$-electrons and the shielding from $5p$-electrons.

6 Conclusion

In the present thesis, properties of solid iodine under high pressure is surveyed by using FP-LMTO within LDA.

The molecular phase is realized from the monatomic FCO structure with the distortion of the transverse phonon at the center of Σ line. The molecular phase becomes unstable with increasing pressure with respect to FCO, that is the gradual molecular dissociation. It is caused by the interaction between third neighbors which come closer with each other with increasing pressure. Because the monatomic FCO structure is unstable with respect to the monatomic BCO one, the molecular dissociation occurs as a first-order transition from the molecular phase to BCO, as observed by Takemura *et al.*

The frozen-phonon calculations for the Raman active A_g modes of the molecular solid iodine are carried out. The mixing between A_g vibron and libron is increased with increasing pressure. Above the band overlap pressure, which is found around 10 GPa in the present work, the direction of "vibron" is along the c-axis and the "libron" along the b-axis. It is indicated that the observed pressure-induced softening of Raman active A_g "libron" in the band overlap state is caused by the gradual molecular dissociation as suggested by Shimomura *et al.*

In the metallic molecular phase, the change of the principal axis of EFG is found, as observed by Pasternak *et al.* above 16 GPa. It is shown that the change of the principal axis of EFG is also the result of the gradual molecular dissociation.

In BCO, a large asymmetry parameter of EFG is obtained, i.e. the value is 0.49 at 30 GPa, and the results of HP2 observed by Pasternak *et al.* agree quite well. It is caused by the imbalance between the occupation number of $5p_x$ and $5p_y$: That is the result of the band Jahn-Teller effect as introduced to explain the stability of BCO by Orita *et al.* Therefore the consistency between Mössbauer and X-ray experiments are found on the

basis of the molecular dissociation picture.

The negligible small change in the isomer shift under high pressure, which is also observed by Pasternak *et al.*, is attributed to the cancellation between the effect of the increasing contact density caused by the compressed $5s$-electrons and that of the increasing shielding by $5p$-electrons.

The following experiments are demanded to support the above results:

(I) Raman scattering studies with polarized light for the single crystal of iodine can detect the direction of Raman active modes, and therefore the change of directions as displayed in Fig.31 could be found.

(II) Mössbauer spectroscopy above 30 GPa will find the decrease of the asymmetry parameter of EFG with increasing pressure, and at 43 GPa, which is the transition pressure from BCO to BCT, the value will vanish.

Quantitative errors found in the present work are mainly coming from the interatomic overbindings and underestimate of band gaps. Both two defects are caused by LDA. Therefore the results would be corrected by using improved density functionals, such as GGA or any other formula.

APPENDIXES

A Bond Charge Model

In this appendix the bond charge model applied to the transition of solid iodine by Luty and Raich [37] are presented. One must notice that this model leads only *a consequence of the adiabatic approximation* [37].

Firstly it is assumed that the undistorted structure is BCT. Then both BCO and the molecular solid phase are distorted structure from BCT within xy-plane, which corresponds to the bc-plane of the molecular phase. BCT has one atom per unit cell and the structure is displayed in Fig.A-1. The lattice parameter of x- and y-direction is denoted as a_0 in this appendix.

Secondly bond charges $\delta\rho$ which are induced by the lattice distortion are located at the center of the interatomic bondings on xy-plane. As displayed in Fig.A-1 two $\delta\rho$'s are located per atom and are labeled with x and y.

The potential energy of lattice distortion is described by dynamical matrix and reduced displacements:

$$\Phi = \frac{1}{2}\sum_{ll'}\sum_{\alpha\beta} D_{\alpha\beta}(ll')u_\alpha(l)u_\beta(l') \qquad (A-1)$$

where l denotes the atom and α denotes the Cartesian component. The system is defined within the periodic boundary condition, then u is performed the Fourier transformation with the wave vector $\mathbf{k}$:

$$u_\alpha(l) = \frac{1}{N}\sum_{\mathbf{k}} u_\alpha(\mathbf{k})e^{i\mathbf{k}\cdot\mathbf{R}_l} \qquad (A-2)$$

where $\mathbf{R}_l$ represents the position of the atom l. After all the potential energy is

$$\Phi = \frac{1}{2}\sum_{\alpha\beta}\sum_{\mathbf{k}} D_{\alpha\beta}(\mathbf{k})u_\alpha(-\mathbf{k})u_\beta(\mathbf{k}) \ , \qquad (A-3)$$

where

$$D_{\alpha\beta}(\mathbf{k}) = \sum_l D_{\alpha\beta}(ll')e^{-i\mathbf{k}\cdot(\mathbf{R}_l-\mathbf{R}_{l'})} \qquad (A-4)$$

for any l'.

The change of the crystal internal energy caused by the bond charges is

$$\delta U = \frac{1}{2}\sum_{ll'}\sum_{\alpha\beta}\phi_{\alpha\beta}(ll')\delta\rho_\alpha(l)\delta\rho_\beta(l') \qquad (A-5)$$

where ϕ represents the effective potential of the interaction between the bond charges. As similar above the bond charges are performed the Fourier transformation and finally

$$\delta U = \frac{1}{2}\sum_{\alpha\beta}\sum_{\mathbf{k}}\phi_{\alpha\beta}(\mathbf{k})\delta\rho_\alpha(-\mathbf{k})\delta\rho_\beta(\mathbf{k}) \ , \qquad (A-6)$$

where

$$\delta\rho_\alpha(\mathbf{k}) = \sum_l \delta\rho_\alpha(l)e^{-i\mathbf{k}\cdot\mathbf{R}_l} \qquad (A-7)$$

and

$$\phi_{\alpha\beta}(\mathbf{k}) = \sum_l \phi_{\alpha\beta}(ll')e^{-i\mathbf{k}\cdot(\mathbf{R}_l-\mathbf{R}_{l'})} \qquad (A-8)$$

for any l'. The following conditions are demanded by the symmetry:

$$a(\mathbf{k}) \equiv \phi_{xx}(\mathbf{k}) = \phi_{yy}(\mathbf{k}) \qquad (A\text{-}9)$$

$$b(\mathbf{k}) \equiv \phi_{xy}(\mathbf{k}) = \phi_{yx}(\mathbf{k}). \qquad (A\text{-}10)$$

Then δU is decomposed as follows:

$$\delta U = \frac{1}{2}\sum_{\mathbf{k}}\left[\delta\rho_A(\mathbf{k})\left\{a(\mathbf{k})+b(\mathbf{k})\right\}\delta\rho_A(-\mathbf{k}) + \delta\rho_B(\mathbf{k})\left\{a(\mathbf{k})-b(\mathbf{k})\right\}\delta\rho_B(-\mathbf{k})\right] \ , \qquad (A\text{-}11)$$

where

$$\delta\rho_A(\mathbf{k}) = \frac{1}{\sqrt{2}}\left[\delta\rho_x(\mathbf{k})+\delta\rho_y(\mathbf{k})\right] \ , \qquad (A\text{-}12)$$

$$\delta\rho_B(\mathbf{k}) = \frac{1}{\sqrt{2}}\left[\delta\rho_x(\mathbf{k})-\delta\rho_y(\mathbf{k})\right] \ . \qquad (A\text{-}13)$$

If the charge conservation per atom is assumed, then the eigenvector Eq.(A-12) is trivial, i.e. $\delta\rho = 0$, and for Eq.(A-13) $\delta\rho = |\delta\rho_x| = |\delta\rho_y|$. Therefore only the antisymmetric solution Eq.(A-13) is to be interested.

The potential of the eigenvalue problem to be solved can be viewed as coming from two separate contributions:

$$\Phi = \Phi_0 - \delta U \ , \qquad (\mathrm{A}-14)$$

where the first term of the right hand side is arising from the forces between "bare" atoms and the second is coming from the indirect interaction between the "bare" atoms mediated by the bond charges. As a consequence of the adiabatic approximation the bond charges are induced to minimize the energy of system, therefore the sign of δU is defined as minus.

Hereafter the mechanism in the creation of $\delta\rho$ is simply assumed: $\delta\rho_\alpha(l)$ is induced by the α component of lattice distortion at l. Furthermore the coupling constant is introduced as follows:

$$\delta\rho_\alpha(l) = Au_\alpha(l). \qquad (\mathrm{A}-15)$$

Because of the orthogonality of eigenvector the bond charge wave with wave number $\mathbf{k}$ couples with the distortion wave which has the same symmetry.

A.1 Γ-point, at $\mathbf{k} = 0$

At $\mathbf{k} = 0$ distortions are classified with the point group D_{4h}. The lattice dynamical problem is to be described by elastic coefficients and elastic stresses. In the Voigt notation the distortion energy is

$$\begin{aligned}\Phi \ = \ & \frac{1}{2}\Big[(c_{11}+c_{12})(s_1+s_2)^2 + c_{33}s_3^2 + 2c_{13}(s_1+s_2)s_3 \\ & +(c_{11}-c_{12})(s_1-s_2)^2 + c_{44}(s_4^2+s_5^2) + c_{66}s_6^2\Big] \ , \qquad (\text{A-16})\end{aligned}$$

where first, second, and third terms are distorted in the A_{1g} symmetry, the forth is in B_{1g}, the fifth is in E_u, and sixth is in B_{2g}.

The bond charge wave described by Eq.(A-13) has the B_{1g} symmetry. Therefore as displayed in Fig.A-2 only the distortion in B_{1g}, i.e. to be BCO, is mediated by the bond

charge wave. From Eq.(A-14) the elastic constant is rewritten as

$$c_{11} - c_{12} = c_{11}^0 - c_{12}^0 - A^2\{a(0) - b(0)\} \qquad (\mathrm{A}-17)$$

where c^0 is the "bare" elastic constant. By sufficiently large coupling constant A, BCT becomes unstable and BCO is realized. This is the answer by this model for the problem, why the orthorhombic distortion from BCT is realized only in BCO not in FCO. FCO is realized by the distortion in B_{2g} and is not energetically lowered by the bond charge wave.

A.2 Δ-direction, at $\mathbf{k} = (\pi/2a_0, \pi/2a_0, 0)$

On the Δ-direction the symmetry is isomorphic with the C_{2v} point group. The bond charge wave described by Eq.(A-13) has the B_1 symmetry. In the xy-plane the transverse phonon has the B_1 symmetry and the eigenvalue becomes

$$\omega_{B_1}^2(\mathbf{k}) = \omega_{0,B_1}^2(\mathbf{k}) - A^2\{a(\mathbf{k}) - b(\mathbf{k})\} \qquad (\mathrm{A}-18)$$

where ω_0 denotes the "bare" frequency. As displayed in Fig.A-3, by sufficiently large coupling constant A, BCT becomes unstable and diatomic molecular solid with the space group symmetry $D_{2h}^{18} - Cmca$ is realized. One must notice that the realized molecular solid has the fixed rate of the lattice parameters, $b/c = 2$, and to be as Fig.4 the distortion must be occurred from FCO, in which the situation of the softening is not changed.

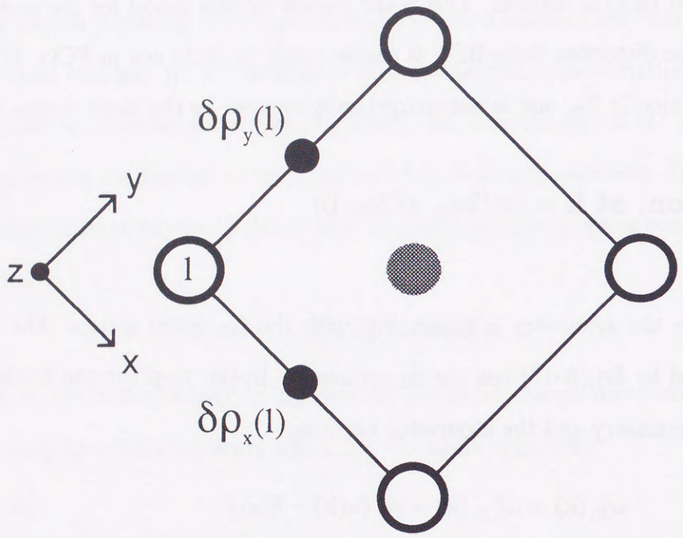

Figure A-1: Structure of BCT. Open circles represent the atoms on xy-plane and gray circle represents the body-centered atom. Small filled circles represent the bond charges denoted with the atom "l".

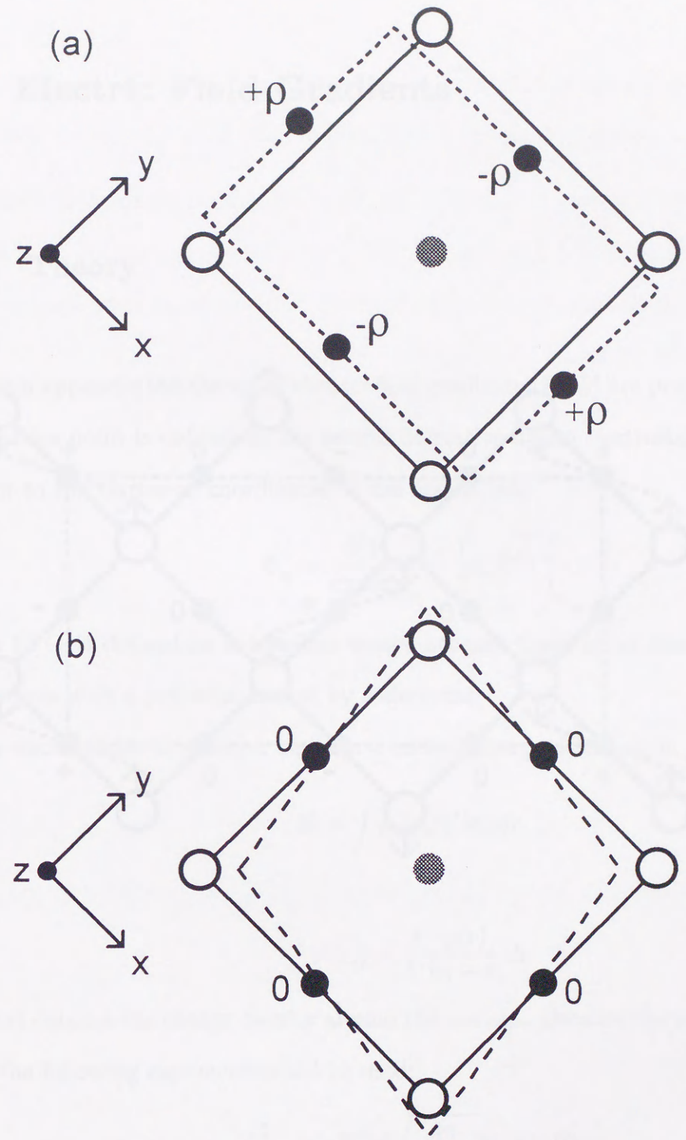

Figure A-2: Elastic distortion of BCT in B_{1g} (a) and B_{2g} (b) symmetries. Broken lines in (a) and (b) represent the distorted structure, i.e. BCO and FCO respectively. Small filled circles represent the bond charges and gray circle represents the body-centered atom of BCT.

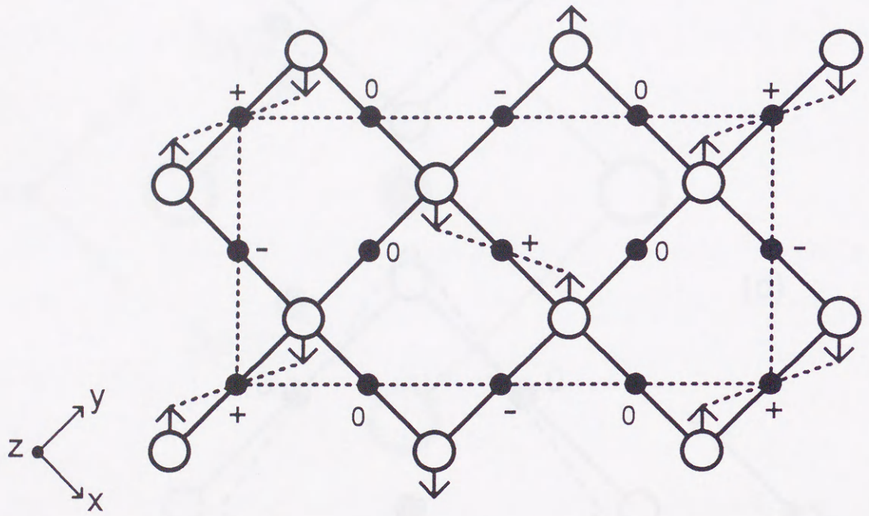

Figure A-3: The transverse phonon and the bond charge wave at $\mathbf{k} = (\pi/2a_0, \pi/2a_0, 0)$. Broken lines denote the realized diatomic molecular solid.

B Electric Field Gradients

B.1 Theory

In this appendix the theory of electric field gradients (EFG) are prepared [60]. The EFG at a lattice point is defined as the second derivative of the electrostatic potential V with respect to the Cartesian coordinates at the nuclear site

$$\Phi_{ij} = \frac{\partial^2 V}{\partial x_i \partial x_j}\bigg|_n - \frac{1}{3}\delta_{ij}\nabla^2 V\bigg|_n , \qquad (\mathrm{B}-1)$$

where EFG is defined as a traceless tensor because there is no interaction of a nuclear quadrupole with a potential caused by s electrons.

The electrostatic interaction between a nuclear charge distribution $\rho_n(\mathbf{r}_i)$ and V is

$$E_i = \int \rho_n(\mathbf{r}_i) V(\mathbf{r}_i) d\mathbf{r}_i , \qquad (\mathrm{B}-2)$$

where

$$V(\mathbf{r}_i) = \int \frac{\rho(\mathbf{r})}{|\mathbf{r}_i - \mathbf{r}|} d\mathbf{r} \qquad (\mathrm{B}-3)$$

and $\rho(\mathbf{r})$ denotes the charge density around the nucleus. Because the size of nucleus is very small the following expansion could be used:

$$\frac{1}{|\mathbf{r}_i - \mathbf{r}|} = \sum_{lm} r_i^l \sqrt{\frac{4\pi}{2l+1}} Y_{lm}(\hat{\mathbf{r}}_i) V^*_{lm;i} , \qquad (\mathrm{B}-4)$$

where

$$V_{lm;i} = \sqrt{\frac{4\pi}{2l+1}} \int \rho(\mathbf{r}) \frac{Y_{lm}(\hat{\mathbf{r}})}{r^{l+1}} d\mathbf{r}. \qquad (\mathrm{B}-5)$$

Finally Eq.(B-2) is written as

$$E_i = \sum_{lm} V^*_{lm;i} Q_{lm;i} \qquad (\mathrm{B}-6)$$

where

$$Q_{lm;i} = \sqrt{\frac{4\pi}{2l+1}} \int r_i^l Y_{lm}(\hat{\mathbf{r}}_i)\rho(\mathbf{r})d\mathbf{r} \qquad (\mathrm{B}-7)$$

is the nuclear multipole moment. In Eq.(B-7) the $l = 2$ components represent the nuclear quadrupole moments, and the $l = 2$ terms of Eq.(B-5) are the tensor components of EFG. In the full-potential calculations, the terms of Eq.(B-5) could be taken from the last two terms of the electrostatic potential Eq.(21) with $r \to 0$.

The relation between Eq.(B-1) and Eq.(B-5) is as follows [69]:

$$\Phi_{xx} = \sqrt{\frac{3}{2}}(V_{22} + V_{2-2}) - V_{20} \qquad \text{(B-8)}$$

$$\Phi_{yy} = -\sqrt{\frac{3}{2}}(V_{22} + V_{2-2}) - V_{20} \qquad \text{(B-9)}$$

$$\Phi_{zz} = 2V_{20} \qquad \text{(B-10)}$$

$$\Phi_{xy} = i\sqrt{\frac{3}{2}}(-V_{22} + V_{2-2}) \qquad \text{(B-11)}$$

$$\Phi_{yz} = i\sqrt{\frac{3}{2}}(V_{21} + V_{2-1}) \qquad \text{(B-12)}$$

$$\Phi_{zx} = \sqrt{\frac{3}{2}}(-V_{21} + V_{2-1}) \; . \qquad \text{(B-13)}$$

If Φ_{ij}'s are diagonalized, then an asymmetry parameter, which vary between 0 and 1, is defined as

$$\eta = \frac{\Phi_{xx} - \Phi_{yy}}{\Phi_{zz}} \qquad (\mathrm{B}-14)$$

under the condition $|\Phi_{zz}| \geq |\Phi_{yy}| \geq |\Phi_{xx}|$ and $\Phi_{xx} + \Phi_{yy} + \Phi_{zz} = 0$.

B.2 Simple estimation of EFG for p electron system

EFG of halogen is approximately estimated by the distortion of p electrons [70]. From Eq.(B-10) the principal component of EFG is

$$\Phi_{zz} = \int |\psi(\mathbf{r})|^2 \frac{3\cos^2\theta - 1}{r^3} d\mathbf{r}^3 \qquad (\mathrm{B}-15)$$

where $\psi(\mathbf{r})$ denotes the electronic wave function. If the Cartesian coordinates are set as the eigenvector of EFG, i.e. Φ is decomposed in three diagonal terms, and the wave function is defined as $\psi = \sum_i \sqrt{n_i}\phi(r)Y_{1i}(\hat{\mathbf{r}})$ then

$$\Phi_{zz} = C(n_z - \frac{n_x + n_y}{2}) \qquad (\mathrm{B}-16)$$

where

$$C = \frac{4}{5}\int \frac{\phi^2(r)}{r} dr \; . \qquad (\mathrm{B}-17)$$

Similarly

$$\Phi_{xx} = C(n_x - \frac{n_y + n_z}{2}) \qquad \text{(B-18)}$$

$$\Phi_{yy} = C(n_y - \frac{n_x + n_z}{2}) \; . \qquad \text{(B-19)}$$

Finally the asymmetry parameter η is

$$\eta = \frac{3(n_x - n_y)}{2n_z - n_x - n_y} \; . \qquad (\mathrm{B}-20)$$

References

[1] E. Wigner and H.B. Huntington, J. Chem. Phys. **3**, 764 (1935).

[2] H.K. Mao and R.J. Hemley, Rev. Mod. Phys. **66**, 671 (1994).

[3] N.W. Ashcroft, Phys. World, **8**, 43 (1995).

[4] Y. Fujii, K. Takemura, and O. Shimomura, Solid State Phys. (Japan), **24**, 399 (1989).

[5] F. van Bolhuis, P.B. Koster, and T. Migechelsen, Acta Crystallog. **23**, 90 (1967).

[6] B.M. Riggleman and H.G. Drickamer, J. Chem. Phys. **38**, 2721 (1963).

[7] H. G. Drickamer, R. W. Lynch, R. L. Clendenen, and E. A. Perez-Albuerne, Solid State Phys. **19**, 135 (1965), and references therein.

[8] K. Syassen, K. Takemura, H. Tups, and A. Otto, in *Physics of Solids under High Pressure*, edited by J.S. Schilling and R.N. Shelton (North-Holland, Amsterdam, 1981), p.125.

[9] N. Sakai, K. Takemura, and K. Tsuji, J. Phys. Soc. Jpn. **51**, 1811 (1982).

[10] K. Shimizu, N. Tamitani, N. Takeshita, M. Ishizuka, K. Amaya, and S. Endo, J. Phys. Soc. Jpn. **61**, 3853 (1992).

[11] O. Shimomura, K. Takemura, Y. Fujii, S. Minomura, M. Mori, Y. Noda, and Y. Yamada, Phys. Rev. B **18**, 715 (1978).

[12] K. Takemura, S. Minomura, O. Shimomura, and Y. Fujii, Phys. Rev. Lett. **45**, 1881 (1980).

[13] Y. Fujii, K. Hase, Y. Ohishi, N. Hamaya, and A. Onodera, Solid State Commun. **59**, 85 (1986).

[14] Y. Fujii, K.Hase, N. Hamaya, Y. Ohishi, and A. Onodera, Phys. Rev. Lett. **58**, 796 (1987).

[15] H. Fujihisa, Y. Fujii, K. Hase, Y. Ohishi, N. Hamaya, K. Tsuji, K. Takemura, O. Shimomura, H. Takahashi, and T. Nakajima, High Pressure Res. **4**, 330 (1990).

[16] R. Reichlin, A. K. McMahan, M. Ross, S. Martin, J. Hu, R. J. Hemley, H. Mao, and Y. Wu, *Phys. Rev. B* **49**, 3725 (1994).

[17] H. Fujihisa, Y. Fujii, K. Takemura, O. Shimomura, R.J. Nelmes, and M.I. McMahon, in *Proceedings of the 4th Workshop of the ICUr High Pressure Group on Synchrotron and Neutron Souces, Tsukuba, March 22-24, 1995*: to be published.

[18] H. Fujihisa, unpublished; the data was obtained with the experiments described in Ref. [17].

[19] F. D. Murnaghan, Proc. Natn. Acad. Sci. **30**, 244 (1944).

[20] M. Pasternak, J. N. Farrell, and R. D. Taylor, Phys. Rev. Lett. **58**, 575 (1987).

[21] M. Pasternak, J. N. Farrell, and R. D. Taylor, Phys. Rev. Lett. **59**, 945 (1987).

[22] M. Pasternak, J. N. Farrell, and R. D. Taylor, Solid State Commun. **61**, 409 (1987).

[23] O. Shimomura, K. Takemura, and K. Aoki, in *High Pressure in Research and Industry*, edited by C.M. Backman, T. Johanisson, and L. Tagner, (Uppsala, Arkitektkopia, 1982), p.272.

[24] Y. Hayashi, Y. Fujii, H. Fujihisa, K. Aoki, H. Yamawaki, O. Shimomura, and K. Takemura, in *Recent Trends in High Pressure Research*, edited by A.K. Singh (Oxford IBH, New Delhi, 1982), p.119.

[25] H. Olijnyk, W. Li, and A. Wokaun, Phys. Rev. B **50**, 712 (1994).

[26] Y. Natsume and T. Suzuki, Solid State Commun. **44**, 1105 (1982); Y. Natsume, in *Solid State Physics under High Pressure*, edited by S. Minomura (Reidel, Drodrecht, Holland, 1985), p. 43.

[27] F. Siringo, R. Pucci, and N.H. March, Phys. Rev. B **37**, 2491 (1988); F. Siringo, R. Pucci, and N.H. March, Phys. Rev. B **38**, 9567 (1988).

[28] N. Orita, Ph.D. thesis, Tohoku University, Japan, 1990.

[29] N. Orita, K. Niizeki, K. Shindo, and H. Tanaka, J. Phys. Soc. Jpn. **61**, 4502 (1992).

[30] H. Sakamoto, M. Shirai, N. Suzuki, J. Phys. Soc. Jpn. **64**, 3860 (1995).

[31] H. Sakamoto, T. Oda, M. Shirai, and N. Suzuki, J. Phys. Soc. Jpn. **65**, 489 (1996).

[32] N. Orita, T.Sasaki, and K. Niizeki, Solid State Commun. **64**, 391 (1987).

[33] N. Orita, K. Niizeki, and K. Shindo, in *20th International Conference on the Physics of Semiconductors Vol.3*, edited by E. M. Anatassakis and J. D. Joannopoulos (World Scientific, Singapore, 1990), p. 2201.

[34] S.C. Nyburg, J. Chem. Phys. **40**, 2493 (1964).

[35] K. Kobashi and R.D. Etters, J. Chem. Phys. **79**, 3018 (1983).

[36] K. Takemura, S. Minomura, O. Shimomura, Y. Fujii, and J.D. Axe, Phys. Rev. B **26**, 998 (1982).

[37] T. Luty and J.C. Raich, Can. J. Chem. **66**, 812 (1988).

[38] K. Shimizu, K. Amaya, and S. Endo, in *High Pressure Science and Technology, Proceedings of the Joint XV AIRAPT and XXXIII EHPRG International Conference*, edited by W.A. Trzeciakowski (World Scientific, Singapore, 1996).

[39] Y. Fujii, K. Hase, Y. Ohishi, H. Fujihisa, N. Hamaya, K. Takemura, O. Shimomura, T. Kikegawa, Y. Amemiya, and T. Matsushita, Phys. Rev. Lett. **63**, 536 (1989).

[40] K. Takemura, O. Shimomura, and Y. Fujii, Phys. Rev. Lett. **59**, 944 (1987).

[41] K.H. Weyrich, Phys. Rev. B **37**, 10269 (1988).

[42] M. Methfessel, C.O. Rodriguez, and O.K. Andersen, Phys. Rev. B **40**, 2009 (1988).

[43] S.Yu. Savrasov and D.Yu. Savrasov, Phys. Rev. B **46**, 12181 (1992).

[44] P. Hohenberg and W. Kohn, *Phys. Rev.* **136**, B864 (1964); W. Kohn and L. J. Sham, *ibid.* **140**, A1133(1965).

[45] M.T. Yin and M.L. Cohen, Phys. Rev. B **26**, 3259 (1982).

[46] O.K. Andersen, Phys. Rev. B **12**, 3060 (1975).

[47] For example, J.D. Talman, in *Special Functions, A Group Theoretic Approach* (Benjamin, New York, 1968), Chapter 12.

[48] E.U. Condon and G.H. Shortley, in *The Theory of Atomic Spectra* (Cambridge U. P., Cambridge, 1951).

[49] S.Yu. Savrasov, unpublished.

[50] U. von Barth and L. Hedin, *J. Phys. C* **5**, 1629 (1972).

[51] D.E. Koelling and B.N. Harmon, J. Phys. C: Solid State Phys. **10**, 3107 (1977).

[52] D. Liberman, J.T. Waber, and D.T. Cromer, Phys. Rev. **137**, A27 (1965).

[53] P.E. Blöchl, O. Jepsen, and O.K. Andersen, Phys. Rev. B **49**, 16223 (1994).

[54] R. O. Jones and O. Gunnarsson, Rev. Mod. Phys. **61**, 689 (1989).

[55] C.J. Bradley and A.P. Cracknell, in *The Mathematical Theory of Symmetry in Solids* (Clarendon Press, Oxford, 1972).

[56] H. Yamamoto, K. Seki, T. Mori, and H. Inokuchi, J. Chem. Phys. **86**, 1775 (1987).

[57] M. Pasternak, A. Simopoulos, and Y. Hazony, Phys. Rev. **140**, A1892 (1965).

[58] P. Blaha and K. Schwartz, Theochem **93**, 355 (1992).

[59] N.N. Greenwood and T.C. Gibb, in *Mössbauer Spectroscopy*, (Chapman and Hall, London, 1971), p. 607.

[60] P. Herzig, Theoret. Chim. Acta **67**, 323 (1985).

[61] S.L. Ruby and G.K. Shenoy, in *Mössbauer Isomer Shifts*, edited by G.K. Shenoy and F.E. Wagner (North-Holland, Amsterdam, 1978), p. 617.

[62] G. Nilson and G. Nelin, Pys. Rev. B **6**, 3777 (1972).

[63] H.J. McSkimin and P. Andreatch, Jr., J. Appl. Phys. **35**, 3312 (1965).

[64] R. Yu, D. Singh, and H. Krakauer, Phys. Rev. B **43**, 6411 (1991).

[65] H. Fujihisa, Y. Fujii, K. Takemura, and O. Shimomura, J. Phys. Chem. Solids, **56**, 1439 (1995).

[66] G.M. Kalvius and G.K. Shenoy, Atomic Data and Nuclear Data Tables **14**, 639 (1974).

[67] K. Yamaguchi and H. Miyagi, Solid State Commun. **99**, 89 (1996).

[68] See e.g. L.D. Landau and E.M. Lifshitz, in *Statistical Physics, Part 1, Third edition*, (Pergamon, Oxford, 1980), p.264.

[69] E. Matthias, W. Schneider, and R.M. Steffen, Ark. Fys. **24**, 97 (1963).

[70] T.P. Das and E.L. Hahn, Solid State Phys. Suppl. **1**, 1 (1958).